UNIVERSITY OF OKLAHOMA

GRADUATE COLLEGE

Charming Flavor Changing Interactions of Beyond Standard Model Higgs Boson at Large Hadron Collider

A DISSERTATION

SUBMITTED TO THE GRADUATE FACULTY

in partial fulfillment of the requirements for the

Degree of

DOCTOR OF PHILOSOPHY

By CHENYU FANG

Norman, Oklahoma

2025

Downloaded from SHAREOK. Persistent Handle URL: https://hdl.handle.net/11244/341743

Charming Flavor Changing Interactions of Beyond Standard Model Higgs Boson at Large Hadron Collider

A DISSERTATION APPROVED FOR THE
HOMER L. DODGE DEPARTMENT OF PHYSICS AND ASTRONOMY

BY THE COMMITTEE CONSISTING OF

Dr. Chung Kao, Chair

Dr. Nikola Petrov

Dr. Brad Abbott

Dr. Howard Baer

Dr. Kieran Mullen

©Copyright by Chenyu Fang 2025

All Rights Reserved.

Acknowledgement

I extend my deepest gratitude to my advisor, Professor Chung Kao, for his unwavering support, patient guidance, and insightful critiques throughout my research journey. His dedication to academic excellence and meticulous attention to detail have profoundly shaped both my research and this dissertation. I am also deeply grateful for his kind assistance and thoughtful guidance that greatly enriched my academic and personal life during my stay in Norman.

I am equally thankful to the members of my thesis committee—Professor Nikola Petrov, Professor Brad Abbott, Professor Howard Baer, and Professor Kieran Mullen—for their constructive feedback and invaluable suggestions that have greatly enhanced the quality of my work.

I would also like to express my sincere appreciation to my collaborators. To Professor Phillip Gutierrez, with whom I worked on two projects, I am deeply grateful for his generous guidance and countless helpful discussions. To Professor George Wei-Shu Hou, I extend my thanks for his valuable comments and advice on one of my projects. I am also indebted to Dr. Mohamed Krab, whose discussions have broadened my research perspective and improved my scientific writing. To Nicolas Bost, I am grateful for his assistance in several important parts of the data analysis.

My appreciation also goes to the faculty and staff of the Department of Physics and Astronomy at the University of Oklahoma, whose support and resources have been indispensable throughout my graduate studies.

I would like to thank my friends—Zongkai Peng, Zhitao Zhao, Zongyuan Liu, Mulin Fang, Yanting Guo, Diya Tang, and Lvshuang Huang—for their friendship and encouragement. As an international student, the first few years in a new country

were challenging, but their companionship helped me overcome homesickness and create many joyful memories. A special note of thanks goes to Zongkai Peng, my friend and roommate for more than six years, whose constant support helped me through countless difficulties.

Finally, my heartfelt gratitude goes to my parents in China for their endless love, encouragement, and faith in me. This long journey would not have been possible without their support. Words cannot fully express my appreciation—thank you for everything. I look forward to reuniting with you in the future.

Table of Contents

List of Abbreviations **xiv**

1 Introduction **1**

1.1 Structure of Standard Model 1

1.1.1 Particle Content 1

1.1.2 Theoretical Framework 7

1.2 Needs for New Physics 21

1.2.1 Baryon Asymmetry of the Universe 21

1.2.2 Flavor Anomalies 22

1.3 General Two Higgs Doublet Model 23

1.3.1 Modified Higgs Potential 24

1.3.2 The Yukawa Sector 27

1.4 Summary of Chapter 1 29

2 Higgs Signal Channels and Analysis Strategies **31**

2.1 Motivations 32

2.1.1 Charged Higgs Flavor-changing channel 32

2.1.2 FCNH signal channels 33

2.2 Analysis Tools and Strategies 36

2.2.1 Analytical Tools 36

2.2.2 Analysis Strategies 43

2.3 Summary of Chapter 2 47

3 Searching for Charged Higgs Boson at the LHC **49**

3.1 Constraints on Relevant Parameters 49

3.2 Collider Study for $H^+ \to c\bar{b}$ 51
3.2.1 Higgs signal 51
3.2.2 The Physics Background 52
3.2.3 Mass Reconstruction and Realistic acceptance 52
3.3 Discovery Potential 54
3.4 Summary of Chapter 3 55

4 Probing Heavy Neutral Higgs Bosons via Interactions with Top quark 58

4.1 Detecting Flavor Changing Neutral Higgs Bosons in Top Decays with τ pairs 59
4.1.1 The Higgs Signal and Standard Model background 59
4.1.2 Mass Reconstruction and Realistic Acceptance Cuts 63
4.1.3 Discovery Potential 68
4.2 Top Pairs with Flavor Changing Neutral Higgs Decays 74
4.2.1 The Higgs Signal and Standard Model background 74
4.2.2 Mass Reconstruction and Realistic Acceptance Cuts 75
4.2.3 Discovery Potential at the LHC 80
4.3 Summary of Chapter 4 84

5 Conclusion 86

REFERENCES 89

Appendix A 96

List of Figures

1.1 Standard Model of Elementary Particles. Source: CERN (2025) . 2

1.2 Higgs potential with fixed λ and μ^2 for (a) $\Im\ \phi = 0$ and (b) general ϕ. 16

2.1 Branching ratios of $H^+ \to XY$ as a function of m_{H^+} for (a) $\rho_{tc} = 0.1$, and (b) $\rho_{tc} = 0.4$. 33

2.2 Branching ratios of $\phi^0 \to XY$ as functions of m_ϕ. The parameters are chosen as $c_{\beta-\alpha} = 0.01$ and $\rho_{tt} = 0.2 \times m_\phi/(150\text{ GeV})$, with: (a) H^0, $\tilde{\rho}_{tc} = 0.1$; (b) H^0, $\tilde{\rho}_{tc} = 0.4$; (c) A^0, $\tilde{\rho}_{tc} = 0.1$; (d) A^0, $\tilde{\rho}_{tc} = 0.4$. 37

3.1 Leading-order Feynman diagrams for $cg \to bH^+$. 52

3.2 Invariant mass distributions $d\sigma/dM_{cb_1}$ for the signal and dominant backgrounds $b\bar{b}j$ (magenta, dashed) and $c\bar{c}j$ (black, dotted) at $\sqrt{s} = 14$ TeV, shown for $\rho_{tc} = 0.4$, (a) $m_{H^+} = 200$ GeV (blue, solid) and (b) $m_{H^+} = 400$ GeV (blue, solid). 54

3.3 The cross section as a function of ρ_{tc} for signal and background at $\sqrt{s} = 14$ TeV after selection cuts, shown for (a) $m_{H^+} = 200$ GeV and (b) $m_{H^+} = 400$ GeV. 56

3.4 The 5σ discovery contours at the LHC in the (m_{H^+}, ρ_{tc}) plane for (a) $\sqrt{s} = 13$ TeV and (b) $\sqrt{s} = 14$ TeV with $L = 300\,\text{fb}^{-1}$ (dark green solid) and $L = 3000\,\text{fb}^{-1}$ (light green dashed). In addition, 3σ discovery contour with $L = 3000\,\text{fb}^{-1}$ (red dotted) are shown for both 13 and 14 TeV. 57

4.1 Leading-order Feynman diagrams for the $\phi^0 \to \tau^+\tau^-$ signal. . . . 60

4.2 Invariant mass distribution $d\sigma/dM_{jj}$ for the Higgs signal (magenta, solid) and for the dominant background from ttj (blue, dashed) and $ttjj$ (red, dot) at the LHC with $\sqrt{s} = 13$ TeV. Results are shown for (a) parton level, and (b) event level. 64

4.3 Invariant mass distribution $d\sigma/dM_{bjj}$ for the Higgs signal (magenta, solid) and for the dominant background from ttj (blue, dashed) and $ttjj$ (red, dot) at the LHC with $\sqrt{s} = 13$ TeV. Results are shown for (a) parton level, and (b) event level. 65

4.4 Invariant mass distributions $d\sigma/dM_{\tau\tau}$ for the Higgs signal with $m_H = 130$ GeV (magenta, solid), 150 GeV (green, dot-dashed), 200 GeV (black, solid) and for the dominant background from ttj (blue, dashed) and $ttjj$ (red, dot) at $\sqrt{s} = 13$ TeV. Results are shown for (a) parton level, and (b) event level with detector simulation in pp collisions. 66

4.5 Invariant mass distributions $d\sigma/dM_{c\tau\tau}$ for the Higgs signal ($t \to c\phi^0$) with $m_H = 130$ GeV (magenta, solid) and 150 GeV (Green, dot-dashed) and for the dominant background from ttj (blue, dashed) and $ttjj$ (red, dot) at $\sqrt{s} = 13$ TeV. Results are shown for (a) parton level, and (b) event level with detector simulation in pp collisions. 66

4.6 Energy distribution for the charm quark ($d\sigma/dE_c$) in the top rest frame for the Higgs signal from $t \to cH^0$ with $m_H = 130$ GeV (magenta, solid), 150 GeV (Green, dot-dashed) and for the dominant background from ttj (blue, dashed) and $ttjj$ (red, dot) at $\sqrt{s} = 13$ TeV. Results are shown for (a) parton level, and (b) event level with detector simulation in pp collisions. 67

4.7 Signal cross section σ vs. mass of Higgs boson for the FCNH signal ($t \to c\Phi^0$) with $\rho_{tc} = 0.1$ (blue) and 0.5 (red) at $\sqrt{s} = 13.6$ TeV, where ϕ^0 is (a) Heavy Scalar H^0, and (b) pseudoscalar A^0 with detector simulation in pp collisions. 72

4.8 Signal cross section σ vs. ρ_{tc} of Higgs boson for the FCNH signal ($t \to c\Phi^0$) with $m_\phi = 130$ GeV (blue), 150 GeV (red) and 200 GeV (magenta) at $\sqrt{s} = 13.6$ TeV, where Φ^0 is (a) Heavy Scalar H^0, and (b) pseudoscalar A^0 with detector simulation in pp collisions. . . . 72

4.9 Parton Level and Event Level 5σ discovery contours at the LHC at $\sqrt{s} = 13.6$ TeV in the $[m_\Phi, \tilde{\rho}_{tc}]$ plane for (a) Parton Level Heavy Scalar H^0, (b) Parton Level pseudoscalar A^0, (c) Event Level Heavy Scalar H^0 and (d) Event Level pseudoscalar A^0 with $L = 30fb^{-1}$ (dark green dotted dashed), $300fb^{-1}$ (medium green solid) and $L = 3000fb^{-1}$ (light green dashed) 73

4.10 Parton Level and Event Level 5σ discovery contours of Higgs mass degenerate case at the LHC at $\sqrt{s} = 13.6$ TeV in the $[m_\Phi, \tilde{\rho}_{tc}]$ plane for Parton Level (left) and Event Level (right) with $L = 30fb^{-1}$ (dark green dotted dashed), $300fb^{-1}$ (medium green solid) and $L = 3000fb^{-1}$ (light green dashed) 73

4.11 Leading-order Feynman diagrams for $pp \to t\phi \to t(tc)$. 74

4.12 Invariant mass distribution $d\sigma/dM_{l\nu}$ (left) and $d\sigma/dM_{b_1 l\nu}$ (right) for the Higgs signal. 77

4.13 Invariant mass distributions $d\sigma/dM_{cb_1 l\nu}$ for the Higgs signal signal and dominant backgrounds $t\bar{t}j$ (red, dashed) at $\sqrt{s} = 13.6$ TeV, shown for $\tilde{\rho}_{tc} = 0.4$, (a) $m_H = 200$ GeV (blue, solid) and (b) $m_H = 400$ GeV (blue, solid). 78

4.14 Energy distribution for the charm quark ($d\sigma/dE_c$) in the Higgs rest frame for the Higgs signal from $H^0 \to t\bar{c}$ with (a) $m_H = 200$ GeV (blue, solid), (b) $m_H = 400$ GeV (blue, solid) with $\tilde{\rho}_{tc} = 0.4$, at $\sqrt{s} = 13.6$ TeV. Dominant background are also presented (red, dotted) in both cases. 79

4.15 The cross sections as functions of m_H for (a) the all-top signal and its dominant background $t\bar{t}j$ (red, dashed), and (b) the same-sign top signal and its dominant background $t\bar{t}W$ (red, dashed). Both signal channels are shown for two benchmark values of $\tilde{\rho}_{tc}$: $\tilde{\rho}_{tc} = 0.1$ (blue, solid) and $\tilde{\rho}_{tc} = 0.4$ (green, solid). 82

4.16 The 5σ discovery contours at the LHC in the $(m_H, \tilde{\rho}_{tc})$ plane are shown for: (a) All-top final state at $\sqrt{s} = 13$ TeV, (b) Same-sign top final state at $\sqrt{s} = 13$ TeV, (c) All-top final state at $\sqrt{s} = 13.6$ TeV, (d) Same-sign top final state at $\sqrt{s} = 13.6$ TeV, (e) degenerate $m_H = m_A$ all-top final state at $\sqrt{s} = 13.6$ TeV, and (f) degenerate $m_H = m_A$ same-sign top final state at $\sqrt{s} = 13.6$ TeV. The contours correspond to integrated luminosities of $L = 100$ fb^{-1} (dark-green dashed), 300 fb^{-1} (medium-green solid), and 3000 fb^{-1} (light-green dotted). In addition, the 3σ discovery contours for $L = 3000$ fb^{-1} (red dotted) are shown for both 13 TeV and 14 TeV scenarios. . . 83

1 p_T^c distribution for $m_H = 200$ (blue), 300 (magenta) and 400 (cyan) with dominant background ttW (red) at $\sqrt{s} = 13$ TeV. 96

List of Tables

1.1 Fermion masses from PDG 2024 [1]. 3

1.2 Weak quantum numbers of Standard Model fermions. 12

1.3 Assignment of Z_2 charges for the right-handed fermions, and the resulting relations among Yukawa coupling matrices in the Z_2-symmetric types of 2HDM Yukawa sectors. The Higgs doublets have Z_2 quantum numbers $-$ (Φ_1) and $+$ (Φ_2). 29

3.1 Final selection criteria for signal and backgrounds events. 54

3.2 Benchmark points used in this table, which correspond to $\rho_{ct} = 0.05$, $\rho_{tc} = 0.4$ and $m_{H^+} = 200$ GeV (BP_1), $m_{H^+} = 300$ GeV (BP_2), and $m_{H^+} = 400$ GeV (BP_3). Statistical significance is presented with integrated luminosity $L = 500\,\mathrm{fb}^{-1}$. K-factors are included in the cross section. 55

4.1 Branching fractions for different τ-lepton decays modes. 62

4.2 Selection criteria for signal and backgrounds events with $m_\phi \leq 150$ GeV and $m_\phi > 150$ GeV. In this table, S_1 represents signal events with $m_\phi \leq 150$ GeV , S_2 represents signal events with $m_\phi > 150$ GeV, BG_1 represents backgrounds events with $m_\phi \leq 150$ GeV and BG_2 represents signal events with $m_\phi > 150$ GeV. 68

4.3 Parton level signal cross section in fb after all cuts with $\varepsilon_b = 0.7$ and $\varepsilon_\tau = 0.723$. 69

4.4 Background cross sections in fb after applying the mass selection at the parton level. 69

4.5 Event level signal cross section in fb after all cuts. 70

4.6 Background cross sections in fb after applying the mass selection at the event level. 71

4.7 Final selection criteria applied to the signal and background events in the all-top channel. 79

4.8 Final selection criteria applied to the signal and background events in the SS-top channel. 80

4.9 All-top signal and background cross sections. The benchmark points correspond to $\tilde{\rho}_{tc} = 0.4$ with $(m_H, m_A) = (200, 200)\,\text{GeV}$ (BP_1) and $(400, 400)\,\text{GeV}$ (BP_2). The signal cross sections are denoted by σ_H and σ_A for the H^0 and A^0 channels, respectively. The statistical significance is evaluated for an integrated luminosity of $L = 500\ \text{fb}^{-1}$, with $N_{SS}(H^0)$ representing the H^0 channel and N_{SS} for the degenerate case. 81

4.10 Same-sign top signal and background cross sections. The benchmark points correspond to $\tilde{\rho}_{tc} = 0.4$ with $(m_H, m_A) = (200, 200)\,\text{GeV}$ (BP_1) and $(400, 400)\,\text{GeV}$ (BP_2). The signal cross sections are denoted by σ_H and σ_A for the H^0 and A^0 channels, respectively. The statistical significance is evaluated for an integrated luminosity of $L = 500\ \text{fb}^{-1}$, with $N_{SS}(H^0)$ representing the H^0 channel and N_{SS} for the mass degenerate case. 81

1 Optimized E_c^* selection ranges for the all-top channel corresponding to different Higgs boson masses m_ϕ. 96

List of Abbreviations

LHC	Large Hadron Collider
SM	Standard Model
BSM	Beyond the Standard Model
FCNH	Flavor-Changing Neutral Higgs
CERN	European Organization for Nuclear Research
PDF	Parton Distribution Function
MC	Monte Carlo
VEGAS	Adaptive Monte Carlo integration algorithm (not an acronym)
MG5	MadGraph5_aMC@NLO
PYTHIA8	Program for High-Energy Physics Event Generation (version 8)
DELPHES	Fast detector simulation framework (not an acronym)
PDG	Particle Data Group
QCD	quantum chromodynamics
VEV	vacuum expectation value
CKM	Cabibbo–Kobayashi–Maskawa
CP	charge–parity
G2HDM	general Two-Higgs-Doublet Model
2HDM	Two-Higgs-Doublet Model
FCNCs	flavor-changing neutral currents
EWSB	electroweak symmetry breaking
2HDMC	Two-Higgs-Doublet Model Calculator
LO	leading-order
NLO	next-to-leading-order
NNLO	next-to-next-to-leading-order
UFO	Universal FeynRules Output
HELAS	HELicity Amplitude Subroutines
LHE	Les Houches Even
MLM	Mangano–Lönnblad–Moretti
CKKW-L	Catani–Krauss–Kuhn–Webber–Lönnblad
ME	Matrix Element
PS	Parton Showering
BDTs	boosted decision trees
ROC	receiver operating characteristi
AUC	area under the ROC curve
CL	confidence leve
CT14LLO	CT14 LO from the CTEQ-TEA Global Analysis
BPs	benchmark points
SS-top	same-sign top
2HDM-UFO	Two-Higgs-Doublet Model Universal FeynRules Output

Abstract

In this dissertation, we discuss the flavor changing interactions of Beyond Standard Model (BSM) Higgs bosons, including neutral heavy Higgs (CP-even scalar H^0 and CP-odd pseduo-scalar A^0) and Charged Higgs ($H^{\pm}$), with quarks at the CERN Large Hadron Collider (LHC). Adopting a general two Higgs doublet model (G2HDM), we investigate several different channels to study the flavor changing interactions of BSM Higgs bosons. For flavor changing neutral Higgs bosons, we look for $t \to c\phi^0$ or $\phi^0 \to t\bar{c}$ followed with $\phi^0 \to \tau^+\tau^-$ or $\phi^0 \to t\bar{c}/\bar{t}c$. For interactions of charged Higgs, we study $cg/\bar{c}g \to bH^{\pm}$ with $H^- \to b\bar{c}$ or $H^+ \to \bar{b}c$. This report presents the study of the discovery potential of these channels at the LHC. Applying Monte Carlo simulations with VEGAS, MadGraph 5, Pythia 8 and Delphes, we evaluate the signal and dominant physical background cross sections after implementing realistic selection rules. We limit the parameter space for experimental results at the LHC and discuss the discovery rate at Collider energy $\sqrt{s} = 13$ TeV, 13.6 TeV and 14 TeV.

Chapter 1

Introduction

1.1 Structure of Standard Model

The Standard Model (SM) is one of the most successful particle physics models providing a description of nearly all observed phenomena in particle physics. It is a gauge-symmetric quantum field theory that classifies the particles according to their quantum properties and their interactions with other particles. As such, the SM encapsulates our current understanding of the fundamental particles that constitute the visible universe. First proposed by Abraham Pais and Sam Treiman in 1975 [2], the SM represents the culmination of decades of work by numerous prominent particle physicists from around the world. The model unifies three of the four known fundamental interactions, electro-magnetic, weak, and strong, into a coherent theoretical structure, forming the foundation of modern particle physics.

1.1.1 Particle Content

In the Standard Model, all known fundamental particles are classified into two broad categories: fermions and bosons. Fermions constitute the building blocks of matter, while bosons mediate the fundamental forces among them. In addition, the Higgs boson provides mass to the other particles via the Higgs mechanism. Fig. **1.1** provides an overview of the particle content of the Standard Model (CERN, 2025).

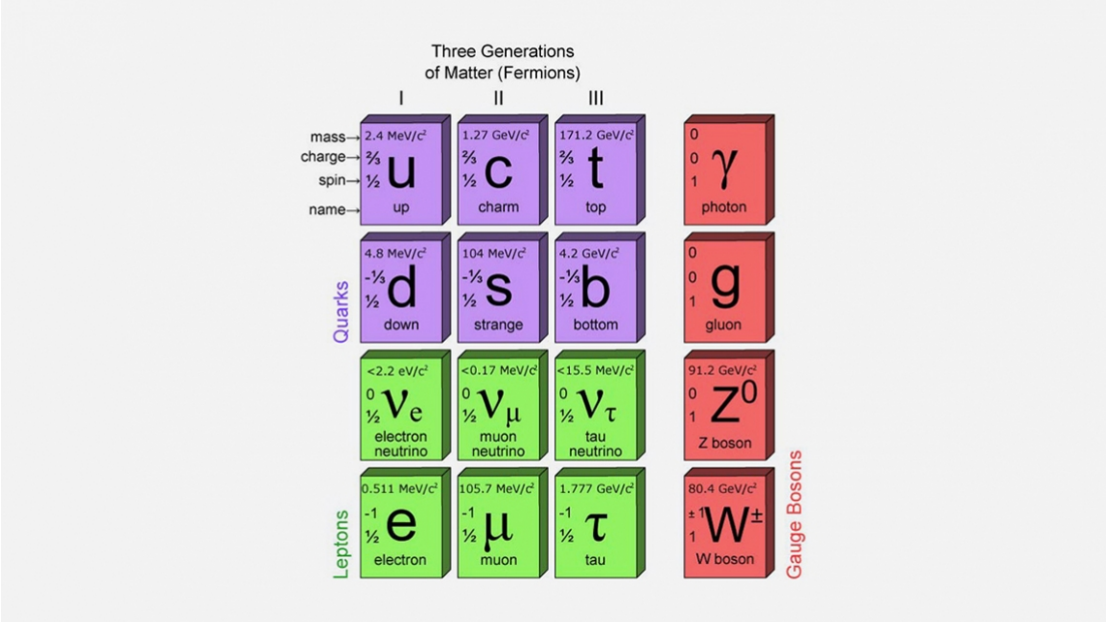


Figure 1.1: Standard Model of Elementary Particles. Source: CERN (2025)

Fermions: Leptons and Quarks

Fermions are particles with half-integer spin, $(2n+1)/2$ for $n = 0, 1, 2, \ldots$, and obey Fermi–Dirac statistics [3]. A distinctive property of fermions is their adherence to the Pauli exclusion principle, which forbids two identical fermions from occupying the same quantum state simultaneously.

Fermions come in two families: leptons and quarks, each organized into three generations. Leptons include the charged leptons and their corresponding neutrinos $\{\text{electron}\,(e),\ \text{electron-neutrino}\,(\nu_e)\}$, $\{\text{muon}\,(\mu),\ \text{muon-neutrino}\,(\nu_\mu)\}$, $\{\text{tau-lepton}\,(\tau)\,,\ \text{tau-neutrino}\,(\nu_\tau)\}$.

Quarks are similarly grouped into pairs:

$$\{\text{up}\,(u),\ \text{down}\,(d)\},\quad \{\text{charm}\,(c),\ \text{strange}\,(s)\},\quad \{\text{top}\,(t),\ \text{bottom}\,(b)\},$$

representing the first, second, and third generations, respectively. Particles in

higher generations are heavier than those in the lower ones, as summarized in Table **1.1**, based on PDG 2024 data [1].

Leptons	Mass (GeV/c^2)	Quarks	Mass (GeV/c^2)
ν_e	$< 8 \times 10^{-10}$	u	$0.0022 \pm 7 \times 10^{-5}$
e	$5.11 \times 10^{-4} \pm 1.5 \times 10^{-13}$	d	$0.0047 \pm 7 \times 10^{-5}$
ν_μ	$< 1.9 \times 10^{-4}$	c	1.273 ± 0.0046
μ	$0.10566 \pm 2.3 \times 10^{-9}$	s	0.0935 ± 0.0008
ν_τ	$< 1.82 \times 10^{-2}$	t	$172.56 \pm 0.51 \pm 0.31$
τ	$1.7769 \pm 9 \times 10^{-5}$	b	4.78 ± 0.06

Table 1.1: Fermion masses from PDG 2024 [1].

Leptons. Leptons differ from quarks in several ways:

- They exist freely in nature and are not subject to confinement;
- They carry integer multiples of the electric charge e;
- They interact through electromagnetic and weak forces, but not via the strong force;
- They are relatively light (except the τ lepton that $m_\tau > m_c$).

Historically, the electron was discovered in 1897 by J. J. Thomson [4], followed by the muon in 1936, observed by Carl D. Anderson and Seth Neddermeyer [5]. The τ lepton was first predicted by Yung-Su Tsai in 1971 [6] and subsequently discovered between 1975 and 1977 by Martin Perl and collaborators [7, 8].

Neutrinos were first postulated by Wolfgang Pauli in 1930, in a famous letter proposing a neutral, light particle to account for the missing energy in β decay. Enrico Fermi later incorporated this particle into his theory of weak interactions,

coining the name "neutrino" [9]. Subsequent experiments confirmed the existence of three distinct neutrino flavors, each associated with one of the three charged leptons [10, 11].

Antiparticles. Dirac's relativistic wave equation for the electron [12] predicts both positive and negative energy solutions. The existence of these negative energy states led to the prediction of antiparticles—objects identical in mass but opposite in charge to their corresponding particles. The first antiparticle, the positron (e^+), was experimentally discovered in 1931 by Carl D. Anderson [13].

In modern notation, antiparticles are denoted by an overbar, for example $\bar{p}$ for the antiproton and $\bar{\nu}$ for the antineutrino. Charged leptons are conventionally labeled with a superscript "+," such as e^+ or μ^+. Charge conjugation, represented by the operator C, transforms a particle state into its corresponding antiparticle:

$$C, |p\rangle = |\bar{p}\rangle, . \tag{1.1}$$

Matter–antimatter symmetry arises naturally within this formalism, though the observed dominance of matter in the Universe indicates the presence of charge-parity-violating (CP-violating) processes beyond the Standard Model (BSM).

Quarks, Mesons, and Baryons. Quarks are fermionic constituents of hadrons and are never observed in isolation due to the phenomenon of color confinement. They carry fractional electric charges of $\pm\frac{1}{3}e$ and $\pm\frac{2}{3}e$. The quark model, proposed independently by Murray Gell-Mann and George Zweig in 1964 [14, 15], successfully explained the observed classification patterns of hadrons within the framework of $SU(3)$ flavor symmetry.

A meson is a bound state of a quark and an antiquark ($q\bar{q}$), whereas a baryon

consists of three quarks (qqq). Representative examples include:

- **Mesons:** π^+ ($u\bar{d}$), π^- ($d\bar{u}$), K^+ ($u\bar{s}$), K^0 ($d\bar{s}$), and η ($(u\bar{u} + d\bar{d} - 2s\bar{s})/\sqrt{6}$);
- **Baryons:** proton (uud), neutron (udd), Δ^+ (uud), Δ^0 (udd), and Ω^- (sss).

The introduction of the color quantum number resolved the apparent violation of the Pauli exclusion principle in baryons such as the Δ^{++} (uuu). Quarks exist in three color states—red, green, and blue—while only color-neutral (singlet) combinations correspond to observable particles.

In the late 1960s, deep-inelastic scattering experiments at SLAC [16, 17] revealed that the proton possesses an internal substructure consisting of three point-like constituents, providing the first direct experimental evidence for the quark model. Subsequent discoveries of the charm, bottom, and top quarks between 1974 and 1995 [18–21] established the three-generation structure of quarks, mirroring that of the leptons. The concept of isospin was introduced earlier to distinguish the nearly degenerate nucleons, with the proton and neutron forming an isospin doublet of total isospin $I = \frac{1}{2}$.

Gauge Bosons

Gauge bosons are spin-1 particles belonging to the class of bosons, which possess integer spins and obey Bose–Einstein statistics [22], originally developed by Satyendra Nath Bose and Albert Einstein. Unlike fermions, bosons are not subject to the Pauli exclusion principle. In the Standard Model, gauge bosons mediate the fundamental forces:

- Photon (γ) — mediator of the electromagnetic interaction;
- $W^{\pm}$ and Z bosons — mediators of the weak interaction;

- Gluons (g) — eight massless gauge bosons mediating the strong interaction.

The concept of the photon originated from Planck's quantization of light [23] and was further developed by Einstein to explain the photoelectric effect [24]. The weak gauge bosons $W^{\pm}$ and Z were predicted within the electroweak theory formulated by Glashow, Weinberg, and Salam [25]. They were subsequently discovered at CERN in 1983: the $W^{\pm}$ boson by the UA1 and UA2 collaborations [26], followed about five months later by the discovery of the Z boson [27]. Their measured masses,

$$M_W = 81 \pm 5 \text{ GeV/c}^2\,, \quad M_Z = 95.2 \pm 2.5 \text{ GeV/c}^2\,,$$

were in excellent agreement with the theoretical predictions,

$$M_W = 82 \pm 2 \text{ GeV/c}^2, \quad M_Z = 92 \pm 2 \text{ GeV/c}^2\,,$$

marking a major experimental validation of the Standard Model.

Higgs Boson

The Higgs boson (h) is a scalar (spin-0) particle associated with spontaneous symmetry breaking in the electroweak sector. It provides mass to the $W^{\pm}$ and Z boson, as well as the fermions, through Yukawa couplings. Discovered in 2012 at the LHC [28, 29] with a measured mass of approximately 125 GeV, the Higgs boson completes the Standard Model particle spectrum. Its properties continue to be studied with increasing precision as a potential window to new physics beyond the Standard Model.

1.1.2 Theoretical Framework

The formulation of the SM is based on two fundamental principles: *local gauge invariance* and *spontaneous symmetry breaking*. It is a gauge quantum field theory constructed upon the symmetry group

$$\mathcal{G}_{\mathrm{SM}} = SU(3)_C \otimes SU(2)_L \otimes U(1)_Y \tag{1.2}$$

which governs all known non-gravitational interactions: the electromagnetic, weak, and strong interaction. The electromagnetic and weak interactions are unified within the electroweak theory [30–32], while the strong interaction is described by the theory of quantum chromodynamics (QCD) [33, 34].

Gauge invariance dictates the structure of the interaction Lagrangian, guarantees renormalizability, and constrains the possible couplings among fermions, gauge fields, and scalar fields. Together, these principles determine the form of the fundamental interactions, the particle content of the SM, and the mechanism through which particle masses arise.

The Strong Interaction: $SU(3)_C$

The color gauge group $SU(3)_C$ describes Quantum Chromodynamics (QCD) [33, 34], the theory of the strong interaction between quarks and gluons. The generalized form of the Lagrangian [1, 25, 35] is,

$$\mathcal{L} = \sum_q \bar{\psi}_{q,a} \left(i\gamma^\mu D_{\mu,ab} - m_q \delta_{ab} \right) \psi_{q,b} - \frac{1}{4} \sum_{A=1}^{8} F^A_{\mu\nu} F^{A\,\mu\nu}. \tag{1.3}$$

Here, $\psi_{q,a}$ represents the quark fields with mass m_q with a color-index a from 1 to $N_c = 3$. For convenience, the summation symbol ($\sum$) will be omitted when

summing over repeated indices with identical superscripts. The γ^μ are the Dirac γ-matrices and $D_{\mu,ab}$ is the covariant derivative:

$$D_{\mu,ab} = \partial_\mu \delta_{ab} + i g_s (t^A_{ab}) G^A_\mu \,. \tag{1.4}$$

where g_s denotes the strong coupling constant, and G^A_μ $(A = 1, \ldots, 8)$ are the gluon fields. The t^A_{ab} are the generators of the $SU(3)$ group in the fundamental representation, expressed as eight 3×3 Hermitian matrices. A convenient choice is $t^A \equiv \lambda^A/2$, where λ^A are the Gell-Mann matrices. The corresponding field-strength tensor $F^A_{\mu\nu}$ is defined as

$$F^A_{\mu\nu} = \partial_\mu G^A_\nu - \partial_\nu G^A_\mu - g_s f_{ABC} G^B_\mu G^C_\nu \,. \tag{1.5}$$

where f^{ABC} are the structure constants of the $SU(3)$ group, defined through the commutation relation

$$[t^A, t^B] = i f^{ABC} t^C \,. \tag{1.6}$$

The QCD Lagrangian remains invariant under local $SU(3)$ gauge transformations of the quark fields:

$$\psi \;\rightarrow\; \psi' = e^{-i g_s \, t^A \, \theta^A(x)} \, \psi \,, \tag{1.7}$$

where $\theta^A(x)$ are the local gauge parameters. The non-Abelian nature of the $SU(3)$ symmetry introduces nonlinear terms in the gluon field-strength tensor, leading to self-interactions among the gluons. These gluon self-couplings give rise to two hallmark phenomena of QCD:

- **Asymptotic freedom:** the effective coupling decreases with increasing

energy scale, allowing for perturbative calculations at high energies;

- **Confinement:** color-charged particles cannot exist in isolation—only color-singlet bound states (hadrons) are observed experimentally.

Both properties have been firmly established through experimental evidence, notably in deep inelastic scattering and jet production processes, and form the cornerstone of our modern understanding of the strong interaction [1].

The Electroweak Interaction: $SU(2)_L \times U(1)_Y$

The electroweak theory unifies the weak and electromagnetic interactions within the gauge group $SU(2)_L \times U(1)_Y$ [31, 36–38]. The left-handed fermions form weak isospin doublets, while right-handed fermions are singlets:

$$Q_L = \begin{pmatrix} u \\ d \end{pmatrix}_L , \quad L_L = \begin{pmatrix} \nu \\ e \end{pmatrix}_L , \quad u_R,\, d_R,\, e_R. \tag{1.8}$$

Here, $SU(2)_L$ symmetry acts exclusively on left-handed fermions under this group. This chiral structure gives rise to the maximal violation of parity observed in weak interactions. The additional $U(1)_Y$ factor corresponds to the weak hypercharge, which, together with the weak isospin, determines the electric charge of each particle through the Gell-Mann–Nishijima relation (see Eq. **1.13**).

One can separate the electroweak Lagrangian into two main components: the Yang–Mills (symmetric) and fermion matter fields part, $\mathcal{L}_{\text{symm}}$, and the Higgs fields sector, $\mathcal{L}_{\text{Higgs}}$, which includes the dynamics of the scalar field and its couplings to gauge bosons and fermions.

The $\mathcal{L}_{\text{symm}}$ describes the kinetic and interaction terms of the gauge and fermion fields. It embodies the non-Abelian gauge theory based on the group $SU(2)_L \otimes$

$U(1)_Y$ with fermionic matter content:

$$\begin{aligned}\mathcal{L}_{\text{symm}} &= -\frac{1}{4}\sum_{A=1}^{3} F^A_{\mu\nu}F^{A\mu\nu} - \frac{1}{4}B_{\mu\nu}B^{\mu\nu} + \bar{\psi}_L i\gamma^\mu D_\mu \psi_L \\ &\quad + \bar{\psi}_R i\gamma^\mu D_\mu \psi_R \ . \end{aligned} \tag{1.9}$$

Here, the Dirac spinor ψ collectively represents all quark and lepton fields. To incorporate with the chiral nature of weak interactions, the fermion fields are decomposed into left- and right-handed components using the projection operators:

$$\psi_{L,R} = \frac{1 \mp \gamma_5}{2}\,\psi, \qquad \bar{\psi}_{L,R} = \bar{\psi}\,\frac{1 \pm \gamma_5}{2}. \tag{1.10}$$

The operators $(1 \mp \gamma_5)/2$, conventionally denoted as P_L and P_R, project ψ onto its left- and right-handed chiral states, which transform differently under the electroweak gauge group. In particular, only left-handed fermions participate in weak charged-current interactions. Notice that the mass term $m\bar{\psi}\psi$ violates the invariance under the $SU(2)_L$ gauge transformation.

The tensors $F^A_{\mu\nu}$ and $B_{\mu\nu}$ represent the field strength tensors of $SU(2)_L$ and $U(1)_Y$, respectively. Their explicit forms are given by

$$B_{\mu\nu} = \partial_\mu B_\nu - \partial_\nu B_\mu \quad \text{and} \quad F^A_{\mu\nu} = \partial_\mu W^A_\nu - \partial_\nu W^A_\mu - g\epsilon_{ABC}\, W^B_\mu W^C_\nu \,, \tag{1.11}$$

where g is the $SU(2)_L$ gauge coupling and ϵ^{ABC} are the structure constants of the $SU(2)$ Lie algebra. The gauge fields B_μ and W^A_μ correspond to the generators of the groups $U(1)_Y$ and $SU(2)_L$, respectively. The $U(1)_Y$ field B_μ is associated with the hypercharge operator $Y_{L,R}$, while the three $SU(2)_L$ fields W^A_μ $(A = 1, 2, 3)$ are associated with the weak isospin generators $t^A_{L,R}$.

The commutation relations among the generators of the $SU(2)$ algebra take the form

$$[\, t_L^A,\, t_L^B \,] = i\, \epsilon^{ABC} t_L^C, \qquad [\, t_R^A,\, t_R^B \,] = i\, \epsilon^{ABC} t_R^C, \tag{1.12}$$

Adopting the normalization convention $\mathrm{Tr}\big[t^A t^B\big] = \frac{1}{2}\delta^{AB}$, the generators in the fundamental representation are expressed in terms of the Pauli matrices as $t_L^A = \frac{1}{2}\,\sigma^A$. Right-handed fermions, being singlets under $SU(2)_L$, transform only under the abelian $U(1)_Y$ group.

The electric charge operator Q is related to the weak isospin and hypercharge through the Gell-Mann–Nishijima [39, 40] relation,

$$Q = t_L^3 + \frac{1}{2} Y_L = t_R^3 + \frac{1}{2} Y_R, \tag{1.13}$$

which unifies the description of the electromagnetic and weak interactions within the electroweak framework. The corresponding weak quantum numbers for the Standard Model fermions are summarized in Table **1.2**.

	t	t_3	Y	Q
ν_L	$\frac{1}{2}$	$\frac{1}{2}$	-1	0
e_L	$\frac{1}{2}$	$-\frac{1}{2}$	-1	-1
e_R	0	0	-2	-1
u_L	$\frac{1}{2}$	$\frac{1}{2}$	$\frac{1}{3}$	$\frac{2}{3}$
d_L	$\frac{1}{2}$	$-\frac{1}{2}$	$\frac{1}{3}$	$-\frac{1}{3}$
u_R	0	0	$\frac{4}{3}$	$\frac{2}{3}$
d_R	0	0	$-\frac{2}{3}$	$-\frac{1}{3}$

Table 1.2: Weak quantum numbers of Standard Model fermions.

The covariant derivatives are defined as

$$D_\mu = \partial_\mu + igt^A_{L,R}W^A_\mu + ig'\frac{1}{2}Y_{L,R}B_\mu, \tag{1.14}$$

where g' is the coupling of $U(1)_Y$ group.

Expanding the term $t^A W^A_\mu$ using

$$W^\pm_\mu = \frac{1}{\sqrt{2}}\left(W^1_\mu \mp i\, W^2_\mu\right), \qquad t^\pm = \frac{1}{\sqrt{2}}\left(t^1 \pm i\, t^2\right), \tag{1.15}$$

we obtain

$$t^A W^A_\mu = t^+ W^+_\mu + t^- W^-_\mu + t^3 W^3_\mu. \tag{1.16}$$

Here, $W^\pm_\mu$ correspond to the charged W bosons, while $t^\pm$ act as the raising and lowering operators of the weak isospin algebra.

To unify the electromagnetic and weak interactions, the neutral gauge fields W_μ^3 and B_μ must combine to yield the physical photon and Z boson fields. The interaction term involving the neutral components, $i\left(g\, t^3 W_\mu^3 + g'\, \frac{1}{2} Y B_\mu\right)$, can be identified with the electromagnetic coupling $ieQA_\mu$. This correspondence is achieved by introducing a rotation between the weak eigenstates (W_μ^3, B_μ) and the physical mass eigenstates (Z_μ, A_μ):

$$\begin{pmatrix} Z_\mu \\ \\ A_\mu \end{pmatrix} = \begin{pmatrix} \cos\theta_W & \sin\theta_W \\ \\ -\sin\theta_W & \cos\theta_W \end{pmatrix} \begin{pmatrix} W_\mu^3 \\ \\ B_\mu \end{pmatrix}, \tag{1.17}$$

where θ_W is the weak mixing angle (also known as the Weinberg angle). From this rotation, the couplings are related by

$$g\, \sin\theta_W = g'\, \cos\theta_W = e, \tag{1.18}$$

which establishes the link between the electroweak gauge couplings (g, g') and the elementary electric charge e.

Thus, the interaction part of the Lagrangian $\mathcal{L}_{\text{symm}}$ can be expressed in terms of the physical gauge fields as

$$-\mathcal{L} = e\, J^\mu A_\mu + \frac{1}{2}\left(J_L^{+\mu} W_\mu^+ + J_L^{-\mu} W_\mu^-\right) + g_Z\, J_Z^\mu Z_\mu\,, \tag{1.19}$$

where the corresponding fermionic currents are defined as

$$J^{\mu} = \bar{\psi}\,\gamma^{\mu} Q\,\psi,$$

$$J_L^{\pm\mu} = \sqrt{2}\,\bar{\psi}\,\gamma^{\mu} t_L^{\pm}\psi,$$

$$J_Z^{\mu} = \bar{\psi}\,\gamma^{\mu}\left(t_L^3 - \sin^2\theta_W\, Q\right)\psi.$$

Here, J^{μ} represents the electromagnetic current, $J_L^{\pm\mu}$ correspond to the charged weak currents, and J_Z^{μ} is the neutral weak current. The coupling constants satisfy the relation

$$g_Z \sin\theta_W \cos\theta_W = e\,, \tag{1.20}$$

Higgs Mechanism

Mass terms are forbidden in the $\mathcal{L}_{\text{symm}}$ sector by the requirements of gauge invariance and renormalizability. However, the experimental observation that the weak gauge bosons $W^{\pm}$ and Z are massive implies the existence of an additional mechanism responsible for generating these masses, as well as those of the fermions. This mechanism is incorporated through the Higgs sector of the electroweak Lagrangian.

To generate the mass terms for the vector bosons $W^{\pm}$ and Z, a scalar doublet ϕ is introduced [41],

$$\phi = \begin{pmatrix} \phi^{+} \\ \phi^{0} \end{pmatrix}. \tag{1.21}$$

The Lagrangian for the scalar field is given as,

$$\mathcal{L}_H = (D_{\mu}\phi)^{\dagger} D^{\mu}\phi - V(\phi^{\dagger}\phi)\,, \tag{1.22}$$

where the potential $V(\phi^\dagger\phi)$ is invariant under $SU(2)_L \otimes U(1)_Y$ gauge symmetry. To preserve renormalizability, the potential includes at most quartic terms in the scalar field,

$$V(\phi^\dagger\phi) = -\frac{1}{2}\mu^2\phi^\dagger\phi + \frac{1}{4}\lambda|\phi^\dagger\phi|^2\,. \tag{1.23}$$

where μ^2 and λ are real parameters, with $\lambda > 0$ ensuring that the potential is bounded from below.

For $\mu^2 > 0$, the potential does not have a global minimum at $|\phi^0| = 0$, as illustrated in Fig. **1.2**. Instead, it attains degenerate minima at $|\phi^0| = \pm v$, where $v = \sqrt{\mu^2/\lambda}$, indicating that the vacuum expectation value (VEV) of the neutral component of the scalar field is nonzero. Expanding the Higgs field around this vacuum configuration selects a particular ground state,

$$\langle\phi\rangle = \frac{1}{\sqrt{2}}\begin{pmatrix}0\\ \\ v\end{pmatrix}, \tag{1.24}$$

which spontaneously breaks the $SU(2)_L \times U(1)_Y$ gauge symmetry down to the electromagnetic subgroup $U(1)_{\text{em}}$. This spontaneous symmetry breaking mechanism gives rise to masses for the weak gauge bosons and fermions while preserving the renormalizability of the theory.

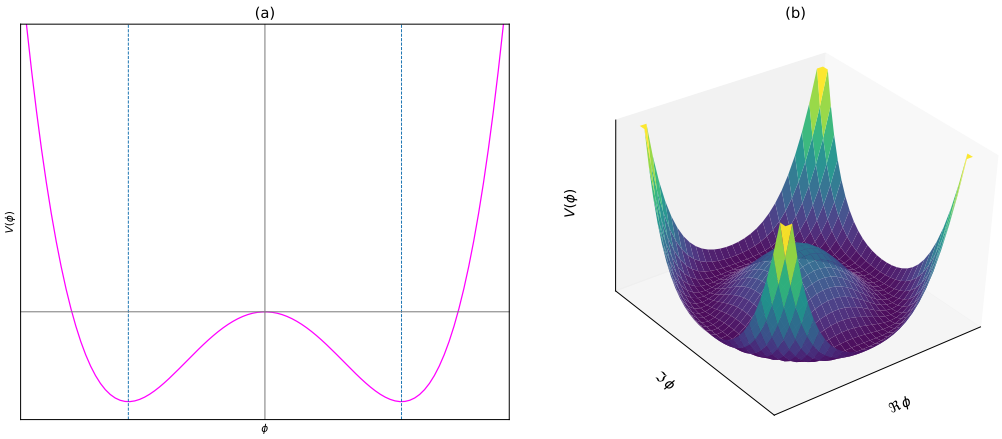


Figure 1.2: Higgs potential with fixed λ and μ^2 for (a) $\Im\ \phi = 0$ and (b) general ϕ.

We can now define the scalar doublet as [25],

$$\phi(x) = \begin{pmatrix} \phi^+ \\ \phi^0 \end{pmatrix} = \exp(i\frac{\xi^A(x)t^A}{2v}) \begin{pmatrix} 0 \\ (v + h(x))/\sqrt{2} \end{pmatrix} . \tag{1.25}$$

where $h(x)$ and $\xi^A(x)$ $(A = 1, 2, 3)$ are real scalar fields, each having a vanishing VEV. The fields $\xi^A(x)$ represent the would-be Goldstone bosons, which are absorbed by the gauge fields to provide the longitudinal components of the now massive vector bosons $W^\pm$ and Z [25, 42].

In the Unitary gauge, the three Goldstone bosons $\xi^A(x)$ are "eaten" by the gauge fields, leaving only the physical neutral scalar field $h(x)$. The Higgs doublet then reduces to

$$\phi(x) = \frac{1}{\sqrt{2}} \begin{pmatrix} 0 \\ v + h \end{pmatrix} , \tag{1.26}$$

where, for convenience, we denote $h(x)$ simply as h.

To determine the masses of the gauge bosons and their couplings to the Higgs

field, we examine the term $(D_\mu\phi)^\dagger D^\mu\phi$ in Eq. **1.22**, where the covariant derivative is given by

$$D_\mu\phi = \left[\partial_\mu + ieQA_\mu + i\frac{1}{\sqrt{2}}g(t^+W_\mu^+ + t^-W_\mu^-) + ig_Z(\frac{1}{2}t^3 - \sin^2\theta_W Q)Z_\mu\right]\phi\,. \tag{1.27}$$

Requiring that the photon remain massless is equivalent to imposing the condition of an electrically neutral vacuum:

$$Q|v\rangle = (t^3 + \frac{1}{2}Y)|v\rangle = 0\ . \tag{1.28}$$

Applying the covariant derivative to $\phi(x)$ yields

$$D_\mu\phi = \frac{1}{\sqrt{2}}\begin{pmatrix} \frac{ig}{\sqrt{2}}W_\mu^+(v+h) \\ \partial_\mu h - \frac{ig_Z}{2}Z_\mu(v+h)\end{pmatrix}. \tag{1.29}$$

Substituting this into the kinetic term leads to

$$\begin{aligned}\mathcal{L}_H = &\frac{1}{2}(\partial_\mu h)(\partial^\mu h) + \frac{1}{4}g^2v^2W^+W^- + \frac{1}{8}g_Z^2v^2ZZ \\ &+ \frac{1}{4}g^2h^2W^+W^- + \frac{1}{8}g_Z^2h^2ZZ + \frac{1}{2}g^2vhW^+W^- + \frac{1}{4}g_Z^2vhZZ \\ &- \left[\frac{1}{2}\mu^2(v+h)^2 + \frac{1}{4}\lambda(v+h)^4\right],\end{aligned}$$

which explicitly displays the gauge boson mass terms, the Higgs self-interaction, and the trilinear and quartic couplings between the Higgs field and the gauge bosons. From the quadratic terms in the gauge fields, we obtain the masses of the weak bosons:

$$M_W = \frac{1}{2}gv, \qquad M_Z = \frac{1}{2}g_Zv. \tag{1.30}$$

These relations show that the $W^{\pm}$ and Z bosons acquire masses proportional to the vacuum expectation value v, with $v = 246.1$ GeV, while the photon remains massless, consistent with the unbroken $U(1)_{\rm em}$ gauge symmetry.

Fermion masses are given by the Yukawa interaction term $\mathcal{L}_Y$. As discussed earlier, in the $SU(2)_L \otimes U(1)_Y$ electroweak theory, a direct fermion mass term of the form $m\,(\bar{\psi}_L\psi_R + \bar{\psi}_R\psi_L)$ would explicitly violate gauge invariance, since ψ_L and ψ_R transform differently under the gauge group. When the Higgs doublet acquires a nonzero vacuum expectation value and spontaneously breaks the electroweak symmetry, it simultaneously induces effective mass terms for the fermions through the Yukawa interaction.

For the leptons, the Yukawa Lagrangian in unitary gauge can be written as [25]

$$\mathcal{L}_{Y\ell} = -\frac{y_\ell}{\sqrt{2}}\, v\,(\bar{\ell}_L\ell_R + \bar{\ell}_R\ell_L) - \frac{y_\ell}{\sqrt{2}}\, h\,(\bar{\ell}_L\ell_R + \bar{\ell}_R\ell_L), \qquad \textbf{(1.31)}$$

where $\ell = e, \mu, \tau$. The first term generates the lepton masses,

$$m_\ell = \frac{y_\ell v}{\sqrt{2}}, \qquad \textbf{(1.32)}$$

while the second term describes the coupling of the physical Higgs boson to fermions, with a strength proportional to the fermion mass. Here, y_ℓ denotes the lepton Yukawa couplings.

For quarks, the weak eigenstates in the unbroken gauge phase are defined as

$$Q_{iL} \equiv \begin{pmatrix} u_i \\ \\ d_i \end{pmatrix}_L, \quad u_{iR},\ d_{iR}, \qquad i = 1, 2, 3\,.$$

It is important to note that, in the interaction basis, these weak eigenstates are

not identical to the physical quark mass eigenstates observed experimentally. The most general $SU(2)_L \otimes U(1)_Y$–invariant Yukawa Lagrangian for the quark sector is given by [25]

$$\mathcal{L}_{Yq} = -\sum_{i=1}^{3}\sum_{j=1}^{3}\left[Y_{ij}^{U}\,\bar{u}_{iR}\,\tilde{\phi}^{\dagger}Q_{jL} + Y_{ij}^{D}\,\bar{d}_{iR}\,\phi^{\dagger}Q_{jL}\right] + \text{H.c.}\,, \qquad (\mathbf{1.33})$$

where

$$\tilde{\phi} = i\,t^2\,\phi^* = \begin{pmatrix} \phi^{0*} \\ -\phi^- \end{pmatrix}$$

is the charge-conjugated Higgs doublet.

After spontaneous symmetry breaking, when the Higgs field acquires its vacuum expectation value, the Yukawa interactions generate the quark mass terms:

$$(\bar{u}_1,\,\bar{u}_2,\,\bar{u}_3)_R\,\mathcal{M}^U \begin{pmatrix} u_1 \\ u_2 \\ u_3 \end{pmatrix}_L + (\bar{d}_1,\,\bar{d}_2,\,\bar{d}_3)_R\,\mathcal{M}^D \begin{pmatrix} d_1 \\ d_2 \\ d_3 \end{pmatrix}_L + \text{H.c.},$$

where

$$\mathcal{M}_{ij}^{U} = \frac{v}{\sqrt{2}}\,Y_{ij}^{U}, \qquad \mathcal{M}_{ij}^{D} = \frac{v}{\sqrt{2}}\,Y_{ij}^{D},$$

are the up- and down-type quark mass matrices, respectively. These matrices are, in general, complex and non-Hermitian. They can be diagonalized by independent unitary transformations on the left- and right-handed quark fields, which rotate

from the interaction (weak) basis to the physical (mass) basis in the broken phase:

$$\begin{pmatrix} u_1 \\ u_2 \\ u_3 \end{pmatrix}_{L,R} = U_{L,R} \begin{pmatrix} u \\ c \\ t \end{pmatrix}, \qquad \begin{pmatrix} d_1 \\ d_2 \\ d_3 \end{pmatrix}_{L,R} = D_{L,R} \begin{pmatrix} d \\ s \\ b \end{pmatrix}. \tag{1.34}$$

The mass matrices are diagonalized by bi-unitary transformations of the form

$$U_R^\dagger \, \mathcal{M}^U \, U_L = \begin{pmatrix} m_u & 0 & 0 \\ 0 & m_c & 0 \\ 0 & 0 & m_t \end{pmatrix}, \qquad D_R^\dagger \, \mathcal{M}^D \, D_L = \begin{pmatrix} m_d & 0 & 0 \\ 0 & m_s & 0 \\ 0 & 0 & m_b \end{pmatrix}.$$

The weak eigenstates u_i and d_i are thus linear combinations of the mass eigenstates u, c, t and d, s, b, with different unitary transformations for left- and right-handed components.

In the broken phase, rewriting the Yukawa Lagrangian in terms of the quark mass eigenstates gives

$$\mathcal{L}_{Yq} = -\frac{1}{\sqrt{2}} \left[\sum_{q_u = u,c,t} \kappa^U_{q_u} \, \bar{q}_u q_u \, (v + h) + \sum_{q_d = d,s,b} \kappa^D_{q_d} \, \bar{q}_d q_d \, (v + h) \right],$$

where the Yukawa couplings are related to the quark masses by

$$\kappa^U_{q_u} = \frac{\sqrt{2}\, m_{q_u}}{v}, \qquad \kappa^D_{q_d} = \frac{\sqrt{2}\, m_{q_d}}{v}.$$

The diagonalization of the mass matrices eliminates mixing between weak and mass eigenstates in the fermion sector, resulting in flavor-diagonal Yukawa interactions at tree level in the Standard Model.

However, the misalignment between the weak and mass eigenstates manifests in the charged-current interactions. Specifically,

$$(\bar{u}_1,\, \bar{u}_2,\, \bar{u}_3)_L\, \gamma^\mu \begin{pmatrix} d_1 \\ d_2 \\ d_3 \end{pmatrix}_L = (\bar{u},\, \bar{c},\, \bar{t})_L\, U_L^\dagger D_L\, \gamma^\mu \begin{pmatrix} d \\ s \\ b \end{pmatrix}_L .$$

We define

$$V \equiv U_L^\dagger D_L,$$

which is the Cabibbo–Kobayashi–Maskawa (CKM) matrix. This unitary matrix encodes all flavor-changing effects in the charged-current weak interaction.

1.2 Needs for New Physics

Despite its remarkable success, the Standard Model (SM) is widely regarded as an incomplete description of nature. Although it accurately accounts for an enormous range of experimental observations, it does not incorporate gravity, dark matter, or dark energy. In addition, several fundamental phenomena remain unexplained within its framework. Two of the most striking open issues are the observed baryon asymmetry of the Universe and a series of flavor anomalies in the decays of heavy mesons. Both point toward the need for new physics beyond the SM (BSM).

1.2.1 Baryon Asymmetry of the Universe

Cosmological and astrophysical observations indicate that the present Universe is overwhelmingly composed of matter, with an exceedingly small abundance of

antimatter. This imbalance is quantified by the baryon-to-photon ratio, defined as

$$\eta_B \equiv \frac{n_B}{n_\gamma} \simeq 2.75 \times 10^{-8}\, \Omega_b h^2 \simeq 6.16 \times 10^{-10}, \qquad (\mathbf{1.35})$$

where n_B is the baryon number density and $n_\gamma = 4.11 \times 10^{-8}\,\mathrm{cm}^{-3}$ is the photon number density. The parameter $\Omega_b h^2 = 0.0224 \pm 0.0001$, denotes the baryon density of the Universe, determined from measurements of the cosmic microwave background and Big Bang nucleosynthesis [43].

Within the Standard Model, the generation of such an asymmetry requires three conditions, known as the *Sakharov criteria* [44]:

1. violation of baryon number (B);
2. violation of charge conjugation (C) and charge–parity (CP) symmetries;
3. departure from thermal equilibrium.

Although the Standard Model satisfies these conditions in principle, the magnitude of CP violation and the strength of the electroweak phase transition are insufficient to explain the observed baryon asymmetry of the Universe, falling short by several orders of magnitude [45]. This discrepancy strongly indicates the need for additional sources of CP violation or new dynamics beyond the Standard Model—such as extended Higgs sectors, heavy neutrino mechanisms (leptogenesis), or new interactions at the TeV scale that could strengthen the electroweak phase transition.

1.2.2 Flavor Anomalies

In parallel, precise measurements of flavor-changing processes in the quark and lepton sectors have revealed several tensions with SM predictions. Particularly

notable are anomalies observed in semileptonic B-meson decays, such as the lepton flavor universality ratios

$$R_{K^{(*)}} = \frac{\mathcal{B}(B \to K^{(*)}\mu^+\mu^-)}{\mathcal{B}(B \to K^{(*)}e^+e^-)}, \qquad R_{D^{(*)}} = \frac{\mathcal{B}(B \to D^{(*)}\tau\nu)}{\mathcal{B}(B \to D^{(*)}\ell\nu)}, \tag{1.36}$$

where $\ell = e$, μ. Experimental results from LHCb (Large Hadron Collider beauty), Belle, and BaBar show deviations at the level of 2–3σ from SM expectations [46, 47]. In addition, angular observables in $B \to K^*\mu^+\mu^-$ decays, along with anomalies observed in rare processes such as $b \to s\ell^+\ell^-$ transitions, suggest possible violations of lepton flavor universality and hint at contributions from new vector or scalar interactions [48].

If confirmed with higher statistics, these anomalies could point toward new degrees of freedom, such as leptoquarks, Z' bosons, or extended Higgs sectors that couple non-universally to fermions. Together with the baryon asymmetry of the Universe, these observations provide strong motivation for exploring extensions of the Standard Model, including scenarios with additional Higgs fields, new gauge interactions, or flavor-dependent couplings.

1.3 General Two Higgs Doublet Model

To address the observed deviations from the Standard Model, one of the simplest and most well-motivated approaches is to extend the scalar sector by introducing an additional $SU(2)_L$ Higgs doublet. After electroweak symmetry breaking, this framework yields five physical Higgs bosons: two CP-even scalars, the lighter h^0 and the heavier H^0; one CP-odd pseudoscalar, A^0; and a charged pair, $H^\pm$. The presence of two scalar doublets allows for new sources of CP

violation and introduces an additional set of Yukawa interactions, which can give rise to flavor-changing neutral currents (FCNCs).

1.3.1 Modified Higgs Potential

With two $Y = 1$ $SU(2)_L$ Higgs doublets ($\Phi_{1,2}$), the most general gauge invariant Higgs potential for the general two-Higgs doublet extension of the SM is given by [49]:

$$\begin{aligned}\mathcal{V} &= m_{11}^2\,\Phi_1^\dagger\Phi_1 + m_{22}^2\,\Phi_2^\dagger\Phi_2 - \Big[m_{12}^2\,\Phi_1^\dagger\Phi_2 + \text{H.c.}\Big] \\ &+ \tfrac{1}{2}\lambda_1(\Phi_1^\dagger\Phi_1)^2 + \tfrac{1}{2}\lambda_2(\Phi_2^\dagger\Phi_2)^2 + \lambda_3(\Phi_1^\dagger\Phi_1)(\Phi_2^\dagger\Phi_2) + \lambda_4(\Phi_1^\dagger\Phi_2)(\Phi_2^\dagger\Phi_1) \\ &+ \Big\{\tfrac{1}{2}\lambda_5(\Phi_1^\dagger\Phi_2)^2 + \big[\lambda_6(\Phi_1^\dagger\Phi_1) + \lambda_7(\Phi_2^\dagger\Phi_2)\big]\Phi_1^\dagger\Phi_2 + \text{H.c.}\Big\}, \qquad (\mathbf{1.37})\end{aligned}$$

In general, m_{12}^2 and $\lambda_{5,6,7}$ can be complex, whereas the remaining parameters are real. The Higgs doublets Φ_1 and Φ_2 are defined in the interaction (Yukawa) basis as

$$\Phi_1 = \begin{pmatrix} \phi_1^+ \\ \frac{1}{\sqrt{2}}(\phi_1^0 + v_1 + i\text{Im}\phi_1^0) \end{pmatrix}, \quad \Phi_2 = \begin{pmatrix} \phi_2^+ \\ \frac{1}{\sqrt{2}}(\phi_2^0 + v_2 + i\text{Im}\phi_2^0) \end{pmatrix},$$

with non-vanishing vacuum expectation values (VEVs)

$$\langle\Phi_1\rangle = \frac{1}{\sqrt{2}}\begin{pmatrix} 0 \\ v_1 \end{pmatrix}, \quad \langle\Phi_2\rangle = \frac{1}{\sqrt{2}}\begin{pmatrix} 0 \\ v_2 \end{pmatrix}.$$

The two vacuum expectation values satisfy $v_1^2 + v_2^2 = v^2$, where $\tan\beta \equiv v_2/v_1$. Here, v denotes the electroweak vacuum expectation value in the Higgs basis. This

transformation can be expressed as

$$\begin{pmatrix} v_1 \\ v_2 \end{pmatrix} = \begin{pmatrix} \cos\beta & -\sin\beta \\ \sin\beta & \cos\beta \end{pmatrix} \begin{pmatrix} v \\ 0 \end{pmatrix}. \tag{1.38}$$

Applying this transformation to the charged and CP-odd scalar components, we can write the two Higgs doublets as [50]

$$\begin{aligned} \Phi_1 &= \frac{1}{\sqrt{2}} \begin{pmatrix} \sqrt{2}\left(G^+\cos\beta - H^+\sin\beta\right) \\ v\cos\beta + \phi_1^0 + i\left(G^0\cos\beta - A^0\sin\beta\right) \end{pmatrix}, \\ \Phi_2 &= \frac{1}{\sqrt{2}} \begin{pmatrix} \sqrt{2}\left(G^+\sin\beta + H^+\cos\beta\right) \\ v\sin\beta + \phi_2^0 + i\left(G^0\sin\beta - A^0\cos\beta\right) \end{pmatrix}. \end{aligned}$$

Defining a mixing angle α for the CP-even neutral components,

$$\begin{pmatrix} \phi_1^0 \\ \phi_2^0 \end{pmatrix} = \begin{pmatrix} \cos\alpha & -\sin\alpha \\ \sin\alpha & \cos\alpha \end{pmatrix} \begin{pmatrix} H^0 \\ h^0 \end{pmatrix}, \tag{1.39}$$

the electroweak symmetry breaking (EWSB) results in five physical scalar states: two neutral CP-even scalars (H^0 and h^0), one CP-odd pseudoscalar (A^0), and a pair of charged Higgs bosons ($H^\pm$). The remaining fields, $G^\pm$ and G^0, are the three Goldstone bosons that are absorbed as the longitudinal components of the weak gauge bosons $W^\pm$ and Z^0.

Finally, the two Higgs doublets can be expressed in terms of the physical fields

as

$$\Phi_1 = \frac{1}{\sqrt{2}} \begin{pmatrix} \sqrt{2}\,(G^+ c_\beta - H^+ s_\beta) \\ H^0 c_\alpha - h^0 s_\alpha + v c_\beta + i\,(G^0 c_\beta - A^0 s_\beta) \end{pmatrix}, \quad \textbf{(1.40)}$$

$$\Phi_2 = \frac{1}{\sqrt{2}} \begin{pmatrix} \sqrt{2}\,(G^+ s_\beta + H^+ c_\beta) \\ H^0 s_\alpha + h^0 c_\alpha + v s_\beta + i\,(G^0 s_\beta + A^0 c_\beta) \end{pmatrix}, \quad \textbf{(1.41)}$$

where $s_{\beta,\alpha} \equiv \sin\beta, \alpha$ and $c_{\beta,\alpha} \equiv \cos\beta, \alpha$.

Then the tree-level Higgs masses can be expressed according to the remaining potential parameters of Eq. (**1.37**). For the CP-odd scalar A^0, the mass is given by

$$m_A^2 = \frac{m_{12}^2}{s_\beta c_\beta} - \lambda_5 v^2 \ . \quad \textbf{(1.42)}$$

The CP-even Higgs mass matrix in the (ϕ_1^0, ϕ_2^0) basis is

$$M^2 = m_A^2 \begin{pmatrix} s_\beta^2 & -s_\beta c_\beta \\ -s_\beta c_\beta & c_\beta^2 \end{pmatrix} + v^2 \begin{pmatrix} \lambda_1 c_\beta^2 + \lambda_5 s_\beta^2 & (\lambda_3 + \lambda_4) s_\beta c_\beta \\ (\lambda_3 + \lambda_4) s_\beta c_\beta & \lambda_2 s_\beta^2 + \lambda_5 c_\beta^2 \end{pmatrix}, \quad \textbf{(1.43)}$$

Diagonalizing this matrix yields the CP-even Higgs boson masses:

$$m_H^2 = \frac{1}{2}\left[M_{11}^2 + M_{22}^2 + \sqrt{(M_{11}^2 - M_{22}^2)^2 + 4(M_{12}^2)^2} \right], \quad \textbf{(1.44)}$$

$$m_h^2 = \frac{1}{2}\left[M_{11}^2 + M_{22}^2 - \sqrt{(M_{11}^2 - M_{22}^2)^2 + 4(M_{12}^2)^2} \right], \quad \textbf{(1.45)}$$

corresponding to the heavier (H^0) and lighter (h^0) CP-even scalar states, respectively.

Finally, the charged Higgs boson mass is given by

$$m_{H^\pm}^2 = m_A^2 + \frac{1}{2}v^2\,(\lambda_5 - \lambda_4). \tag{1.46}$$

At tree level, the mass relations enable the quartic couplings λ_{1-5} to be re-expressed in terms of the physical parameters—namely, the four Higgs boson masses and the neutral-sector mixing angle $\sin(\beta-\alpha)$. This substitution provides a more convenient set of physical input parameters for phenomenological analysis.

1.3.2 The Yukawa Sector

Assuming CP conservation, the general Yukawa Lagrangian of the G2HDM, written in the interaction basis, takes the form [50]:

$$\begin{aligned} -\mathcal{L}_Y = {} & \overline{Q}_L\widetilde{\Phi}_1\eta_1^U U_R + \overline{Q}_L\Phi_1\eta_1^D D_R + \overline{L}_L\Phi_1\eta_1^L L_R \\ & + \overline{Q}_L\widetilde{\Phi}_2\eta_2^U U_R + \overline{Q}_L\Phi_2\eta_2^D D_R + \overline{L}_L\Phi_2\eta_2^L L_R, \end{aligned} \tag{1.47}$$

where the η_i^F $(i=1,2)$ with $F=\{U,D,L\}$ denote real 3×3 Yukawa coupling matrices. They can be combined into the effective matrices κ^F, defined as

$$\kappa^F \equiv \eta_1^F\cos\beta + \eta_2^F\sin\beta, \tag{1.48}$$

which are real and positive. The κ^F matrices are related to the fermion mass matrices M_F via

$$\kappa^F = \frac{\sqrt{2}}{v}M_F\,,$$

generating the mass to fermions.

Orthogonal to κ^F, we define the matrices ρ^F as

$$\rho^F \equiv -\eta_1^F \sin\beta + \eta_2^F \cos\beta \ , \tag{1.49}$$

which describe additional Yukawa structures beyond those responsible for fermion mass generation.

Performing a rotation to Higgs basis (H_1, H_2)—where only H_1 acquires a nonzero vacuum expectation value (VEV)—the Yukawa Lagrangian can be rewritten as

$$\begin{aligned} -\mathcal{L}_Y =& \overline{Q}_L \widetilde{H}_1 \kappa^U U_R + \overline{Q}_L H_1 \kappa^D D_R + \overline{Q}_L H_1 \kappa^L L_R & (1.50)\\ &+ \overline{Q}_L \widetilde{H}_2 \rho^U U_R + \overline{Q}_L H_2 \rho^D D_R + \overline{Q}_L H_2 \rho^L L_R. & (1.51) \end{aligned}$$

Here, H_1 (with vev $v_1 = v$) is responsible for fermion mass generation and couples through κ^F, while H_2 (with $v_2 = 0$) couples through ρ^F and mediates potential flavor-changing effects.

Transforming to the physical (mass) basis, the Yukawa interactions of the neutral and charged scalars can be expressed as

$$\begin{aligned} -\mathcal{L}_{\rm Y} =& \frac{1}{\sqrt{2}}\overline{D}\Big[\kappa^D s_{\beta-\alpha} + \rho^D c_{\beta-\alpha}\Big] Dh + \frac{1}{\sqrt{2}}\overline{D}\Big[\kappa^D c_{\beta-\alpha} - \rho^D s_{\beta-\alpha}\Big] DH + \frac{\mathrm{i}}{\sqrt{2}}\overline{D}\gamma_5 \rho^D DA \\ &+ \frac{1}{\sqrt{2}}\overline{U}\Big[\kappa^U s_{\beta-\alpha} + \rho^U c_{\beta-\alpha}\Big] Uh + \frac{1}{\sqrt{2}}\overline{U}\Big[\kappa^U c_{\beta-\alpha} - \rho^U s_{\beta-\alpha}\Big] UH - \frac{\mathrm{i}}{\sqrt{2}}\overline{U}\gamma_5 \rho^U UA \\ &+ \frac{1}{\sqrt{2}}\overline{L}\Big[\kappa^L s_{\beta-\alpha} + \rho^L c_{\beta-\alpha}\Big] Lh + \frac{1}{\sqrt{2}}\overline{L}\Big[\kappa^L c_{\beta-\alpha} - \rho^L s_{\beta-\alpha}\Big] LH + \frac{\mathrm{i}}{\sqrt{2}}\overline{L}\gamma_5 \rho^L LA \\ &+ \Big[\overline{U}\big(V_{\rm CKM}\rho^D P_R - \rho^U V_{\rm CKM} P_L\big) DH^+ + \overline{\nu}\rho^L P_R L H^+ + \text{h.c.}\Big]. \end{aligned} \tag{1.52}$$

The general structure of Eq. (**1.52**) leads to tree-level flavor-changing neutral currents (FCNCs) unless the ρ^F matrices are diagonal. A common way to eliminate

Type	U_R	D_R	L_R	ρ^U	ρ^D	ρ^L
I	+	+	+	$\kappa^U \cot\beta$	$\kappa^D \cot\beta$	$\kappa^L \cot\beta$
II	+	−	−	$\kappa^U \cot\beta$	$-\kappa^D \tan\beta$	$-\kappa^L \tan\beta$
III/Y	+	−	+	$\kappa^U \cot\beta$	$-\kappa^D \tan\beta$	$\kappa^L \cot\beta$
IV/X	+	+	−	$\kappa^U \cot\beta$	$\kappa^D \cot\beta$	$-\kappa^L \tan\beta$

Table 1.3: Assignment of Z_2 charges for the right-handed fermions, and the resulting relations among Yukawa coupling matrices in the Z_2-symmetric types of 2HDM Yukawa sectors. The Higgs doublets have Z_2 quantum numbers $-$ (Φ_1) and $+$ (Φ_2).

such FCNCs is to impose a discrete Z_2 symmetry that forbids certain Yukawa terms in Eq. (**1.47**). Under this symmetry, one Higgs doublet and selected right-handed fermion fields are odd, while all others are even. Models implementing this symmetry are classified into the four canonical 2HDM *types*, following the convention of Ref. [51]. The corresponding Z_2 charge assignments and resulting Yukawa coupling structures are summarized in Table **1.3**.

1.4 Summary of Chapter 1

Chapter 1 provides the theoretical framework for this dissertation by reviewing the structure of the SM and introducing the G2HDM as a motivated framework for new physics.

The chapter begins with an overview of the particle content of the SM, including the fermion families, gauge bosons, and the Higgs boson. It then outlines the theoretical structure of the model, focusing on its gauge symmetries, electroweak spontaneous symmetry breaking, fermion mass generation, and the formulation of charged and neutral currents. This section emphasizes how the SM successfully describes a wide range of particle interactions with remarkable precision.

Despite its success, the SM leaves several fundamental questions unsolved.

Section 1.2 highlights key indications for physics beyond the Standard Model. These include the baryon asymmetry of the Universe, which cannot be explained by SM CP violation or the electroweak phase transition, and flavor anomalies in heavy B-Meson decays, that suggest possible contributions from new interactions or particles. These open problems provide strong motivation to explore the extensions of the SM.

The chapter concludes with an introduction to the G2HDM. The G2HDM allows FCNH interactions and can produce extra source for CP-violation. The modified Higgs potential is presented, along with its physical mass eigenstates, mixing angles, and theoretical constraints. The Yukawa sector is then discussed in detail, illustrating how additional Yukawa matrices lead to new scalar–fermion couplings and potentially observable flavor-changing processes, particularly in the top-quark and Higgs sectors.

Together, these elements establish the conceptual and theoretical motivation for the collider studies performed in the later chapters of the dissertation.

Chapter 2

Higgs Signal Channels and Analysis Strategies

The main objective of this dissertation is to explore the discovery prospects of BSM Higgs bosons—including the neutral scalars (H^0, A^0) and the charged Higgs bosons ($H^{\pm}$)—within the framework of the general Two Higgs Doublet Model (G2HDM). In particular, special attention is given to flavor-changing processes, such as the charged Higgs decay channel $H^+ \to c\bar{b}$.

For the neutral sector, we focus on flavor-changing neutral Higgs (FCNH) processes such as $t \to c\phi^0$ with $\phi^0 \to \tau^+\tau^-$, where t and c denote the top and charm quarks, respectively, and ϕ^0 represents either the heavy scalar (H^0) or pseudoscalar (A^0).

Chapter 3 focuses on the detection of the charged Higgs boson through the decay mode $H^+ \to c\bar{b}$. The following Chapter 4 presents detailed study of the discovery potential for $\phi^0 \to \tau^+\tau^-$, along with an analysis of the alternative FCNH channel $\phi^0 \to t\bar{c}$ ($c\bar{t}$).

2.1 Motivations

2.1.1 Charged Higgs Flavor-changing channel

One can extract the H^+cb interaction terms from the Yukawa Lagrangian in Eq. **1.52** and obtain

$$\begin{aligned}\mathcal{L}_{H^+\bar{c}b} =& -\ \bar{c}\left[\left(V_{cd}\rho_{db} + V_{cs}\rho_{sb} + V_{cb}\rho_{bb}\right)P_R - \left(\rho^*_{uc}V_{ub} + \rho^*_{cc}V_{cb} + \rho^*_{tc}V_{tb}\right)P_L\right] b\, H^+ \\ &+ \text{H.c.} \\ \approx& \ \bar{c}\left[\rho^*_{tc}V_{tb}P_L\right] b\, H^+ + \text{H.c.}\ ,\end{aligned} \tag{2.1}$$

where the CKM matrix elements are taken from the latest PDG review [1]:

$$V_{\text{CKM}} = \begin{pmatrix} 0.97435 \pm 0.00016 & 0.22501 \pm 0.00068 & 0.003732^{+0.000090}_{-0.000085} \\ 0.22487 \pm 0.00068 & 0.97349 \pm 0.00016 & 0.04183^{+0.00079}_{-0.00069} \\ 0.00858^{+0.00019}_{-0.00017} & 0.04111^{+0.00077}_{-0.00068} & 0.999118^{+0.000029}_{-0.000034} \end{pmatrix}. \tag{2.2}$$

It follows that the effective coupling $|\lambda_{H^+cb}|$ is proportional to $\rho_{tc}V_{tb}$ (taking ρ matrices as real), and is therefore not suppressed by CKM mixing. In contrast to the flavor-changing neutral Higgs coupling $|\lambda_{tc\phi}|$, this charged-Higgs coupling depends solely on ρ_{tc} rather than $\tilde{\rho}_{tc}$, making the decay channel $H^+ \to c\bar{b}$ free from constraints associated with ρ_{ct}.

Assuming the same heavy Higgs mass degenerate state, we study the decay channels of the charged Higgs boson H^+, focusing in particular on $H^+ \to c\bar{b}$, $H^+ \to t\bar{b}$, and $H^+ \to t\bar{s}$. For $\rho_{ct} = 0.05$, the corresponding branching ratios are calculated with the Two-Higgs-Doublet Model Calculator (2HDMC) [52], which evaluates all kinematically allowed Higgs decay modes in the G2HDM framework,

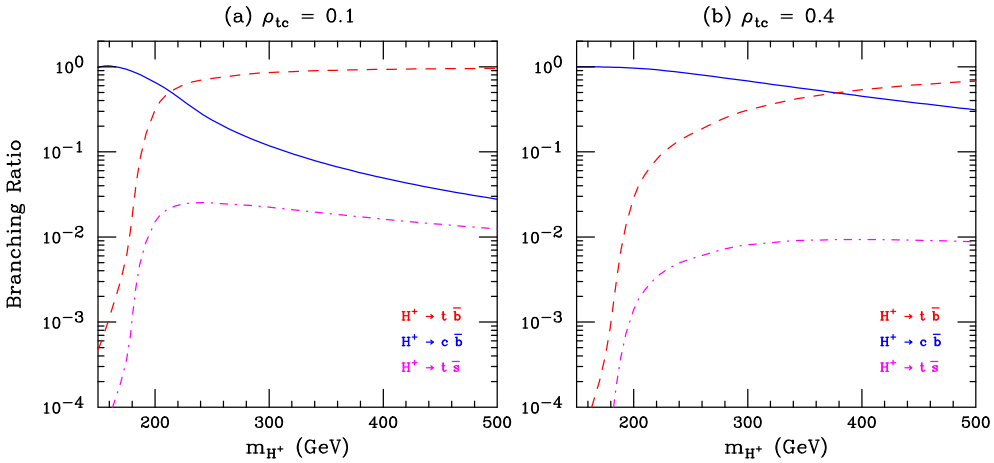


Figure 2.1: Branching ratios of $H^+ \to XY$ as a function of m_{H^+} for (a) $\rho_{tc} = 0.1$, and (b) $\rho_{tc} = 0.4$.

and shown in Fig. **2.1** as functions of m_{H^+}, for fixed values of $\rho_{tc} = 0.1$ (left) and $\rho_{tc} = 0.4$ (right). It can be seen that $H^+ \to t\bar{b}$ becomes the dominant decay mode once $m_{H^+} \gtrsim 200$ GeV, while the $H^+ \to c\bar{b}$ channel remains sizable, particularly for larger ρ_{tc}. The discovery prospects of the process $cg \to bH^+ \to b(c\bar{b})$ will be discussed in detail in Chapter 3.

2.1.2 FCNH signal channels

Similarly, from the Yukawa Lagrangian given in Eq. **1.52**, the effective interaction terms for the neutral Higgs bosons h^0, H^0, and A^0 can be written as

$$\mathcal{L}_{\text{eff}} = -\frac{\lambda_{tch}}{\sqrt{2}}\,\bar{c}t\,h^0 + \frac{\lambda_{tcH}}{\sqrt{2}}\,\bar{c}t\,H^0 + i\frac{\lambda_{tcA}}{\sqrt{2}}\,\bar{c}t\,A^0 + \text{H.c.} \qquad (\mathbf{2.3})$$

where $|\lambda_{tc\phi}|$ (with $\phi = h,\ H,\ A$) denote the effective Yukawa couplings between the neutral Higgs bosons and the $(t,\ c)$ quark pair. These couplings are approximately given by

$$|\lambda_{tch}| \propto \tilde{\rho}_{tc}\, c_{\beta-\alpha}, \qquad |\lambda_{tcH}| \propto \tilde{\rho}_{tc}\, s_{\beta-\alpha}, \qquad |\lambda_{tcA}| \propto \tilde{\rho}_{tc}\,. \qquad (\mathbf{2.4})$$

To reproduce the observed properties of the Standard Model (SM) Higgs boson, we invoke the *alignment limit* [53, 54], in which one of the two CP-even Higgs mass eigenstates in the G2HDM is aligned with the direction of the scalar field vacuum expectation value v. By convention, we identify h^0 as the SM-like Higgs boson, corresponding to $\cos(\beta-\alpha)\approx 0$ and $\sin(\beta-\alpha)\approx 1$.

The effective coupling $\tilde{\rho}_{tc}$ can be related to the fundamental Yukawa couplings as

$$\tilde{\rho}_{tc} \simeq \sqrt{\frac{|\rho_{tc}|^2+|\rho_{ct}|^2}{2}}\,, \tag{2.5}$$

which follows from separating the Yukawa interaction into its CP-even and CP-odd components, denoted respectively by X^F_Φ and $Y^F_\Phi\gamma^5$, where X^F and Y^F are 3×3 matrices in flavor space. The general form of the effective Lagrangian is then written as

$$\mathcal{L} = \sum_{\mathrm{F\,=\,U,D,L}} \bar{F}\left[X^F_\Phi + Y^F_\Phi\gamma_5\right]\Phi\, P_R\, F\,, \tag{2.6}$$

where $\Phi = h^0$, H^0, A^0 denotes the physical neutral Higgs fields.

For each Higgs eigenstate, the explicit forms of X^F_Φ and Y^F_Φ are given as follows:

(i) For $\Phi = h^0$:

$$X^F = \frac{1}{\sqrt{2}}\left[\kappa^F s_{\beta-\alpha} + \frac{\rho^F+\rho^{F\dagger}}{2}\,c_{\beta-\alpha}\right], \qquad Y^F = -\frac{1}{\sqrt{2}}\left[\frac{\rho^F-\rho^{F\dagger}}{2}\,c_{\beta-\alpha}\right].$$

(ii) For $\Phi = H^0$:

$$X^F = \frac{1}{\sqrt{2}}\left[\kappa^F c_{\beta-\alpha} - \frac{\rho^F+\rho^{F\dagger}}{2}\,s_{\beta-\alpha}\right], \qquad Y^F = \frac{1}{\sqrt{2}}\left[\frac{\rho^F-\rho^{F\dagger}}{2}\,s_{\beta-\alpha}\right].$$

(iii) For $\Phi = A^0$:

$$X^F = -\,\mathrm{sgn}(Q_F)\,\frac{i}{\sqrt{2}}\left[\frac{\rho^F - \rho^{F\dagger}}{2}\right], \qquad Y^F = -\,\mathrm{sgn}(Q_F)\,\frac{i}{\sqrt{2}}\left[\frac{\rho^F + \rho^{F\dagger}}{2}\right].$$

Next, consider the decay process $\Phi(p) \to f_i(k_1)\,\bar{f}_j(k_2)$ for $\Phi = H^0$ or A^0. The squared matrix element, summed over spins and colors, is

$$\sum_{\text{spin, color}} |M(\Phi \to f_i \bar{f}_j)|^2 = 4N_c\left[(|X^F_{ij}|^2 + |Y^F_{ij}|^2)(k_1\cdot k_2) - (|X^F_{ij}|^2 - |Y^F_{ij}|^2)m_i m_j\right], \tag{2.7}$$

where N_c is the color factor and $k_{1,2}$ are the fermion momenta. The relevant kinematic relations are

$$\begin{aligned} &2(k_1\cdot k_2) = m_\Phi^2 - m_i^2 - m_j^2\,, \qquad |k_1| = \frac{1}{2m_\Phi}\,\lambda^{1/2}(m_\Phi^2, m_i^2, m_j^2), \\ &\lambda(x,y,z) \equiv x^2 + y^2 + z^2 - 2xy - 2xz - 2yz\,. \end{aligned}$$

The partial decay width is then obtained as

$$\begin{aligned} \Gamma(\Phi \to f_i \bar{f}_j) =& \frac{N_c\,\lambda^{1/2}(m_\Phi^2, m_i^2, m_j^2)}{8\pi m_\Phi^3}\Big[|X^F_{ij}|^2\big(m_\Phi^2 - (m_i + m_j)^2\big) \\ &+ |Y^F_{ij}|^2\big(m_\Phi^2 - (m_i - m_j)^2\big)\Big] \end{aligned} \tag{2.8}$$

Therefore, for the flavor-changing process $\phi \to tc$, where tc denotes both $t\bar{c}$ and $c\bar{t}$ for convenience, neglecting $m_c \ll m_t$, the effective coupling satisfies

$$|\lambda_{tc\phi}|^2 \propto |X^U_{32}|^2 + |Y^U_{32}|^2 \propto \frac{|\rho_{tc}|^2 + |\rho_{ct}|^2}{2}\,. \tag{2.9}$$

For the SM-like Higgs boson h^0, the coupling $|\lambda_{tch}|$ is strongly suppressed by the factor $s_{\beta-\alpha}$ in the alignment limit, which explains the absence of experimental

signals at the Large Hadron Collider (LHC). In contrast, the couplings $|\lambda_{tcH}|$ and $|\lambda_{tcA}|$ remain unsuppressed, making the decay $\phi^0 \to tc$ a promising channel to probe non-standard Higgs bosons beyond the Standard Model.

For the parameter space under consideration, the heavy Higgs states (H^0, A^0, and $H^\pm$) are taken to be degenerate in mass. We choose $c_{\beta-\alpha} = 0.01$ and set $\rho^F_{ii} = \kappa^F_{ii}$, except for the coupling $\rho_{tt} = 0.2 \times m_\phi/(150\text{ GeV})$ [55]. Using the 2HDMC, we compute the branching ratios (BRs) of the dominant decay channels as functions of m_ϕ for both H^0 and A^0, as shown in Fig. **2.2**. We take $\tilde{\rho}_{tc} = 0.1$ and 0.4, neglecting all other off-diagonal elements in ρ^F.

From Fig. **2.2**, we observe that for both H^0 and A^0, once $m_\phi > m_t$, the $\phi^0 \to tc$ channel becomes dominant, suppressing the $\phi^0 \to b\bar{b}$ and $\phi^0 \to \tau^+\tau^-$ modes. When $m_\phi > 2m_t$, the decay $\phi^0 \to t\bar{t}$ opens up and begins to suppress $\phi^0 \to tc$, however, the branching ratio $\text{BR}(\phi^0 \to tc)$ remains sizable for larger values of $\tilde{\rho}_{tc}$.

Therefore, we investigate two distinct FCNH final states, each targeting different mass ranges of H^0 and A^0. Taking $m_\phi = 200$ GeV as a reference point, we study $pp \to \bar{t}t \to \bar{t}c\phi^0 \to (\bar{b}jj)\,(c\tau^+\tau^-) + X$ for 130 GeV $\leq m_\phi \leq$ 200 GeV, and $pp \to t\phi^0 \to t(tc)$ for 200 GeV $\leq m_\phi \leq$ 500 GeV, respectively. A more detailed analysis of both discovery channels will be presented in Chapter 4.

2.2 Analysis Tools and Strategies

2.2.1 Analytical Tools

Accurate estimation of cross sections in high-energy particle collisions requires evaluating multidimensional integrals that arise from the phase space formulation of the scattering process. The analytical computation of these integrals is nearly

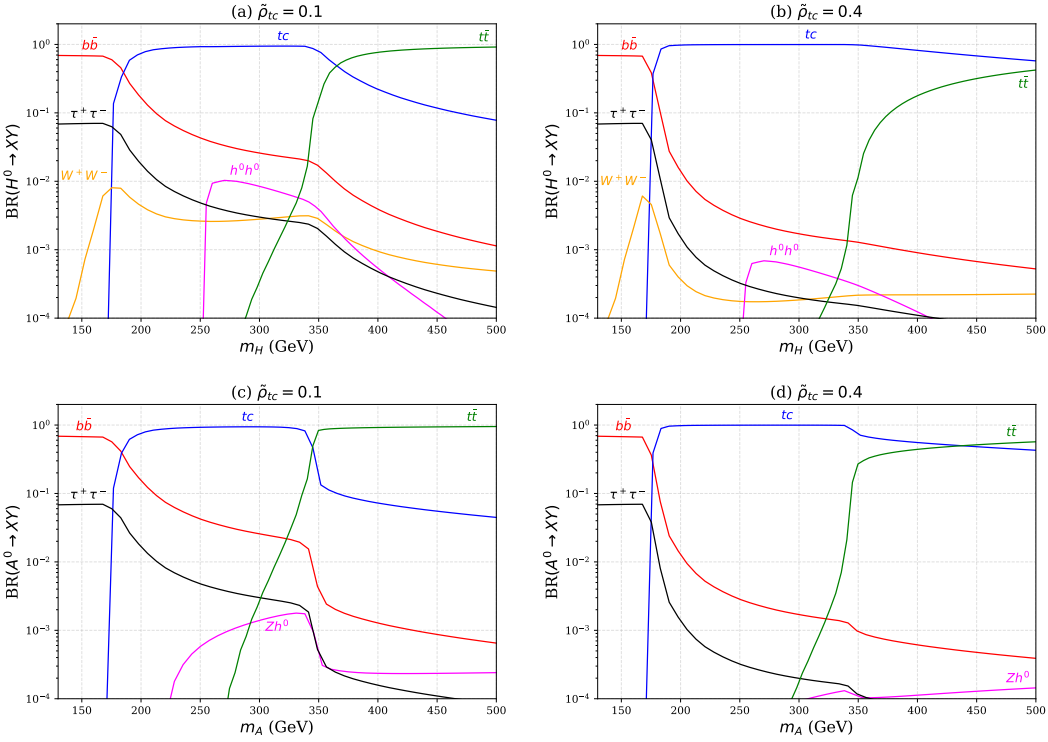


Figure 2.2: Branching ratios of $\phi^0 \to XY$ as functions of m_ϕ. The parameters are chosen as $c_{\beta-\alpha} = 0.01$ and $\rho_{tt} = 0.2 \times m_\phi/(150\ \text{GeV})$, with: (a) H^0, $\tilde{\rho}_{tc} = 0.1$; (b) H^0, $\tilde{\rho}_{tc} = 0.4$; (c) A^0, $\tilde{\rho}_{tc} = 0.1$; (d) A^0, $\tilde{\rho}_{tc} = 0.4$.

impossible for realistic final states with multiple outgoing particles. In our analysis, typical discovery channels involve seven or eight final-state particles, leading to integrals with more than 20 dimensions. To handle this complexity, we employ numerical Monte Carlo (MC) integration [56] techniques combined with matrix-element generators and detector simulations. This section provides an overview of the computational tools we applied in our analysis.

VEGAS

The core challenge in evaluating cross sections is dealing with the integration over the multidimensional phase space,

$$I = \int_{\Omega} f(x)\, dx\,, \tag{2.10}$$

where Ω denotes the N-dimensional integration domain. Monte Carlo (MC) integration estimates such integrals using random sampling [56]. By generating n random points x_i within Ω, the integral can be approximated as

$$E = \frac{1}{n} \sum_{i=1}^{n} f(x_i)\,, \tag{2.11}$$

where E converges to the true value I as $n \to \infty$, according to the law of large numbers. The variance of this estimator is

$$\sigma^2(f) = \frac{1}{n} \sum_{i=1}^{n} f(x_i)^2 - E^2\,, \tag{2.12}$$

and the corresponding statistical uncertainty scales as $\Delta I \propto n^{-1/2}$, independent of the dimensionality N. This property makes MC integration especially powerful for high-dimensional integrals where conventional numerical quadrature methods fail.

To further improve convergence, variance-reduction techniques are employed. In our $\phi^0 \to \tau^+\tau^-$ study, we use the VEGAS algorithm [57], developed by G. P. Lepage, which combines adaptive stratified sampling with importance sampling. VEGAS iteratively refines the sampling probability distribution based on previous evaluations of $f(x)$, concentrating more points in regions where the integrand contributes most to the integral. This adaptive approach substantially enhances

efficiency and reduces variance, enabling accurate cross-section estimation even for leptokurtic distributions.

In practice, VEGAS is implemented in FORTRAN and coupled to matrix-element (ME) generators. The algorithm maps each phase-space variable to random numbers uniformly distributed in $[0, 1]$, allowing event generation directly consistent with the differential cross section. Our implementation follows the iterative phase-space factorization technique,

$$d\Phi_N = (2\pi)^{-1} d\Phi_{N-1}\, d\Phi_{12}\, dM_{12}^2\,, \tag{2.13}$$

which successively reduces an N-body phase space into a series of two-body subspaces. This iterative reduction allows efficient sampling and integration for multi-particle final states.

To avoid divergences associated with soft or collinear emissions—common in QCD processes—we apply basic kinematic cuts:

- Transverse momentum cut: $p_T = \sqrt{p_x^2 + p_y^2}$,
- Pseudorapidity restriction: $\eta = -\ln(\tan\theta/2)$,
- Angular separation: $\Delta R_{ij} = \sqrt{(\Delta\eta_{ij})^2 + (\Delta\phi_{ij})^2}$.

These cuts remove infrared and collinear singularities, ensuring stable numerical convergence.

MadGraph 5, Pythia8, and Delphes

While VEGAS provides an efficient method for integrating phase-space weights, the physical content of $|\mathcal{M}|^2$—the squared scattering amplitude—depends on the underlying theory and process. For realistic collider studies involving many

Feynman diagrams, manual computation of $|\mathcal{M}|^2$ is impractical. We therefore use a suite of automated tools that handle matrix-element generation, parton showering, and detector simulation.

MadGraph 5. MadGraph5_aMC@NLO [58] (MG5) automatically generates all tree-level (and optionally next-to-leading-order) Feynman diagrams for a given process based on a chosen theoretical model file. It supports both tree-level and next-to-leading-order (NLO) computations in perturbative QCD, making it one of the most widely used tools in collider phenomenology. MG5 interprets model information from Universal FeynRules Output (UFO) files, which define the particle content, parameters, and interaction vertices derived from the underlying Lagrangian. This modular structure allows for straightforward extensions beyond the Standard Model (BSM), including two-Higgs-doublet models, supersymmetric models, or other effective field theories.

For each process, MG5 employs the HELAS (HELicity Amplitude Subroutines) library [59] to compute the corresponding matrix elements. These amplitudes are summed over spins, colors, and helicities of the incoming and outgoing particles to obtain $|\mathcal{M}|^2$. Once the matrix elements are computed, MG5 performs the phase-space integration to evaluate total and differential cross sections, employing the VEGAS adaptive Monte Carlo algorithm for efficient multidimensional integration and event generation. The resulting parton-level events are stored in standard Les Houches Event (LHE) format, which contains the full parton-level kinematics and event weights, ready for subsequent processing.

Pythia8. The events generated by MG5 are passed to Pythia8 [60], which simulates parton showering and hadronization. Since quarks and gluons cannot

exist freely due to confinement, Pythia models their transition into observable hadrons. The program also includes multiple parton interactions, underlying-event modeling, and initial- and final-state radiation effects, producing realistic hadronic final states observed in collider experiments.

To ensure a consistent description between matrix-element (ME) calculations from MG5 and the parton shower, appropriate matching or merging schemes are applied, such as the MLM or CKKW-L algorithms [61, 62]. These algorithms avoid double counting of emissions between the matrix-elements (ME) and parton showering (PS) stages while preserving the correct jet multiplicity and kinematic distributions. The combination of MadGraph and Pythia8 thus provides a complete simulation framework, producing fully hadronized final states that accurately represent the physical signatures expected in proton–proton collisions at the LHC.

Delphes. To emulate detector effects, we use Delphes [63], a fast simulation framework designed to approximate the performance of general-purpose collider detectors such as ATLAS and CMS. Delphes employs a parametrized approach that preserves the essential features of the detector response while ensuring computational efficiency. This makes it particularly suitable for phenomenological studies and large-scale Monte Carlo event samples.

Reading the output events from Pythia8, Delphes simulates the propagation of stable particles through simplified detector subsystems—including the tracking system, electromagnetic and hadronic calorimeters, and muon chambers. Each subsystem is defined by its geometrical acceptance, momentum or energy resolution, and particle identification efficiency, all specified in a configurable detector card. These parametrized smearing and efficiency effects emulate the finite precision and

intrinsic limitations of realistic experimental measurements, providing a fast yet physically accurate approximation of detector performance.

Reconstruction of physics objects is performed using algorithms consistent with those employed by the LHC collaborations. Charged-particle tracks are reconstructed in the inner tracker, while energy deposits in the calorimeters are clustered to form electromagnetic and hadronic energy clusters. Jets are reconstructed from final-state particles using the FastJet package [64], typically employing the anti-k_T algorithm [65] with a jet radius parameter $R = 0.4$ or 0.5. Electrons, muons, and photons are identified based on their detector signatures, and isolation criteria are applied to reduce contamination from nearby hadronic activity.

In summary, Delphes provides a critical bridge between theoretical event generation and experimental observation, allowing for fast and realistic assessments of detector effects in collider studies.

Event Yields and Luminosity. The total number of expected events is obtained as

$$N = \sigma \times \mathcal{L}\,, \tag{2.14}$$

where σ is the production cross section and $\mathcal{L}$ is the integrated luminosity. For two colliding Gaussian beams, the luminosity is expressed as [66]

$$\mathcal{L} = \frac{N_1 N_2 f N_b}{4\pi\sigma_x\sigma_y}\,, \tag{2.15}$$

with $N_{1,2}$ the number of particles per bunch, f the revolution frequency, N_b the number of bunches, and σ_x, σ_y the transverse bunch sizes.

Higher-Order Corrections. In our study, leading-order (LO) matrix elements provide the baseline cross-section estimates. To approximate next-to-leading-order (NLO) or next-to-next-to-leading-order (NNLO) effects, we apply K-factors defined as

$$K = \frac{\sigma_{\text{NLO (NNLO)}}}{\sigma_{\text{LO}}}\,. \tag{2.16}$$

The inclusion of these factors improves agreement with experimental measurements and accounts for missing higher-order QCD corrections.

2.2.2 Analysis Strategies

After generating simulated signal and background samples through the workflow described in the previous section, we employ two complementary strategies to enhance the signal-to-background discrimination: the traditional *cut-based optimization* and the modern *machine-learning approach* based on boosted decision trees (BDTs). Both methods aim to identify optimal event-selection criteria that maximize the statistical significance of the signal while efficiently rejecting backgrounds.

Cut-based Optimization

The cut-based analysis represents the most conventional and transparent approach to collider data selection. It relies on applying a series of sequential one-dimensional selection cuts on key kinematic observables to isolate the desired signal events from the dominant backgrounds. Typical observables used in our analysis include:

- Transverse momentum of jets and leptons (p_T),
- Pseudorapidity (η) and angle separation ($\cos\theta_{ij}$),

- Missing transverse energy (E_T^{miss}),
- Angular separation between jets and leptons (ΔR),
- Invariant masses of reconstructed particle combinations.

These variables are chosen to exploit the characteristic kinematic features of the signal process while suppressing Standard Model backgrounds such as $t\bar{t}$, W/Z+jets, or QCD multijet production.

The optimization is performed by scanning over possible cut thresholds and maximizing the expected statistical significance, denoted by N_{SS}, commonly defined as

$$N_{SS} = \frac{S}{\sqrt{S+B}}\,, \tag{2.17}$$

where S and B denote the expected number of signal and background events after selection, respectively. For high-luminosity projections, where both signal and background event counts follow Poisson statistics, a more accurate expression for the statistical significance is adopted [67]:

$$N_{SS} = \sqrt{2\left[(S+B)\ln\left(1+\frac{S}{B}\right) - S\right]}\,, \tag{2.18}$$

which will reduce to $S/\sqrt{B}$ in the limit $B \gg 1$ with Gaussian distributions. $N_{SS} = 5$ corresponds to a 5σ significance – the conventional discovery threshold.

Cut-based analysis is intuitive and physically transparent, making it straightforward to implement and interpret. However, as the dimensionality of the input feature space grows or when correlations among observables become significant, multivariate techniques—such as boosted decision trees (BDTs)—provide a more powerful and systematic framework for event classification.

Machine Learning with BDT

To improve classification performance beyond what can be achieved with sequential cuts, we employ a supervised machine-learning algorithm based on Boosted Decision Trees (BDTs). BDTs are particularly well suited to collider physics, as they combine interpretability with the ability to capture nonlinear correlations among multiple observables [68].

Concept. A decision tree partitions the multidimensional feature space into regions that are predominantly signal- or background-like by applying a sequence of binary splits on input variables. Boosting—typically implemented through the *gradient boosting* or *AdaBoost* algorithm—constructs an ensemble of weakly correlated trees, each trained to correct the misclassifications of the previous ones. The final model prediction is a weighted sum of the outputs of individual trees, effectively reducing variance and bias simultaneously.

Training and Input Variables. The training dataset consists of Monte Carlo–generated signal and background events, labeled respectively as 1 and 0. Each event is characterized by a set of discriminating variables such as:

- p_T, η, and ϕ of jets and leptons,
- Invariant masses of reconstructed intermediate states (e.g., m_{jj}, $m_{b\ell}$),
- Event-shape observables such as $H_T = \sum_i p_{T,i}$,
- Missing transverse energy (E_T^{miss}),
- Angular separations ΔR_{ij} between jets and leptons.

These features are preprocessed (e.g., normalized or standardized) to ensure stable and efficient training.

Implementation. The XGBoost framework [69] is implemented with an interface compatible with scikit-learn [70], allowing for seamless integration with standard machine-learning workflows in Python. Training a BDT classifier thus requires only importing the model and specifying the relevant hyperparameters. The key parameters—such as the number of trees ($n_{\text{estimators}}$), maximum tree depth (max_depth), learning rate (η), and minimum child weight—are systematically optimized using grid search and k-fold cross-validation to prevent overfitting and to ensure robust generalization.

The dataset is randomly divided into statistically independent training and testing subsets, typically with a 75:25 ratio. Class weights are assigned to compensate for the imbalance in event yields between signal and background samples, ensuring that both contribute effectively to the learning process.

Performance Evaluation. The performance of the BDT is quantified using the receiver operating characteristic (ROC) curve, which plots the true positive rate (signal efficiency) versus the false positive rate (background rejection). The area under the ROC curve (AUC) serves as a scalar metric for classifier performance, with AUC closing to 1 indicating nearly perfect separation. Feature-importance scores, computed from the frequency or gain associated with variable splits, help identify the most discriminating observables.

Application. After training, the BDT assigns a discriminant score to each event. By applying an optimized threshold on this score, one can select events with the highest signal purity. The corresponding signal significance is then evaluated

using Eq. (**2.18**). The BDT approach efficiently exploits complex correlations between variables, achieving superior background rejection while retaining high signal efficiency.

Comparison with Cut-based Approach. Compared with traditional cut-based methods, the BDT provides a more robust and systematic treatment of correlated observables, especially in high-dimensional feature spaces. However, it is important to cross-check that the BDT-selected regions are consistent with physical expectations and not dominated by statistical fluctuations or model-specific artifacts. In this study, both cut-based and BDT methods are employed to ensure reliability and cross-validation of the final results.

2.3 Summary of Chapter 2

Chapter 2 presents the motivations, analytical tools and analysis strategies underlying the collider studies performed in this dissertation. The chapter begins by identifying the Higgs flavor-changing processes of interest and explaining why they offer compelling opportunities to probe the extended Higgs sector of the G2HDM. Two classes of processes are emphasized: (i) the charged Higgs flavor-changing channel $pp \to bH^+ \to bc\bar{b}$, which is directly sensitive to the coupling $\lambda_{H^+cb} \propto \rho_{tc} V_{tb}$, and (ii) the neutral FCNH channels, including $\phi^0 \to \tau^+\tau^-$ and $t\phi^0 \to t(tc)$, which provide complementary access to the Yukawa structure associated with $\tilde{\rho}_{tc}$ and related parameters.

The second part of the chapter describes the analytical tools and strategies employed throughout the dissertation. Event generation is carried out using MadGraph5_aMC@NLO, while parton showering and hadronization are per-

formed with PYTHIA 8, and detector responses are modeled using DELPHES. Data handling and event-level analysis utilize ROOT-based frameworks, including EXROOTANALYSIS. A consistent analysis strategy is adopted across all channels, involving realistic acceptance cuts, tagging efficiencies, reconstruction of intermediate resonances, optimization of discriminating observables, and evaluation of signal significance at different collider energies and luminosities. This unified approach ensures that the results presented in the subsequent chapters are directly comparable and reflect realistic LHC detector performance. In addition, a concise introduction to the BDT machine-learning technique is included.

Overall, Chapter 2 establishes the theoretical motivations for the chosen Higgs signal channels and provides a systematic framework for the collider analyses presented in Chapters 3 and 4.

Chapter 3

Searching for Charged Higgs Boson at the LHC

In this chapter, we present the detailed study for the process $pp \to bH^+$, followed by the decay $H^+ \to c\bar{b}$. Before proceeding to collider analysis, we discuss in Section 3.1 the current experimental constraints on the relevant parameters, in particular ρ_{tc}. In Section 3.2, we discuss the characteristics of the signal and dominant background processes, along with the event selection strategies employed to improve the statistical significance. The final cross sections after all selection cuts are calculated at the collider energy $\sqrt{s} = 13$, 13.6, and 14 TeV and are presented in Section 3.3, together with the corresponding discovery contours for $\sqrt{s} = 13$ and 14 TeV. The results of this study are part of a completed project currently being prepared for publication by the end of this year.

3.1 Constraints on Relevant Parameters

Both of our FCNH signal cross section depends directly on $\tilde{\rho}_{tc}$, especially for $pp \to t\phi^0 \to t(tc)$ channel. For $\phi^0 \to \tau^+\tau^-$ channel, the decay modes of τ-leptons also plays an important role.

Recent searches for the flavor-changing neutral decay $t \to ch^0$ by the ATLAS [71] and CMS [72] collaborations have placed stringent constraints on the corresponding branching ratio, yielding $\mathcal{B}(t \to ch) \leq 3.4 \times 10^{-4}$ [71] and $\mathcal{B}(t \to ch) \leq 3.7 \times 10^{-4}$ [72], respectively.

These bounds imply an upper limit on the effective FCNH Yukawa coupling,

$$\lambda_{tch} \leq 0.035, \tag{3.1}$$

defined in the effective Lagrangian,

$$\mathcal{L} = -\frac{\lambda_{tch}}{\sqrt{2}}\, t\bar{c}h^0 + \text{H.c.}, \tag{3.2}$$

where the relation between λ_{tch} and the branching fraction $\mathcal{B}(t \to ch)$ is given by [73]

$$\lambda_{tch} \simeq 1.92 \times \sqrt{\mathcal{B}(t \to ch)}. \tag{3.3}$$

In our framework, this coupling is related to the Yukawa parameters through $|\lambda_{tch}| = \tilde{\rho}_{tc}\, c_{\beta-\alpha}$, with $\tilde{\rho}_{tc} \approx \sqrt{(|\rho_{tc}|^2 + |\rho_{ct}|^2)/2}$, as defined in Section 2.1.1.

Furthermore, from Section 2.1.1, the FCNH couplings for the heavier neutral Higgs bosons are given by

$$|\lambda_{tcH}| = \tilde{\rho}_{tc}\, s_{\beta-\alpha}, \tag{3.4}$$

$$|\lambda_{tcA}| = \tilde{\rho}_{tc}. \tag{3.5}$$

In the alignment limit where $s_{\beta-\alpha} \simeq 1$, $|\lambda_{tcH}|$ is enhanced relative to $|\lambda_{tch}|$, potentially leading to striking signatures such as same-sign top-quark and triple-top production via $cg \to tH \to tt\bar{c}$ or $tt\bar{t}$ [74, 75].

Direct searches for heavy Higgs bosons with flavor-changing couplings by ATLAS [76] and CMS [77] have placed additional constraints on $\tilde{\rho}_{tc}$. In the CMS analysis [77], when no interference between H and A is considered, no exclusion limits are obtained for m_H or m_A with a coupling value of $\tilde{\rho}_{tc} = 0.4$. When interference effects are included, still assuming $\tilde{\rho}_{tc} = 0.4$, the exclusion limits extend to $m_H = 290$ GeV and $m_A = 340$ GeV. For a larger coupling of $\tilde{\rho}_{tc} = 1.0$, the limits are significantly stronger, reaching $m_H = 760$ GeV and $m_A = 810$ GeV at the 95% confidence level (CL) [77].

The ATLAS search [76] excludes an H boson with masses in the range 200 GeV $< m_H <$ 620 GeV at 95% CL, for benchmark coupling values $\rho_{tt} = 0.4$, $\tilde{\rho}_{tc} = 0.2$, and $\tilde{\rho}_{tu} = 0.2$. For smaller or vanishing $\tilde{\rho}_{tu}$, the exclusion power weakens accordingly [76].

To remain consistent with flavor constraints, we adopt $\rho_{tt} = 0.2\times(m_{H^+}/150\,\text{GeV})$, as discussed in Section 2.1.1. In addition, to satisfy the same flavor constraints, the remaining Yukawa couplings, such as ρ_{bb} and $\rho_{\tau\tau}$, are taken to be identical to their corresponding Standard Model values, κ_{bb} and $\kappa_{\tau\tau}$, respectively.

Noting that flavor constraints on ρ_{tc} remain relatively weak [78]. The coupling ρ_{ct} is more tightly constrained, with $\rho_{ct} < 0.1$ [78]. In particular, B_s–$\bar{B}_s$ mixing imposes an upper bound of $|\rho_{tc}| \lesssim 1.7$ for $m_{H^+} = 500$ GeV [78, 79]. In the following analysis, we set $\rho_{ct} = 0.05$, while varying $\rho_{tc} \leq 0.5$ and $m_{H^+} \in [200, 500]$ GeV.

3.2 Collider Study for $H^+ \to c\bar{b}$

In this section, we propose the process $cg \to bH^+$ (see Fig. **3.1**), followed by the decay $H^+ \to c\bar{b}$, as a promising discovery channel for a BSM charged Higgs boson at the LHC in the near future. Using the parameter space discussed above, we investigate the discovery potential of the signal in the presence of the relevant Standard Model backgrounds. By applying realistic selection criteria, including b-tagging and c-tagging efficiencies, we evaluate the statistical significance of the signal at the LHC for center-of-mass energies of $\sqrt{s} = 13$, 13.6, and 14 TeV.

3.2.1 Higgs signal

We study charged Higgs boson production at the LHC via the process $cg \to bH^+$, with the subsequent decay $H^+ \to c\bar{b}$, leading to a $bc\bar{b}$ final state. The complete

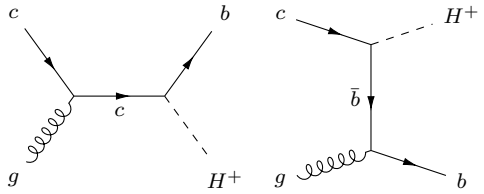


Figure 3.1: Leading-order Feynman diagrams for $cg \to bH^+$.

Monte Carlo simulation is carried out using MadGraph5_aMC@NLO [58], Pythia-8 [60], and Delphes [63]. In addition, we applied matching and merging with xqcut=30 GeV. The signal cross section is evaluated using the CT14LLO parton distribution function (PDF) [80], with the renormalization and factorization scales set to $\mu_{R,F} = m_{H^+}$. Applying the above scale choices and PDF, our current estimates suggest a K-Factor of ≈ 1.95, and is approximately the same for all three energies ($\sqrt{s} = 13, 13.6, \text{and } 14$ TeV). The K-factors are calculated using MadGraph5_aMC@NLO.

3.2.2 The Physics Background

The dominant physics background to the signal arise from $b\bar{b}j$ and $c\bar{c}j$. Using the same simulation framework and PDF as for the signal, we compute the cross sections with both the renormalization and factorization scales set to $\mu_{R,F} = \sqrt{\hat{s}}$. In addition, we scale our backgrounds to next-to-leading order using K-factor of 1.26 for $b\bar{b}j$ and $c\bar{c}j$ [81].

3.2.3 Mass Reconstruction and Realistic acceptance

Using the default ATLAS Delphes card, we incorporate charm-tagging efficiencies based on recent CMS results [82], with $\varepsilon_c = 0.22$, $\varepsilon_b = 0.01$, and $\varepsilon_j = 0.001$. As for b-jet, the b-tagging efficiency is approximately 0.7, the probability that a

c-jet is mistagged as a b-jet is approximately 0.14, while the probability that a light jet (u, d, s, g) is mistagged as a b-jet is 0.01. For the event analysis, each event is required to contain at least three jets, including exactly one identified c-jet and two b-tagged jets.

We adopt the following basic requirements:

(i) exactly one c-jet with $p_T^c \geq 25$ GeV, $|\eta_c| < 2.5$;

(ii) exactly two b-jets with $p_T^b \geq 25$ GeV, $|\eta_b| < 2.5$;

(iii) angular separation between every two pairs of jets satisfy $\Delta R_{jj} \geq 0.4$.

To correctly reconstruct the events, the c-jet and one of the b-jets, denoted b_1, must originate from the decay of the charged Higgs boson (H^+) and are expected to be energetic. In addition to the basic selection cuts, we further require $p_T^{b_1} > 50$ GeV, $p_T^c > 70$ GeV and an angular separation $\Delta R_{cb_1} > 2.0$. The invariant mass distribution of the c-jet and b_1-jet pair, M_{cb_1}, are expected to exhibit a peak around the mass of the charged Higgs, m_{H^+}. Fig. **3.2** shows the $d\sigma/M_{cb_1}$ distributions for the signal with $m_{H^+} = 200$ and 400 GeV, together with the dominant physics backgrounds. A pronounced peak appears near m_{H^+} for $m_{H^+} = 200$ GeV case, while for 400 GeV the peak is less distinct, but still provides discrimination against backgrounds. Using the ATLAS mass resolution [83], the reconstructed c-jet and b_1-jet masses are required to lie a mass window of $\Delta M_{cb_1} = 0.20 \times m_{H^+}$. These selection requirements are optimized to suppress background processes while enhancing the statistical significance of the signal. The complete set of final selection criteria is summarized in Table **4.2**.

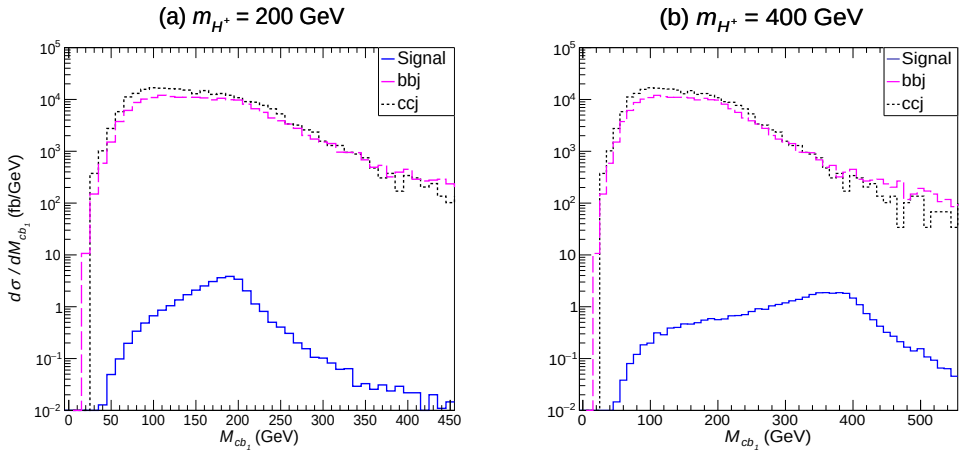


Figure 3.2: Invariant mass distributions $d\sigma/dM_{cb_1}$ for the signal and dominant backgrounds $b\bar{b}j$ (magenta, dashed) and $c\bar{c}j$ (black, dotted) at $\sqrt{s} = 14$ TeV, shown for $\rho_{tc} = 0.4$, (a) $m_{H^+} = 200$ GeV (blue, solid) and (b) $m_{H^+} = 400$ GeV (blue, solid).

selection rule
1 tagged c-jet, 2 tagged b-jets
$p_T^j > 25$ GeV, $\lvert\eta_j\rvert < 2.5$, $\Delta R_{jj} > 0.4$
$p_T^{b_1} > 50$ GeV
$p_T^c > 70$ GeV
$\Delta R_{cb_1} > 2.0$
$\lvert M_{cb_1} - m_{H^+}\rvert \leq 0.20 \times m_{H^+}$

Table 3.1: Final selection criteria for signal and backgrounds events.

3.3 Discovery Potential

After applying all selection criteria at the collider energy $\sqrt{s} = 13$, 13.6, and 14 TeV, the signal cross sections for various benchmark points (BPs), along with the corresponding background cross sections, are summarized in Table **3.2**. The estimated statistical significances, calculated with Eq. (**2.18**), are also presented in Table **3.2**.

Fig. **3.3** presents the cross section as a function of ρ_{tc} for different values of m_{H^+} at a collider energy of $\sqrt{s} = 14$ TeV. Fig. **3.4** presents the 5σ discovery contour

$\sqrt{s}$ (TeV)	BP_1 (fb)	$b\bar{b}j$ (fb)	$c\bar{c}j$ (fb)	Total (fb)	N_{SS}
13	353.4	8.052×10^4	7343	8.786×10^4	26.6
13.6	394.0	8.407×10^4	7851	9.192×10^4	28.9
14	406.3	8.988×10^4	8741	9.862×10^4	28.9
$\sqrt{s}$ (TeV)	BP_2 (fb)	$b\bar{b}j$ (fb)	$c\bar{c}j$ (fb)	Total (fb)	N_{SS}
13	103.2	8.332×10^4	7692	9.102×10^4	7.65
13.6	109.4	9.009×10^4	8223	9.831×10^4	7.80
14	116.1	9.723×10^4	9178	1.064×10^5	7.96
$\sqrt{s}$ (TeV)	BP_3 (fb)	$b\bar{b}j$ (fb)	$c\bar{c}j$ (fb)	Total (fb)	N_{SS}
13	25.61	6.323×10^4	5634	6.887×10^4	2.18
13.6	27.64	6.927×10^4	5762	7.503×10^4	2.26
14	29.37	7.129×10^4	7025	7.832×10^4	2.35

Table 3.2: Benchmark points used in this table, which correspond to $\rho_{ct} = 0.05$, $\rho_{tc} = 0.4$ and $m_{H^+} = 200$ GeV (BP_1), $m_{H^+} = 300$ GeV (BP_2), and $m_{H^+} = 400$ GeV (BP_3). Statistical significance is presented with integrated luminosity $L = 500\,\text{fb}^{-1}$. K-factors are included in the cross section.

at the LHC for (a) $\sqrt{s} = 13$ TeV and (b) $\sqrt{s} = 14$ TeV in the (m_{H^+}, ρ_{tc}) plane, assuming integrated luminosities of $L = 300$ and 3000 fb^{-1}. The results clearly demonstrate that the high-energy LHC at $\sqrt{s} = 14$ TeV with high luminosity, $L = 3000$ fb^{-1}, substantially enhances the discovery potential.

3.4 Summary of Chapter 3

Chapter 3 presents a detailed collider study of the charged Higgs boson H^+ within the framework of the G2HDM, focusing on the flavor-changing process $pp \to bH^+ \to b\,c\bar{b} + X$. The chapter begins by reviewing the current experimental limits on the relevant Yukawa couplings, especially ρ_{tc}, ρ_{ct}, and ρ_{tt}, based on recent ATLAS and CMS searches for flavor-changing neutral Higgs interactions. These constraints guide the parameter space considered in the simulation analysis.

A comprehensive collider study of the channel $H^+ \to c\bar{b}$ is carried out using a full Monte Carlo framework incorporating MadGraph5_aMC@NLO, Pythia8,

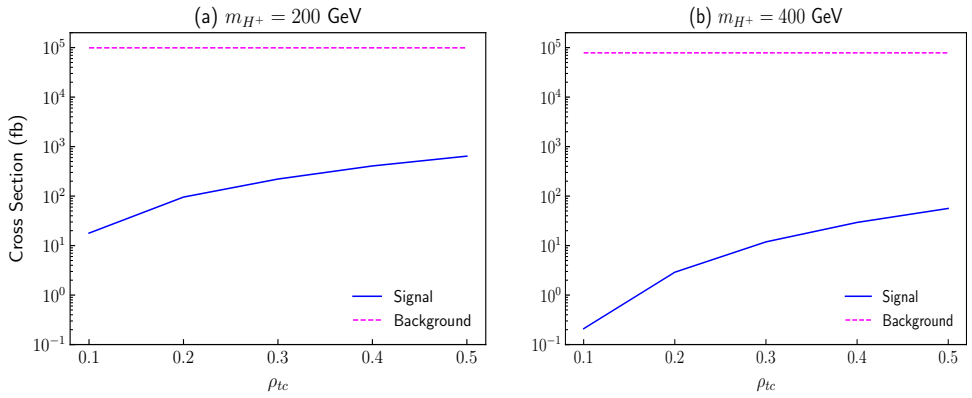


Figure 3.3: The cross section as a function of ρ_{tc} for signal and background at $\sqrt{s} = 14$ TeV after selection cuts, shown for (a) $m_{H^+} = 200$ GeV and (b) $m_{H^+} = 400$ GeV.

and DELPHES. The signal and dominant Standard Model backgrounds—primarily $b\bar{b}j$ and $c\bar{c}j$—are simulated at $\sqrt{s} = 13$, 13.6, and 14 TeV with appropriate K-factors. Dedicated selection cuts, including c-tagging and b-tagging efficiencies, are applied to suppress backgrounds.

The chapter further introduces mass reconstruction strategies designed to reconstruct the charged Higgs mass from the invariant mass M_{cb_1}, taking into account jet combinatorics and realistic detector resolution. With these selection criteria, the final cross sections and statistical significances are evaluated for several benchmark points. The results demonstrate that the charged Higgs boson can be probed effectively for a broad region of parameter space, particularly for $\rho_{tc} \gtrsim 0.1$ and $m_{H^+} \lesssim 450$ GeV at high luminosity. Chapter 3 thus establishes the process $pp \to bH^+ \to b\,c\bar{b} + X$ as a promising channel for discovering flavor-changing charged Higgs boson interactions at the LHC.

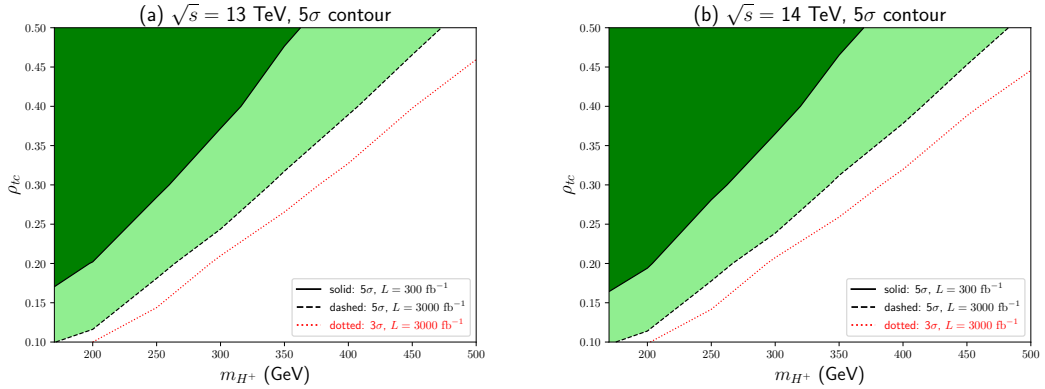


Figure 3.4: The 5σ discovery contours at the LHC in the (m_{H^+}, ρ_{tc}) plane for (a) $\sqrt{s} = 13$ TeV and (b) $\sqrt{s} = 14$ TeV with $L = 300\,\text{fb}^{-1}$ (dark green solid) and $L = 3000\,\text{fb}^{-1}$ (light green dashed). In addition, 3σ discovery contour with $L = 3000\,\text{fb}^{-1}$ (red dotted) are shown for both 13 and 14 TeV.

Chapter 4

Probing Heavy Neutral Higgs Bosons via Interactions with Top quark

This chapter presents a collider study of the top quark (t) interactions with neutral Higgs bosons, focusing on two promising flavor-changing neutral Higgs (FCNH) channels. In Section 4.1, we present the results for the process $pp \to t\bar{t} \to (bjj)(\bar{c}\phi^0) + X$, followed by $\phi^0 \to \tau_{lep}\tau_{had}$, where $\tau_{\rm lep}$ denotes the leptonic decay $\tau \to \ell\,\nu_\ell\,\nu_\tau$ with $\ell = e,\ \mu$, and $\tau_{\rm had}$ denotes the hadronic decay $\tau \to j_\tau\,\nu_\tau$, with $j_\tau = \pi^\pm$, ρ, and a_1, representing the hadronic τ decay products. A parton-level study is performed using VEGAS, incorporating simplified detector effects, along with an event-level analysis utilizing MG5, Pythia8 and Delphes, as introduced in Section 2.2.1. The resulting cross sections and corresponding discovery contours are presented in Section 4.1.3. This study constitutes a completed project that is currently in preparation for publication by the end of this year.

In Section 4.2, we investigate another channel, $pp \to t\phi^0 \to t(tc)$, where the signal is categorized according to the decay mode of the top quarks: (i) the all-top channel, $ttc \to bjjc\,b\ell\nu$, and (ii) the same-sign top (SS-top) channel, $ttc \to bbc\,\ell\ell\nu\nu$, with $\ell = e, \mu$ and ν denoting neutrinos. A similar event-level analysis is conducted with additional optimization strategies. The corresponding cross sections and discovery contours are presented in Section 4.2.3. This work is ongoing, and the results are expected to be published by the end of this year.

Motivated by the disscussion in Section 3.1, we define our parameter space for the $\phi^0 \to tc$ study as $0.1 \leq \tilde{\rho}_{tc} \leq 0.5$ and 200 GeV $\leq m_\phi \leq$ 500 GeV. For lighter Higgs masses, $m_\phi <$ 200 GeV, no direct experimental limits on $\tilde{\rho}_{tc}$ are

currently available; thus, we conservatively adopt the same range, $0.1 \leq \tilde{\rho}_{tc} \leq 0.8$, for 130 GeV $\leq m_\phi \leq$ 200 GeV, before the $\phi^0 \to \tau^+\tau^-$ decay mode becomes suppressed.

4.1 Detecting Flavor Changing Neutral Higgs Bosons in Top Decays with τ pairs

4.1.1 The Higgs Signal and Standard Model background

We present the discovery study for the process $pp \to t\bar{t} \to (bjj)(\bar{c}\phi^0) \to (bjj)(\bar{c}\tau^+\tau^-) + X$ where one of the τ-leptons decays leptonically into an electron or muon accompanied by neutrinos, and the other τ decays hadronically into a τ-jet and neutrinos. Consequently, the final state of our FCNH signal can be expressed as $pp \to t\bar{t} \to (bjj)(\bar{c}\ell^{\mp}j_\tau) + \not{E}_T + X$, where $\ell = e$, μ and X denotes any additional particles produced in the pp collisions. The leading-order Feynman diagrams for this process are shown in Fig. **4.1**, where t^* represents a virtual top quark in the case of $m_\phi > m_t$.

In the final state, we thus expect one lepton and one τ-jet originating from the Higgs boson decay, together with missing transverse energy ($\not{E}_T$) arising from the undetected neutrinos. The other top quark is required to decay hadronically into a b-jet and two light jets, resulting in a final state consisting of five jets (including one b-jet) and one isolated lepton.

According to the final state, two dominant backgrounds to the signal are from $t\bar{t}j$ (with $j = q$ or g), which is the most significant, with one top quark decaying leptonically ($t \to b\ell\nu$) the other decaying hadronically ($t \to bjj$) and the second dominant background (about one third of the most dominant background) is

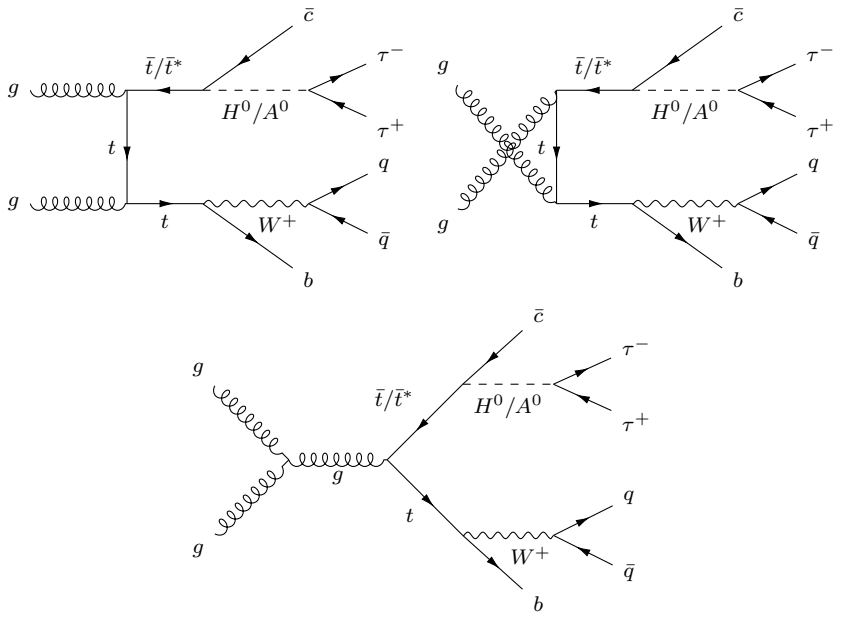


Figure 4.1: Leading-order Feynman diagrams for the $\phi^0 \to \tau^+\tau^-$ signal.

$t\bar{t}jj(+\tau)$, $j = q$ or g with one top quark decaying leptonically ($t \to b\ell\nu$) the other decaying into τ_{had} ($t \to b\tau_{had}\nu_\tau$). These two backgrounds contribute more than 95% of the total background. $pp \to Zb\bar{b}jj + X$ ($Zb\bar{b}jj$) with the subsequent decay of $Z \to \tau_{lep}\tau_{had}$ is negligible after all acceptance requirements are imposed.

In our study, the matrix elements for $gg, q\bar{q} \to t\bar{t} \to bjjc\phi^0 \to bjjc\tau^+\tau^-$ are generated at leading order (LO) using MadGraph5 [58], as introduced in Section 2.2.1. In addition, we apply the collinear approximation for τ decays [84, 85]. Since the Higgs boson is much heavier than the τ lepton ($m_\phi \gg m_\tau$), the τ leptons produced in $\phi^0 \to \tau^+\tau^-$ are highly boosted. To a good approximation, the visible decay products (j_τ and ℓ) and the corresponding neutrinos can be assumed to travel in the same direction as their parent τ leptons.

Denoting the leptonic and hadronic τ decays as $\tau_{\text{lep}} \equiv \tau_1$ and $\tau_{\text{had}} \equiv \tau_2$,

respectively, the momenta of the two τ leptons can be expressed as

$$\vec{P}_{\tau_1} = \frac{\vec{P}_\ell}{x_1} \ , \quad \vec{P}_{\tau_2} = \frac{\vec{P}_{j_\tau}}{x_2} \ , \tag{4.1}$$

where $x_{1,2}$ represent the fractions of the τ-lepton momenta carried by the charged lepton and τ-jet, respectively, with $0 \leq x_i \leq 1$. The remaining fractions $(1 - x_i)$ correspond to the momenta of the undetected neutrinos. Hence, the missing transverse energy components can be estimated as

$$\not{E}_x = (1 - x_1)P_{\tau_1 x} + (1 - x_2)P_{\tau_2 x} \tag{4.2}$$

$$\not{E}_y = (1 - x_1)P_{\tau_1 y} + (1 - x_2)P_{\tau_2 y} \, , \tag{4.3}$$

where $\not{E}_x$ and $\not{E}_y$ are the x- and y-components of the missing transverse energy ($\not{E}_T$). From Eqs. (**4.1**)–(**4.3**), the momentum fractions can be solved as

$$x_1 = \frac{P_{j_\tau x}P_{\ell y} - P_{\ell x}P_{j_\tau y}}{P_{j_\tau x}P_{\ell y} - P_{\ell x}P_{j_\tau y} + \not{E}_y P_{j_\tau x} - \not{E}_x P_{\ell y}}, \tag{4.4}$$

$$x_2 = \frac{P_{j_\tau x}P_{\ell y} - P_{\ell x}P_{j_\tau y}}{P_{j_\tau x}P_{\ell y} - P_{\ell x}P_{j_\tau y} - \not{E}_y P_{\ell x} + \not{E}_x P_{j_\tau y}}. \tag{4.5}$$

These relations allow us to reconstruct the Higgs boson mass from the invariant mass of the τ-lepton pair ($M_{\tau\tau}$).

The parton-level analysis is performed using the VEGAS [57], with τ decay branching fractions taken from Ref. [1], as summarized in Table **4.1**. The cross section is evaluated using the CT14LO parton distribution functions (PDFs) [80]. For simplicity, both the factorization and renormalization scales are set to the invariant mass of the top-quark pair, $\mu_F = \mu_R = \sqrt{\hat{s}}$. With these scale choices and PDFs, the corresponding K-factors are computed using TOP++ [86]. For all

three LHC center-of-mass energies, $\sqrt{s} = 13$, 13.6, and 14 TeV, the $t\bar{t}$ production K-factors are found to be approximately constant, around 1.8.

Decay mode	Branching Fraction
$\tau^- \to \mu^- \bar{\nu_\mu} \nu_\tau$	17.39 %
$\tau^- \to e^- \bar{\nu_e} \nu_\tau$	17.82%
$\tau^- \to \pi^- \nu_\tau$	10.82%
$\tau^- \to \pi^- \pi^0 (\rho^-) \nu_\tau$	25.49%
$\tau^- \to \pi^- \pi^0 \pi^0 (a_1) \nu_\tau$	9.26%
$\tau^- \to \pi^- \pi^+ \pi^- (a_1\, 3\text{-prong}) \nu_\tau$	8.99%

Table 4.1: Branching fractions for different τ-lepton decays modes.

In the event-level analysis, the parton-level signal samples are generated using MadGraph5 [58] with the 2HDM-UFO model [87]. The generated events are then passed to Pythia8 [60] to simulate parton showering, hadronization, and τ decays. The latter are handled by Tauola [88, 89], a dedicated Monte Carlo package embedded in Pythia8 and widely used for accurate modeling of τ-lepton decays in collider simulations. Subsequently, detector effects are incorporated using Delphes [63], which provides a fast and realistic parametrization of the ATLAS and CMS detector responses.

To obtain realistic estimates of production rates at the LHC, we evaluate the cross sections for both the FCNH signal and relevant physics backgrounds in pp collisions, incorporating appropriate tagging and mistagging efficiencies. The ATLAS b-tagging performance [90] is adopted in our analysis, with a b-tagging efficiency of $\varepsilon_b = 0.7$. The probability for a c-jet to be mistagged as a b-jet is $\varepsilon_c \simeq 0.14$, while that for a light-flavor jet (u, d, s, g) is $\varepsilon_j \simeq 0.01$. For τ-jets (j_τ), we apply ATLAS tagging efficiencies of $\varepsilon_\tau = 0.75$ (0.60) and mistag

rates $\varepsilon_\tau(j) = 0.03$ (0.002) for 1-prong (3-prong) τ decays, respectively, following Refs. [91, 92]. For this study, c-tagging is not applied, making the analysis equally applicable to the decay mode $t \to \phi^0 u$.

4.1.2 Mass Reconstruction and Realistic Acceptance Cuts

As discussed in the previous section, each event is required to contain at least five jets, including exactly one identified b-jet, one identified τ-jet, and one isolated lepton (e or μ). The following basic selection criteria are applied, following the strategies adopted in the ATLAS and CMS analysis of $h^0 \to \tau^+\tau^-$ [93]:

(i) At least five jets, including one b-jet and one τ-jet, with $p_T \geq 25$ GeV and $|\eta| \leq 2.5$,

(ii) One lepton with $p_T \geq 20$ GeV and $|\eta| \leq 2.5$,

(iii) The angular separation between any pair of reconstructed objects satisfies $\Delta R > 0.4$,

(iv) Missing transverse energy $\not{E}_T = \not{E}_T \geq 30$ GeV.

Since the two leading light jets (j_1, j_2) originate from the hadronic W-boson decay, their invariant mass distribution $M_{j_1 j_2}$ should peaks near the W-boson mass, $m_W \simeq 80.4$ GeV. Similarly, the invariant mass of the system comprising the b-jet and the two light jets, $M_{bj_1j_2}$, peaks near the top-quark mass, $m_t \simeq 172.6$ GeV. To correctly identify the jets from the W- and top-quark decays, we select the jet combination that minimizes both $|M_{jj} - m_W|$ and $|M_{bjj} - m_t|$. The invariant mass distributions of $M_{j_1j_2}$ and $M_{bj_1j_2}$ at both parton and event levels are shown in Figs. **4.2** and **4.3**, respectively. Following the ATLAS mass resolution [94],

we further require the reconstructed W- and top-quark masses to fall within the windows $\Delta M_{j_1 j_2} = 0.20\, m_W$ and $\Delta M_{b j_1 j_2} = 0.25\, m_t$.

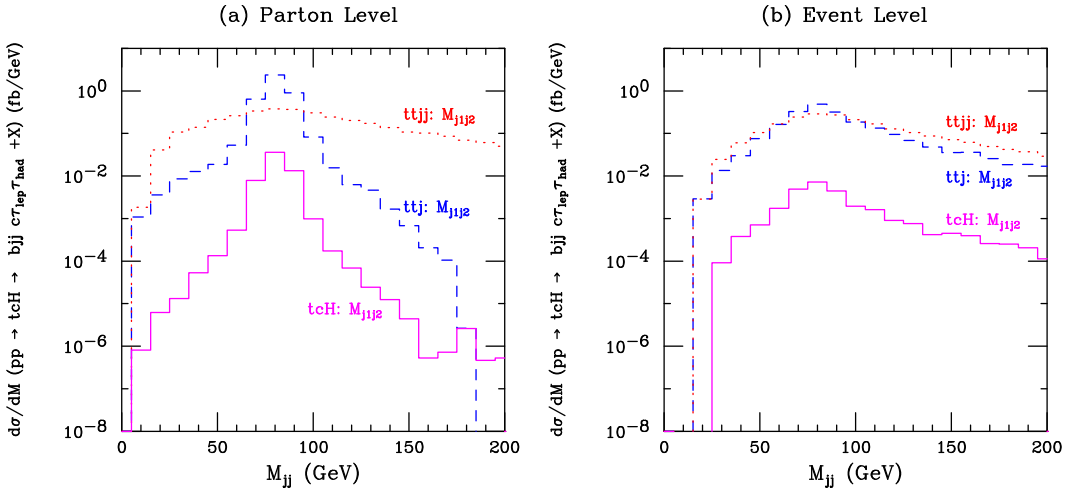


Figure 4.2: Invariant mass distribution $d\sigma/dM_{jj}$ for the Higgs signal (magenta, solid) and for the dominant background from ttj (blue, dashed) and $ttjj$ (red, dot) at the LHC with $\sqrt{s} = 13$ TeV. Results are shown for (a) parton level, and (b) event level.

For the top quark decay chain $t \to c\phi^0 \to c\tau^+\tau^- \to c\,\ell^\pm j_\tau + \not{E}_T$, when the Higgs boson is lighter than the top quark ($m_\phi < m_t$), the c-jet is identified by minimizing $|M_{c\tau\tau} - m_t|$, where the τ leptons are reconstructed using the collinear approximation. We consider two kinematic scenarios:

(a) For $m_\phi \leq 150$ GeV, the c-jet is selected by minimizing $|M_{c\tau\tau} - m_t|$. In this regime, both the invariant mass of the τ-lepton pair, $M_{\tau^+\tau^-}$, from the Higgs decay and the invariant mass $M_{c\tau^+\tau^-}$ from the top-quark decay exhibit sharp peaks near m_ϕ and m_t, respectively.

(b) For $m_\phi > 150$ GeV, we select the light jet with the highest transverse momentum (p_T) among the remaining light jets and reconstruct only the invariant mass $M_{\tau^+\tau^-}$.

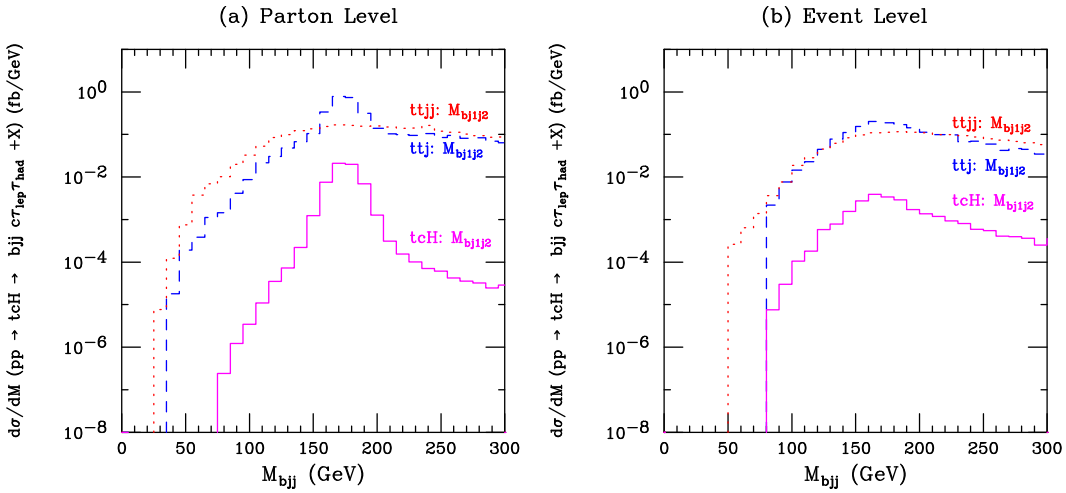


Figure 4.3: Invariant mass distribution $d\sigma/dM_{bjj}$ for the Higgs signal (magenta, solid) and for the dominant background from ttj (blue, dashed) and $ttjj$ (red, dot) at the LHC with $\sqrt{s} = 13$ TeV. Results are shown for (a) parton level, and (b) event level.

Figure **4.4** shows the invariant mass distributions $d\sigma/dM_{\tau\tau}$ for $m_H = 130$, 150, and 200 GeV. Clear peaks are observed near the Higgs boson mass for all values of m_H. The cross sections are evaluated for the scalar H^0 with $\tilde{\rho}_{tc} = 0.1$. In the alignment limit, the cross section for the pseudoscalar A^0 is comparable to that of H^0.

Furthermore, the invariant mass distributions $d\sigma/dM_{c\tau\tau}$ are presented in Fig. **4.5** for $m_\phi = 130$ and 150 GeV. Pronounced peaks are visible near the m_t for $m_\phi \leq 150$ GeV, while for $m_\phi > 150$ GeV, the $M_{c\tau\tau}$ peak becomes significantly broader due to reduced kinematic reconstruction accuracy. We require the reconstructed Higgs and top-quark masses to lie within the windows

$$\Delta M_{\tau\tau} = |M_{\tau\tau} - m_\phi| \leq 0.20\, m_\phi, \tag{4.6}$$

$$\Delta M_{c\tau\tau} = |M_{c\tau\tau} - m_t| \leq 0.25\, m_t, \tag{4.7}$$

for $m_\phi \leq 150$ GeV, following the ATLAS mass resolution [93].

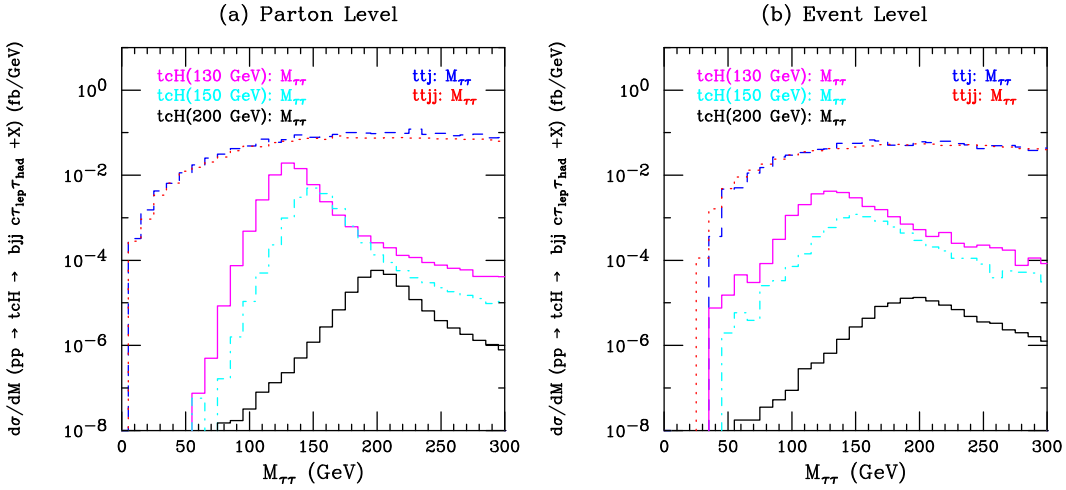


Figure 4.4: Invariant mass distributions $d\sigma/dM_{\tau\tau}$ for the Higgs signal with $m_H = 130$ GeV (magenta, solid), 150 GeV (green, dot-dashed), 200 GeV (black, solid) and for the dominant background from ttj (blue, dashed) and $ttjj$ (red, dot) at $\sqrt{s} = 13$ TeV. Results are shown for (a) parton level, and (b) event level with detector simulation in pp collisions.

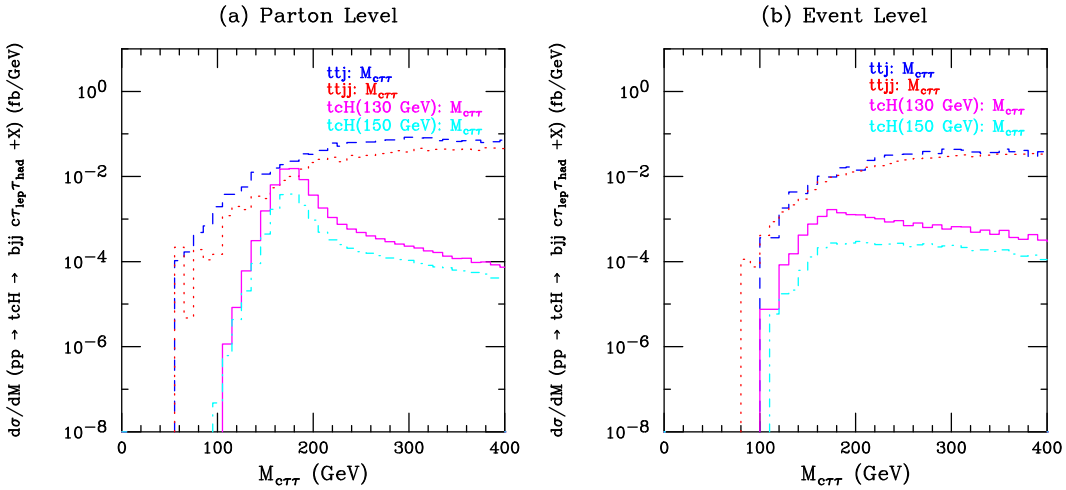


Figure 4.5: Invariant mass distributions $d\sigma/dM_{c\tau\tau}$ for the Higgs signal ($t \to c\phi^0$) with $m_H = 130$ GeV (magenta, solid) and 150 GeV (Green, dot-dashed) and for the dominant background from ttj (blue, dashed) and $ttjj$ (red, dot) at $\sqrt{s} = 13$ TeV. Results are shown for (a) parton level, and (b) event level with detector simulation in pp collisions.

In addition to all kinematic requirements and invariant-mass selections, the energy of the charm quark (E_c^*) in the rest frame of the top quark can be reconstructed to further discriminate the $t \to c\phi^0$ signal from the background [95]. For $m_\phi < m_t$, the charm-quark energy is given by

$$E_c^* = \frac{m_t}{2}\left(1 + \frac{m_c^2}{m_t^2} - \frac{m_\phi^2}{m_t^2}\right). \tag{4.8}$$

For example, when $m_\phi = 130$ GeV and 150 GeV, the E_c^* distribution exhibits clear enhancements at $E_c^* \simeq 37.4$ GeV and 21.2 GeV, respectively. Figure **4.6** shows the energy distributions of the charm quark in the top-quark rest frame for representative mass points. These distributions demonstrate that applying a selection cut of $E_c^* < 60$ GeV effectively suppresses background events while retaining most of the signal, thereby improving the overall discovery potential.

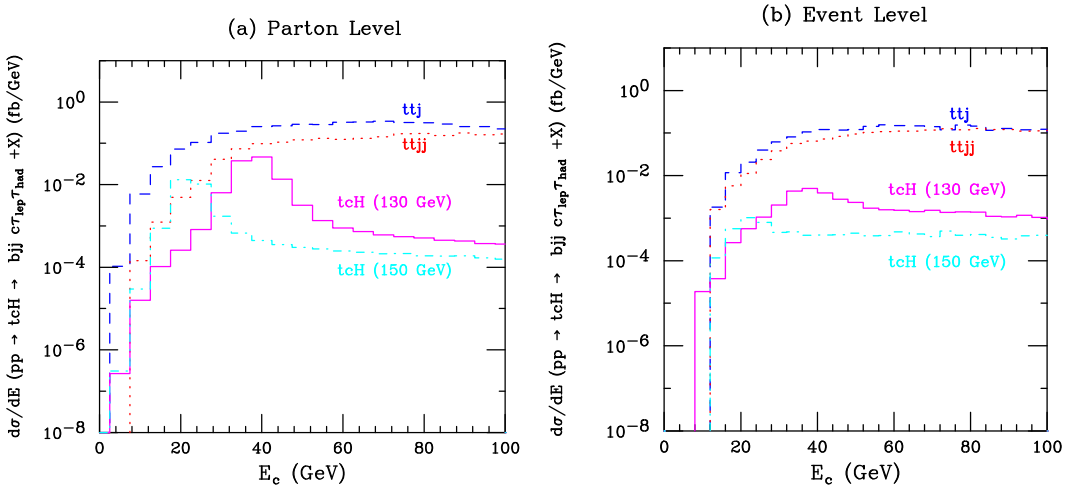


Figure 4.6: Energy distribution for the charm quark ($d\sigma/dE_c$) in the top rest frame for the Higgs signal from $t \to cH^0$ with $m_H = 130$ GeV (magenta, solid), 150 GeV (Green, dot-dashed) and for the dominant background from ttj (blue, dashed) and $ttjj$ (red, dot) at $\sqrt{s} = 13$ TeV. Results are shown for (a) parton level, and (b) event level with detector simulation in pp collisions.

From the invariant mass and the charm quark energy distributions at the

parton and event levels, the following mass requirements are deduced

(i) $|M_{j_1j_2} - m_W| \leq 0.20 \times m_W$ and $|M_{bj_1j_2} - m_t| \leq 0.25 \times m_t$,

(ii) $|M_{\tau\tau} - m_\phi| \leq 0.20 \times m_\phi$,

(iii) $|M_{c\tau\tau} - m_t| \leq 0.25 \times m_t$ for $m_\phi \leq 150$ GeV,

(iv) 0 GeV $\leq E_c^* \leq 60$ GeV for $m_\phi \leq 150$ GeV.

For $m_\phi > 150$ GeV, we stop at (ii) to both signal and background events. A summarized selection rules is presented in Table **4.2**.

selection rule	S_1	BG_1	S_2	BG_2
≥ 5 jets, 1 lepton	✓	✓	✓	✓
1 tagged b-jet, 1 tagged τ-jet	✓	✓	✓	✓
$p_T(j) > 25$ GeV, $\lvert\eta(j)\rvert < 2.5$	✓	✓	✓	✓
$p_T(l) > 20$ GeV, $\lvert\eta(l)\rvert < 2.5$	✓	✓	✓	✓
$\Delta R > 0.4$	✓	✓	✓	✓
$\not{E}_T > 30$ GeV	✓	✓	✓	✓
$\lvert M_{j_1j_2} - m_W\rvert \leq 0.20 \times m_W$	✓	✓	✓	✓
$\lvert M_{bj_1j_2} - m_t\rvert \leq 0.25 \times m_t$	✓	✓	✓	✓
$\lvert M_{\tau\tau} - m_\phi\rvert \leq 0.20 \times m_\phi$	✓	✓	✓	✓
$\lvert M_{c\tau\tau} - m_t\rvert \leq 0.25 \times m_t$	✓	✓	–	–
0 GeV $\leq E_c^* \leq 60$ GeV	✓	✓	–	–

Table 4.2: Selection criteria for signal and backgrounds events with $m_\phi \leq 150$ GeV and $m_\phi > 150$ GeV. In this table, S_1 represents signal events with $m_\phi \leq 150$ GeV , S_2 represents signal events with $m_\phi > 150$ GeV, BG_1 represents backgrounds events with $m_\phi \leq 150$ GeV and BG_2 represents signal events with $m_\phi > 150$ GeV.

4.1.3 Discovery Potential

We present parton level signal cross sections at $\sqrt{s} = 13$, 13.6, and 14 TeV for $\tilde{\rho}_{tc} = 0.1$ and 0.5 in Table **4.3**. The cross sections for the backgrounds are presented in Table **4.4**.

$\sqrt{s} = 13$ TeV	$\rho_{tc} = 0.1$	$\rho_{tc} = 0.5$
$m_H = 130$ GeV	0.3857 fb	9.657 fb
$m_H = 150$ GeV	0.1166 fb	2.889 fb
$m_H = 200$ GeV	0.0016 fb	0.0023 fb
$\sqrt{s} = 13.6$ TeV	$\rho_{tc} = 0.1$	$\rho_{tc} = 0.5$
$m_H = 130$ GeV	0.4241 fb	10.58 fb
$m_H = 150$ GeV	0.1300 fb	3.231 fb
$m_H = 200$ GeV	0.0018 fb	0.0025 fb
$\sqrt{s} = 14$ TeV	$\rho_{tc} = 0.1$	$\rho_{tc} = 0.5$
$m_H = 130$ GeV	0.4567 fb	11.47 fb
$m_H = 150$ GeV	0.1370 fb	3.434 fb
$m_H = 200$ GeV	0.0020 fb	0.0027 fb

Table 4.3: Parton level signal cross section in fb after all cuts with $\varepsilon_b = 0.7$ and $\varepsilon_\tau = 0.723$.

$\sqrt{s} = 13$ TeV	$t\bar{t}j$	$t\bar{t}jj(+\tau)$	$Zb\bar{b}jj$	Total
$m_H = 130$ GeV	0.7236 fb	0.1458 fb	5.4×10^{-2} fb	0.8753 fb
$m_H = 150$ GeV	4.826 fb	1.144 fb	3.6×10^{-2} fb	6.005 fb
$m_H = 200$ GeV	8.145 fb	1.668 fb	1.2×10^{-2} fb	9.824 fb
$\sqrt{s} = 13.6$ TeV	$t\bar{t}j$	$t\bar{t}jj(+\tau)$	$Zb\bar{b}jj$	Total
$m_H = 130$ GeV	0.8010 fb	0.1568 fb	5.9×10^{-2} fb	0.9640 fb
$m_H = 150$ GeV	5.326 fb	1.281 fb	4.0×10^{-2} fb	6.647 fb
$m_H = 200$ GeV	9.052 fb	1.849 fb	1.1×10^{-2} fb	10.91 fb
$\sqrt{s} = 14$ TeV	$t\bar{t}j$	$t\bar{t}jj(+\tau)$	$Zb\bar{b}jj$	Total
$m_H = 130$ GeV	0.8586 fb	0.1667 fb	6.3×10^{-2} fb	1.031 fb
$m_H = 150$ GeV	5.683 fb	1.378 fb	4.3×10^{-2} fb	7.103 fb
$m_H = 200$ GeV	9.639 fb	1.978 fb	1.2×10^{-2} fb	11.63 fb

Table 4.4: Background cross sections in fb after applying the mass selection at the parton level.

For event level, the signal cross section is shown in Table **4.5** and backgrounds in Table **4.6**.

$\sqrt{s} = 13$ TeV	$\rho_{tc} = 0.1$	$\rho_{tc} = 0.5$
$m_H = 130$ GeV	0.1589 fb	3.474 fb
$m_H = 150$ GeV	0.0907 fb	2.317 fb
$m_H = 200$ GeV	1.1×10^{-3} fb	1.5×10^{-3} fb
$\sqrt{s} = 13.6$ TeV	$\rho_{tc} = 0.1$	$\rho_{tc} = 0.5$
$m_H = 130$ GeV	0.1685 fb	4.108 fb
$m_H = 150$ GeV	0.1026 fb	2.677 fb
$m_H = 200$ GeV	1.2×10^{-3} fb	1.8×10^{-3} fb
$\sqrt{s} = 14$ TeV	$\rho_{tc} = 0.1$	$\rho_{tc} = 0.5$
$m_H = 130$ GeV	0.1894 fb	8.050 fb
$m_H = 150$ GeV	0.1031 fb	5.638 fb
$m_H = 200$ GeV	1.4×10^{-3} fb	2.0×10^{-3} fb

Table 4.5: Event level signal cross section in fb after all cuts.

We evaluate the statistical significance (N_{SS}) as a function of $\tilde{\rho}_{tc}$ and m_ϕ in this study, where N_{SS} is calculated using Eq. (**2.18**).

Figure **4.7** shows the signal cross section as a function of the Higgs boson mass (m_H) for $\tilde{\rho}_{tc} = 0.1$ and 0.5. In the alignment limit of the 2HDM, where $\sin(\beta - \alpha) \to 1$, the production cross sections of the heavy scalar (H^0) and pseudoscalar (A^0) are nearly identical. When the two neutral Higgs bosons are mass-degenerate ($m_H \simeq m_A$), the signal cross section and corresponding statistical significance effectively double.

We observe that the cross section decreases rapidly with increasing m_H for $m_H < m_t$, as the charm quark becomes less energetic when m_H approaches m_t. In contrast, for $m_H > m_t$, the cross section falls more slowly, indicating that the sensitivity to m_H becomes less pronounced once the top quark becomes off-shell and the $H \to t\bar{c}$ decay channel opens.

$\sqrt{s} = 13$ TeV	$t\bar{t}j$	$t\bar{t}jj(+\tau)$	$Zb\bar{b}jj$	Total
$m_H = 130$ GeV	0.7157 fb	0.3559 fb	1.6×10^{-2} fb	1.088 fb
$m_H = 150$ GeV	4.689 fb	1.904 fb	4.1×10^{-2} fb	6.635 fb
$m_H = 200$ GeV	6.860 fb	2.720 fb	1.4×10^{-2} fb	9.594 fb
$\sqrt{s} = 13.6$ TeV	$t\bar{t}j$	$t\bar{t}jj(+\tau)$	$Zb\bar{b}jj$	Total
$m_H = 130$ GeV	0.8734 fb	0.3982 fb	2.5×10^{-2} fb	1.297 fb
$m_H = 150$ GeV	5.098 fb	2.173 fb	4.3×10^{-2} fb	7.313 fb
$m_H = 200$ GeV	7.065 fb	3.200 fb	2.2×10^{-2} fb	10.29 fb
$\sqrt{s} = 14$ TeV	$t\bar{t}j$	$t\bar{t}jj(+\tau)$	$Zb\bar{b}jj$	Total
$m_H = 130$ GeV	0.9331 fb	0.4034 fb	2.7×10^{-2} fb	1.364 fb
$m_H = 150$ GeV	5.544 fb	2.266 fb	5.0×10^{-2} fb	7.859 fb
$m_H = 200$ GeV	7.367 fb	3.204 fb	2.9×10^{-2} fb	10.60 fb

Table 4.6: Background cross sections in fb after applying the mass selection at the event level.

Figure **4.8** presents the signal cross section as a function of $\tilde{\rho}_{tc}$ for $m_H = 130$, 150, and 200 GeV. For $m_H < m_t$, the cross section scales approximately as $\sigma \propto \tilde{\rho}_{tc}^2$. However, for $m_H > m_t$, the cross section remains nearly constant, reflecting the reduction in the $H^0 \to \tau^+\tau^-$ branching fraction once the $H^0 \to t\bar{c}$ mode becomes kinematically accessible, as shown in Fig. **2.2**. Thus, the enhancement from the $\tilde{\rho}_{tc}^2$ dependence in the production process $pp \to t\bar{t} \to tc\phi^0 \to tc\tau^+\tau^- + X$ is largely compensated by the increase in the total width when $H^0 \to t\bar{c}$ dominates.

The 5σ discovery reach at the LHC with $\sqrt{s} = 13.6$ TeV is shown in Fig. **4.9**, while Fig. **4.10** illustrates the mass-degenerate case ($m_H = m_A$) for both parton-level and event-level analyses in the [$\tilde{\rho}_{tc}$, m_ϕ] plane. Three benchmark integrated luminosities are considered: $\mathcal{L} = 30$, 300, and 3000 fb^{-1}. It is evident that for Higgs boson masses below the top-quark mass, the high-luminosity LHC operating at $\sqrt{s} = 14$ TeV with $\mathcal{L} = 3000$ fb^{-1} significantly enhances the discovery potential of the FCNH signal.

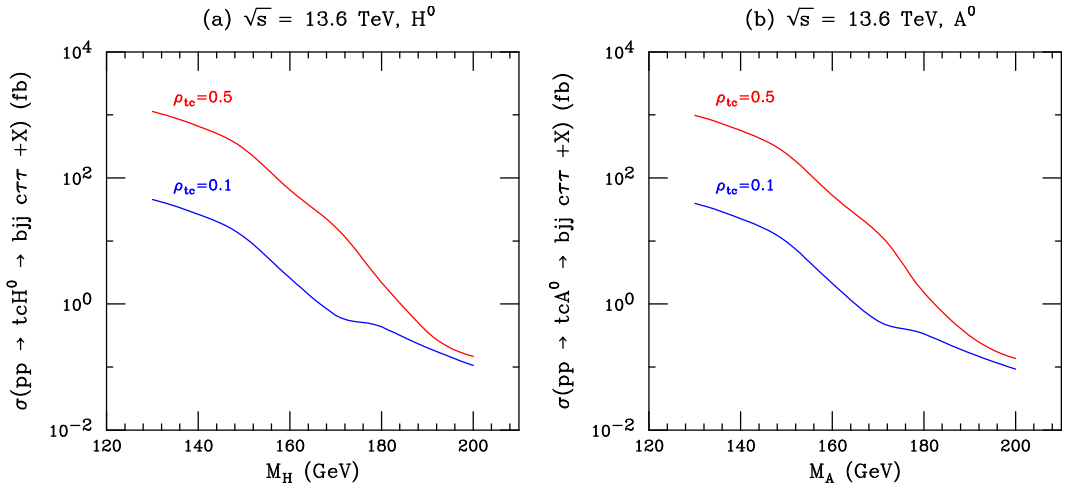


Figure 4.7: Signal cross section σ vs. mass of Higgs boson for the FCNH signal ($t \to c\Phi^0$) with $\rho_{tc} = 0.1$ (blue) and 0.5 (red) at $\sqrt{s} = 13.6$ TeV, where ϕ^0 is (a) Heavy Scalar H^0, and (b) pseudoscalar A^0 with detector simulation in pp collisions.

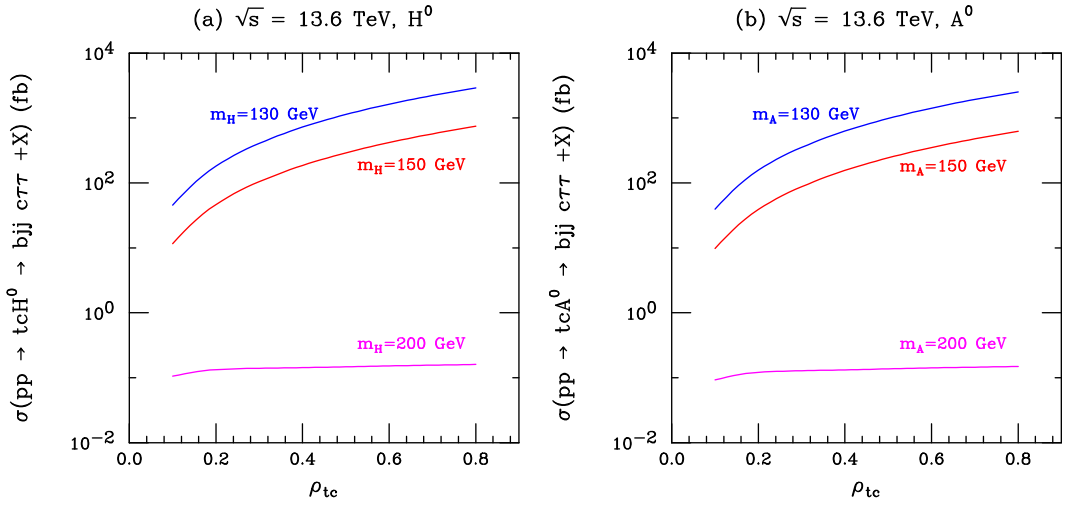


Figure 4.8: Signal cross section σ vs. ρ_{tc} of Higgs boson for the FCNH signal ($t \to c\Phi^0$) with $m_\phi = 130$ GeV (blue), 150 GeV (red) and 200 GeV (magenta) at $\sqrt{s} = 13.6$ TeV, where Φ^0 is (a) Heavy Scalar H^0, and (b) pseudoscalar A^0 with detector simulation in pp collisions.

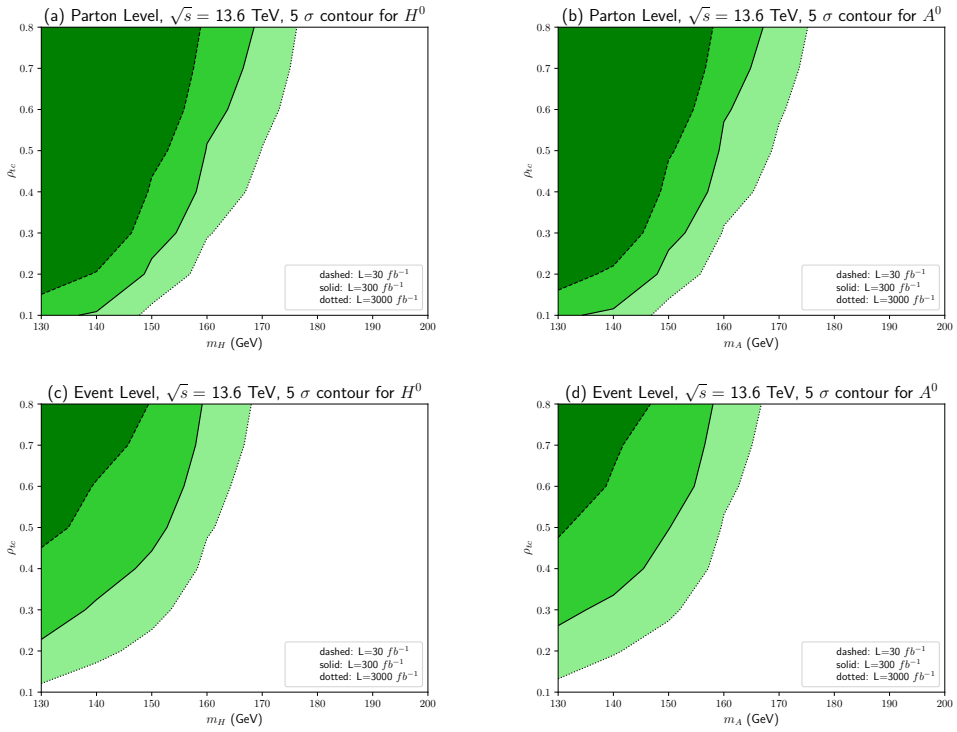


Figure 4.9: Parton Level and Event Level 5σ discovery contours at the LHC at $\sqrt{s} = 13.6$ TeV in the $[m_\Phi, \tilde{\rho}_{tc}]$ plane for (a) Parton Level Heavy Scalar H^0, (b) Parton Level pseudoscalar A^0, (c) Event Level Heavy Scalar H^0 and (d) Event Level pseudoscalar A^0 with $L = 30fb^{-1}$ (dark green dotted dashed), $300fb^{-1}$ (medium green solid) and $L = 3000fb^{-1}$ (light green dashed)

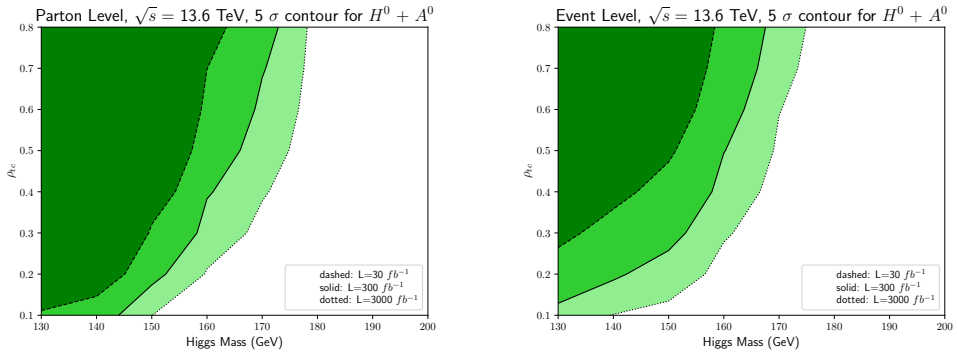


Figure 4.10: Parton Level and Event Level 5σ discovery contours of Higgs mass degenerate case at the LHC at $\sqrt{s} = 13.6$ TeV in the $[m_\Phi, \tilde{\rho}_{tc}]$ plane for Parton Level (left) and Event Level (right) with $L = 30fb^{-1}$ (dark green dotted dashed), $300fb^{-1}$ (medium green solid) and $L = 3000fb^{-1}$ (light green dashed)

4.2 Top Pairs with Flavor Changing Neutral Higgs Decays

4.2.1 The Higgs Signal and Standard Model background

From this section, we present the discovery study of the process $pp \to t\phi \to t(tc)$, with leading-order Feynman diagrams shown in Fig. **4.11**. The signal is categorized into two distinct channels according to their final-state configurations: the all-top channel, corresponding to the full process $pp \to ttc \to bjjc\,b\ell\nu + X$, and the same-sign top (SS-top) channel, $pp \to ttc \to bbc\,\ell\ell\nu\nu + X$, where the two leptons are required to have the same electric charge.

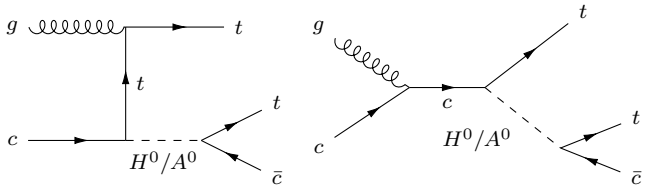


Figure 4.11: Leading-order Feynman diagrams for $pp \to t\phi \to t(tc)$.

The complete Monte Carlo simulation is carried out using MadGraph 5 [58], Pythia 8 [60], and Delphes [63]. The signal cross section is evaluated using the CT14LLO parton distribution functions [80], with the renormalization and factorization scales set to $\mu_{R,F} = m_H + m_t$. Applying the above scale choices and PDFs, our current estimates suggest a K-Factor of ≈ 1.42, and is approximately the same for all three energies ($\sqrt{s} = 13$, 13.6, and 14 TeV). The K-factors are calculated using MadGraph5.

All-top Channel. The dominant Standard Model background to the signal contributed by $pp \to t\bar{t}j \to bjjj\,b\ell\nu + X$ (ttj). Using the same simulation framework

and parton distribution functions (PDFs) as for the signal, we compute the cross sections with both the renormalization and factorization scales set to $\mu_{R,F} = \sqrt{\hat{s}}$. With identical choices of PDFs and scales, the K-factor for the ttj process is calculated using MadGraph5 and found to be approximately 1.10 for all collider energies considered.

SS-top Channel. By requiring two same-sign leptons in the final state, the dominant Standard Model backgrounds arise from $pp \to t\bar{t}W^{\pm} \to bbjj\,\ell\ell\nu\nu$ (ttW) and, to a lesser extent, from $pp \to t\bar{t}Z \to bbjj\,\ell\ell\ell\nu\nu$ (ttZ). The cross sections are evaluated with the same choice of PDFs and scale settings, $\mu_{R,F} = \sqrt{\hat{s}}$. Following Ref. [81], the corresponding K-factors are $K_{\mathrm{ttW}} = 1.59$ and $K_{\mathrm{ttZ}} = 1.44$.

4.2.2 Mass Reconstruction and Realistic Acceptance Cuts

According to the distinct final-state particles, the selection strategies are optimized separately for the all-top and SS-top channels. This section presents the corresponding mass reconstruction and realistic acceptance criteria for both cases. The same tagging efficiencies are applied as described in Section 3.2.3.

All-top Channel

In this channel, the final state consists of five jets, including two b-jets, one c-jet, two light jets, and one isolated lepton. Among them, one b-jet together with the two light jets originates from the hadronically decaying top quark, while the remaining b-jet and the lepton arise from the leptonically decaying top quark. In addition, the c-jet and the leptonically decaying top quark both originate from the decay of the Higgs boson. Since one of the light jets from the W decay may also be identified as a c-jet, the light jets are selected prior to c-tagging in the

event reconstruction. Based on this topology, the following basic selection cuts are imposed:

(i) At least five jets, including two b-tagged jets and at least one c-tagged jet, with $p_T \geq 25$ GeV and $|\eta| \leq 2.5$;

(ii) Exactly one isolated lepton with $p_T \geq 20$ GeV and $|\eta| \leq 2.5$;

(iii) The angular separation between any pair of reconstructed objects satisfies $\Delta R > 0.4$;

(iv) Missing transverse energy $\not{E}_T \geq 25$ GeV.

Since there is only a single isolated lepton and missing transverse energy arising from the neutrino in this final state, the longitudinal component of the neutrino momentum (k_z) can be determined using the on-shell W-boson mass constraint,

$$(k+p)^2 = m_W^2, \tag{4.9}$$

where p and k denote the four-momenta of the lepton and neutrino, respectively. Solving for k_z yields two possible solutions:

$$k_z^{\pm} = \frac{p_z\big(2\,\mathbf{k}_T\cdot\mathbf{p}_T + m_W^2 - m_\ell^2\big) \pm E_\ell\,\Delta}{2(m_\ell^2 + p_T^2)}, \tag{4.10}$$

$$\Delta^2 = \big(2\,\mathbf{k}_T\cdot\mathbf{p}_T + m_W^2 - m_\ell^2\big)^2 - 4\,k_T^2(m_\ell^2 + p_T^2). \tag{4.11}$$

If $\Delta^2 \leq 0$, it is set to zero, in which case the two solutions k_z^+ and k_z^- become identical. For $\Delta^2 > 0$, both $k_z^{\pm}$ solutions are retained. Among them, the solution that minimizes the reconstructed top-mass deviation, $|M_{b_i\ell\nu} - m_t| + |M_{\ell\nu} - m_W|$ or equivalently $|(p_{b_i} + p + k)^2 - m_t^2| + |(p+k)^2 - m_W^2|$ is selected, subject to the

additional requirement $|M_{\ell\nu} - m_W| < 0.1\ m_W$. Once the appropriate solution is chosen, the neutrino momentum can be fully reconstructed, allowing selection of the b-jet originating from the Higgs boson, denoted by b_1. Figure **4.12** presents the distribution of reconstructed $M_{l\nu}$ (left) and $M_{b_1 l\nu}$ (right).

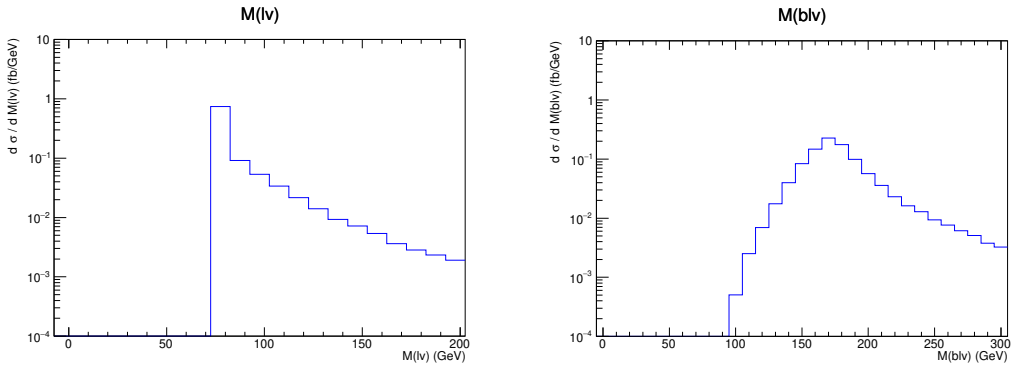


Figure 4.12: Invariant mass distribution $d\sigma/dM_{l\nu}$ (left) and $d\sigma/dM_{b_1 l\nu}$ (right) for the Higgs signal.

Similar to the $\phi^0 \to \tau^+\tau^-$ analysis, two light jets are selected by minimizing $|M_{jj} - m_W|$ and $|M_{bjj} - m_t|$ among the remaining b-jet (denoted by b_2) and light-jet candidates. Subsequently, c-tagging is applied to the remaining unassigned jets, requiring exactly one c-tagged jet in the event. The reconstructed W- and top-quark masses are required to fall within the mass windows $\Delta M_{j_1 j_2} = 0.20\, m_W$ and $\Delta M_{b_2 j_1 j_2} = 0.25\, m_t$, respectively.

Furthermore, the invariant mass distributions $d\sigma/dM_{cb_1 l\nu}$ are shown in Fig. **4.13** for $m_H = 200$ and 400 GeV with $\tilde{\rho}_{tc} = 0.4$. Pronounced peaks are observed around the Higgs masses, with the distribution for $m_H = 200$ GeV appearing sharper and that for $m_H = 400$ GeV slightly broader due to kinematic effects. Finally, we require the reconstructed Higgs- and top-quark candidate masses to satisfy conditions $|M_{cb_1 l\nu} - m_H| \leq 0.25\, m_H$ and $|M_{b_1 l\nu} - m_t| \leq 0.25\, m_t$.

In this channel, E_c^* in the rest frame of the Higgs boson can be reconstructed

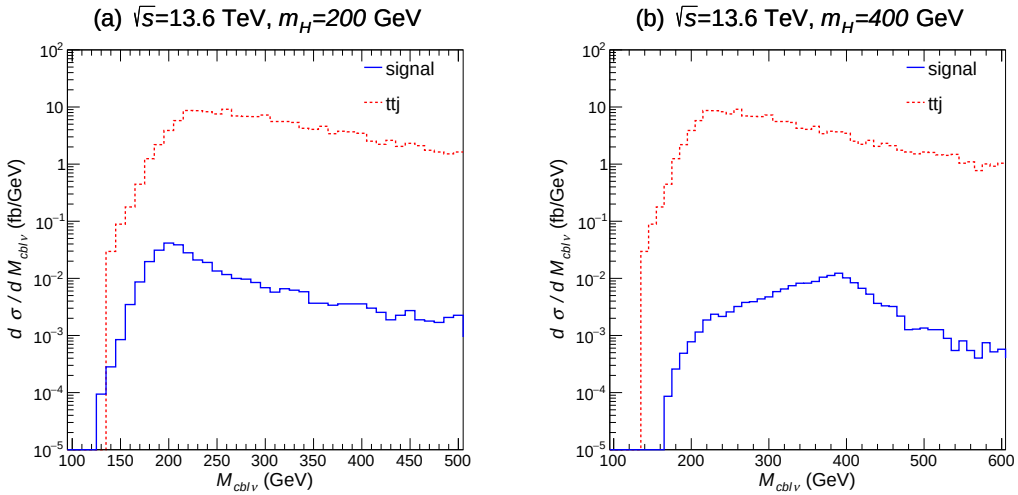


Figure 4.13: Invariant mass distributions $d\sigma/dM_{cb_1l\nu}$ for the Higgs signal signal and dominant backgrounds $t\bar{t}j$ (red, dashed) at $\sqrt{s} = 13.6$ TeV, shown for $\tilde{\rho}_{tc} = 0.4$, (a) $m_H = 200$ GeV (blue, solid) and (b) $m_H = 400$ GeV (blue, solid).

to further discriminate the signal from the background. Analogous to Eq. (**4.8**), the charm-quark energy is given by

$$E_c^* = \frac{m_\phi}{2}\left(1 + \frac{m_c^2}{m_\phi^2} - \frac{m_t^2}{m_\phi^2}\right). \tag{4.12}$$

For instance, for $m_\phi = 200$ GeV and 400 GeV, the E_c^* distribution exhibits pronounced peaks around $E_c^* \simeq 25.5$ GeV and 162.8 GeV, respectively. Figure **4.14** displays the charm-quark energy spectra in the Higgs rest frame for representative benchmark points. From these distributions, suitable selection cuts on E_c^* can be applied to effectively suppress background contributions. The detailed ranges for various m_ϕ hypotheses are summarized in Appendix 5.

These selection requirements are optimized to suppress background processes while enhancing the statistical significance of the signal. The complete set of final selection criteria applied to both signal and background events is summarized in Table **4.7**.

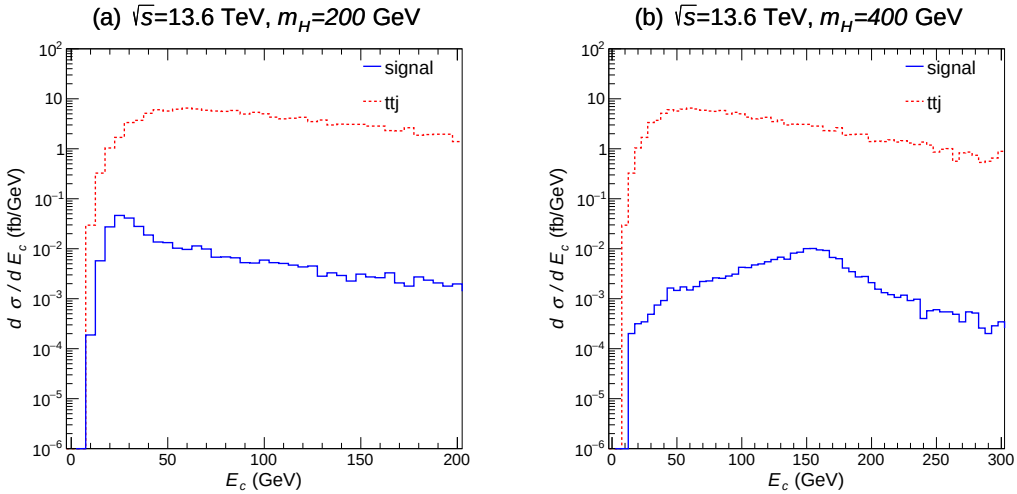


Figure 4.14: Energy distribution for the charm quark ($d\sigma/dE_c$) in the Higgs rest frame for the Higgs signal from $H^0 \to t\bar{c}$ with (a) $m_H = 200$ GeV (blue, solid), (b) $m_H = 400$ GeV (blue, solid) with $\tilde{\rho}_{tc} = 0.4$, at $\sqrt{s} = 13.6$ TeV. Dominant background are also presented (red, dotted) in both cases.

Selection Criteria
1 tagged c-jet, 2 tagged b-jets, and at least 3 light jets
$p_T(j) > 25$ GeV, $\lvert\eta(j)\rvert < 2.5$
1 lepton with $p_T(\ell) > 20$ GeV, $\lvert\eta(\ell)\rvert < 2.5$, $\Delta R > 0.4$
$\not{E}_T > 25$ GeV
$\lvert M_{\ell\nu} - m_W\rvert \leq 0.10\, m_W$
$\lvert M_{jj} - m_W\rvert \leq 0.20\, m_W$, $\lvert M_{b_2jj} - m_t\rvert \leq 0.25\, m_t$
$\lvert M_{b_1\ell\nu} - m_t\rvert \leq 0.25\, m_t$, $\lvert M_{cb_1\ell\nu} - m_\phi\rvert \leq 0.25\, m_\phi$
Optimized E_c^* cuts

Table 4.7: Final selection criteria applied to the signal and background events in the all-top channel.

SS-top Channel

For the SST channel, the final state consists of two b-jets, one c-jet, and two leptons of the same electric charge ($q(\ell_1)\, q(\ell_2) > 0$). Due to the presence of two neutrinos in the final state, it is not possible to fully reconstruct their momenta, nor to apply cuts on the charm-quark energy E_c^*. Moreover, from the p_T^c distributions corresponding to different m_ϕ hypotheses, we find that a cut on p_T^c only begins to enhance the statistical significance for $m_\phi \gtrsim 400$ GeV (see Appendix 5). Fortunately, the requirement of two same-sign leptons is already highly effective in suppressing the Standard Model backgrounds. As a result, the SS-top channel requires a considerably simpler set of selection criteria compared to the all-top channel, as summarized in Table **4.8**.

Selection Criteria
1 tagged c-jet, 2 tagged b-jets
$p_T(j) > 25$ GeV, $\lvert\eta(j)\rvert < 2.5$
2 same-sign lepton with $p_T(\ell) > 20$ GeV, $\lvert\eta(\ell)\rvert < 2.5$, $\Delta R > 0.4$
$\not{E}_T > 30$ GeV
$p_T^c > 60$ GeV, for $m_\phi \in [400, 500)$ GeV
$p_T^c > 70$ GeV, for $m_\phi = 500$ GeV

Table 4.8: Final selection criteria applied to the signal and background events in the SS-top channel.

4.2.3 Discovery Potential at the LHC

After applying all selection criteria at collider energies of $\sqrt{s} = 13$, 13.6, and 14 TeV, the all-top and same-sign top signal cross sections for various benchmark points (BPs), together with the corresponding background cross sections, are summarized in Table **4.9** and Table **4.10**, respectively. The statistical significances N_{SS}, evaluated for both the H^0-only and the mass-degenerate scenarios, are also

$\sqrt{s}$ (TeV)	$\sigma_H(\mathrm{BP}_1)$ (fb)	$\sigma_A(\mathrm{BP}_1)$ (fb)	$t\bar{t}j$ (fb)	$N_{SS}(H^0)$	N_{SS}
13	0.2650	0.2661	16.28	1.46	2.93
13.6	0.2829	0.2932	17.80	1.50	3.04
14	0.3169	0.3196	18.28	1.65	3.31
$\sqrt{s}$ (TeV)	$\sigma_H(\mathrm{BP}_2)$ (fb)	$\sigma_A(\mathrm{BP}_2)$ (fb)	$t\bar{t}j$ (fb)	$N_{SS}(H^0)$	N_{SS}
13	0.1309	0.0861	19.99	0.65	1.08
13.6	0.1385	0.0955	22.64	0.65	1.10
14	0.1550	0.0977	23.79	0.71	1.16

Table 4.9: All-top signal and background cross sections. The benchmark points correspond to $\tilde{\rho}_{tc} = 0.4$ with $(m_H,\, m_A) = (200,\, 200)\,\mathrm{GeV}$ (BP_1) and $(400,\, 400)\,\mathrm{GeV}$ (BP_2). The signal cross sections are denoted by σ_H and σ_A for the H^0 and A^0 channels, respectively. The statistical significance is evaluated for an integrated luminosity of $L = 500$ fb^{-1}, with $N_{SS}(H^0)$ representing the H^0 channel and N_{SS} for the degenerate case.

$\sqrt{s}$ (TeV)	$\sigma_H(\mathrm{BP}_1)$ (fb)	$\sigma_A(\mathrm{BP}_1)$ (fb)	$t\bar{t}W^{\pm}$ (fb)	$t\bar{t}Z$ (fb)	Total (fb)	$N_{SS}(H^0)$	N_{SS}
13	0.1859	0.1835	0.0515	0.0021	0.0537	13.1	22.5
13.6	0.2061	0.2079	0.0544	0.0022	0.0566	14.0	24.1
14	0.2129	0.2133	0.0573	0.0022	0.0595	14.2	24.4
$\sqrt{s}$ (TeV)	$\sigma_H(\mathrm{BP}_2)$ (fb)	$\sigma_A(\mathrm{BP}_2)$ (fb)	$t\bar{t}W^{\pm}$ (fb)	$t\bar{t}Z$ (fb)	Total (fb)	$N_{SS}(H^0)$	N_{SS}
13	0.0868	0.0570	0.0216	0.0010	0.0227	9.25	13.7
13.6	0.0977	0.0647	0.0228	0.0011	0.0240	10.0	14.8
14	0.1030	0.0682	0.0244	0.0011	0.0255	10.2	15.2

Table 4.10: Same-sign top signal and background cross sections. The benchmark points correspond to $\tilde{\rho}_{tc} = 0.4$ with $(m_H,\, m_A) = (200,\, 200)\,\mathrm{GeV}$ (BP_1) and $(400,\, 400)\,\mathrm{GeV}$ (BP_2). The signal cross sections are denoted by σ_H and σ_A for the H^0 and A^0 channels, respectively. The statistical significance is evaluated for an integrated luminosity of $L = 500$ fb^{-1}, with $N_{SS}(H^0)$ representing the H^0 channel and N_{SS} for the mass degenerate case.

presented in the tables for an integrated luminosity of $L = 500$ fb^{-1}.

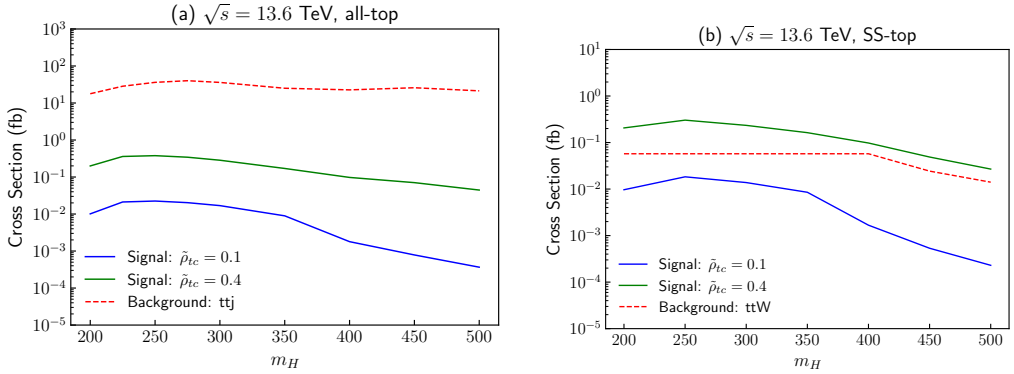


Figure 4.15: The cross sections as functions of m_H for (a) the all-top signal and its dominant background $t\bar{t}j$ (red, dashed), and (b) the same-sign top signal and its dominant background $t\bar{t}W$ (red, dashed). Both signal channels are shown for two benchmark values of $\tilde{\rho}_{tc}$: $\tilde{\rho}_{tc} = 0.1$ (blue, solid) and $\tilde{\rho}_{tc} = 0.4$ (green, solid).

Figure **4.15** illustrates the dependence of the cross section on $\tilde{\rho}_{tc}$ for (a) $m_H = 200$ GeV and (b) $m_H = 400$ GeV at a collider energy of $\sqrt{s} = 13.6$ TeV. Figure **4.16** presents the 5σ discovery contours at the LHC in the (m_H, $\tilde{\rho}_{tc}$) plane for the following cases: (a) All-top channel at $\sqrt{s} = 13$ TeV, (b) SS-top channel at $\sqrt{s} = 13$ TeV, (c) All-top channel at $\sqrt{s} = 13.6$ TeV, (d) SS-top channel at $\sqrt{s} = 13.6$ TeV, (e) degenerate $m_H = m_A$ All-top channel at $\sqrt{s} = 13.6$ TeV, and (f) degenerate $m_H = m_A$ SS-top channel at $\sqrt{s} = 13.6$ TeV. The contours correspond to integrated luminosities of $L = 300$ fb^{-1} (dark-green solid) and $L = 3000$ fb^{-1} (light-green dotted). In addition, the 3σ discovery contours for $L = 3000$ fb^{-1} (red dotted) are shown for both $\sqrt{s} = 13$ TeV and 14 TeV scenarios.

The results indicate that the same-sign top channel provides a strong discovery potential, achieving significant sensitivity even with an integrated luminosity of $L = 300$ fb^{-1}. In contrast, the all-top channel, while less sensitive, offers valuable complementary information on the Higgs boson mass reconstruction. Furthermore, at higher collider energies and luminosities (e.g., $\sqrt{s} = 13.6$ TeV with

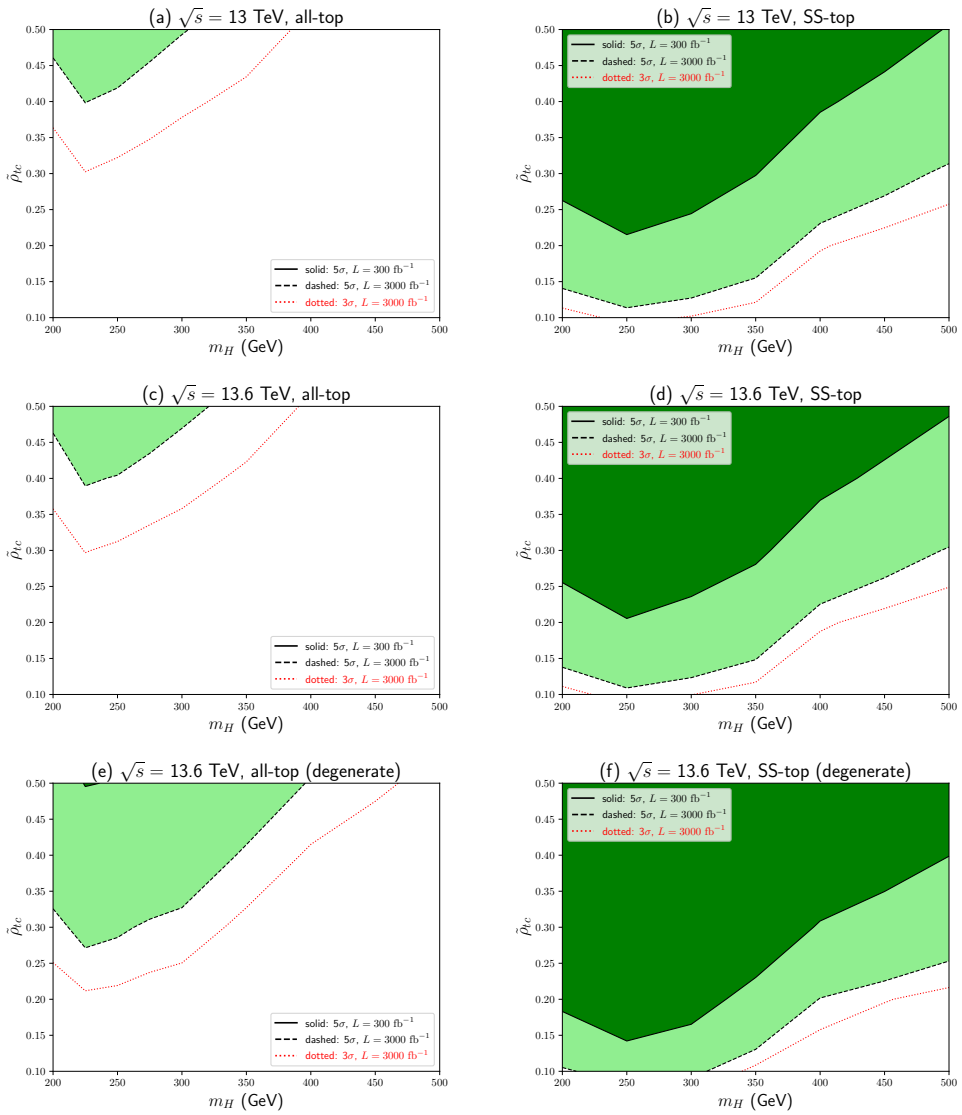


Figure 4.16: The 5σ discovery contours at the LHC in the $(m_H, \tilde{\rho}_{tc})$ plane are shown for: (a) All-top final state at $\sqrt{s} = 13$ TeV, (b) Same-sign top final state at $\sqrt{s} = 13$ TeV, (c) All-top final state at $\sqrt{s} = 13.6$ TeV, (d) Same-sign top final state at $\sqrt{s} = 13.6$ TeV, (e) degenerate $m_H = m_A$ all-top final state at $\sqrt{s} = 13.6$ TeV, and (f) degenerate $m_H = m_A$ same-sign top final state at $\sqrt{s} = 13.6$ TeV. The contours correspond to integrated luminosities of $L = 100$ fb^{-1} (dark-green dashed), 300 fb^{-1} (medium-green solid), and 3000 fb^{-1} (light-green dotted). In addition, the 3σ discovery contours for $L = 3000$ fb^{-1} (red dotted) are shown for both 13 TeV and 14 TeV scenarios.

$\mathcal{L} = 3000$ fb^{-1}), the all-top channel still probes a substantial region of parameter space, with its reach further enhanced in the mass-degenerate scenario.

4.3 Summary of Chapter 4

Chapter 4 investigates collider signatures of heavy neutral Higgs bosons H^0 and A^0 in the G2HDM that interact with the top quark through flavor-changing Yukawa couplings. Two complementary processes are studied in detail: Higgs production in top-quark decays with τ pairs, and flavor-changing top–Higgs associated production.

The first part of the chapter examines the process $pp \to t\bar{t} \to (bjj)\,(\bar{c}\phi^0) \to (bjj)\,(\bar{c}\,\tau^+\tau^-) + X$, which probes the lighter mass region $m_\phi \lesssim 200$ GeV. A full simulation of the signal and the leading backgrounds—primarily $t\bar{t}j$ and $t\bar{t}jj$—is performed using realistic detector effects. Reconstruction strategies for τ-leptons and the Higgs mass are optimized to enhance sensitivity. The results show that for $\sqrt{s} = 14$ TeV and $\mathcal{L} = 3000$ fb^{-1}, the signal becomes detectable for $\tilde{\rho}_{tc} \gtrsim 0.1$ and $m_\phi < 170$ GeV, with a significant enhancement in the mass-degenerate scenario $m_H \simeq m_A$.

The second part focuses on the process $pp \to t\phi^0 \to t(tc) + X$, which leads to two distinct channels: (i) the all-top channel, containing one hadronic and one leptonic top decay, and (ii) the SS-top channel, in which both top quarks decay leptonically and yield same-sign leptons. Detailed event-level simulations are conducted for $\sqrt{s} = 13$, 13.6, and 14 TeV, and optimized selection strategies are designed for each channel. While the all-top channel suffers from significant backgrounds from $t\bar{t}j$, the SS-top channel benefits from low Standard Model backgrounds dominated by $t\bar{t}W$ and $t\bar{t}Z$.

The SS-top channel exhibits strong discovery potential, offering sensitivity to a wide range of $\tilde{\rho}_{tc}$ values even at moderate luminosities. At $\sqrt{s} = 13.6$ TeV with $\mathcal{L} = 3000$ fb^{-1}, the SST signal remains observable for $\tilde{\rho}_{tc} \gtrsim 0.15$ and $m_H \lesssim 350$ GeV, extending to $\tilde{\rho}_{tc} \gtrsim 0.3$ at $m_H = 500$ GeV. In contrast, the all-top channel is more limited but provides valuable complementary information through direct Higgs mass reconstruction, with improved reach in the mass-degenerate scenario.

Overall, Chapter 4 demonstrates that heavy neutral Higgs bosons with flavor-changing couplings to the top quark can produce striking collider signatures, especially in top-associated production modes. Together with the charged Higgs study of Chapter 3, these results highlight the rich discovery potential of extended Higgs sectors at current and future LHC luminosities.

Chapter 5

Conclusion

In this dissertation, we have investigated the discovery potential of extended Higgs sectors beyond the Standard Model, with a particular focus on both charged and neutral BSM Higgs bosons within the framework of the G2HDM. With the theoretical foundation introduced in Chapter 1 and the motivations and analysis strategies summarized in Chapter 2, we conducted detailed collider studies of the characteristic flavor-changing processes mediated by the charged and neutral BSM Higgs bosons, as discussed in Chapter 3 and Chapter 4, respectively.

For the charged Higgs sector, we investigated the flavor-changing process $pp \to bH^+ \to bc\bar{b} + X$, along with the dominant Standard Model backgrounds $b\bar{b}j$ and $c\bar{c}j$, and evaluated the discovery prospects at collider energies of $\sqrt{s} = 13$, 13.6, and 14 TeV under current experimental constraints. Through a comprehensive analysis incorporating realistic detector effects and optimized selection cuts, we demonstrated that this channel can serve as a promising probe for the discovery of the charged Higgs boson. Moreover, since the coupling λ_{H^+cb} is directly proportional to $\rho_{tc}V_{tb}$, this process is particularly sensitive to ρ_{tc} and can provide meaningful constraints on its magnitude. Our results show that, at $\sqrt{s} = 14$ TeV, the signal remains observable for $\rho_{tc} \gtrsim 0.1$ and $m_{H^+} \lesssim 450$ GeV with an integrated luminosity of $L = 3000$ fb^{-1}.

For the neutral heavy Higgs bosons, we analyzed two distinct processes:

(i) $pp \to t\bar{t} \to (bjj)(\bar{c}\phi^0) \to (bjj)(\bar{c}\tau^+\tau^-) + X$, where one τ decays leptonically and the other hadronically, targeting the lighter mass range of $m_\phi \lesssim 200$ GeV. The dominant Standard Model backgrounds for this signal arise from (a) $t\bar{t}j$,

with one top quark decaying hadronically and the other leptonically, and (b) $t\bar{t}jj$, with both tops decaying leptonically. We performed both parton-level and event-level analysis, incorporating realistic detector effects and optimized selection techniques to suppress the backgrounds. Based on our event-level results, we find that at the collider energy $\sqrt{s} = 14$ TeV with an integrated luminosity of $\mathcal{L} = 3000$ fb^{-1} can detect this FCNH signal for $\tilde{\rho}_{tc} \gtrsim 0.1$ and $m_\phi < 170$ GeV. In the case of near mass degeneracy between the CP-even and CP-odd Higgs bosons ($m_H \simeq m_A$), the signal cross section and discovery significance can approximately double.

(ii) $pp \to t\phi^0 \to t(tc) + X$, which is further divided into two channels: (a) the all-top channel, with one top quark decaying hadronically and the other leptonically; and (b) the SS-top channel, where both top quarks decay leptonically, producing leptons with the same charge. The dominant Standard Model backgrounds originate from $t\bar{t}j$ for the all-top channel and from $t\bar{t}W$ and $t\bar{t}Z$ for the SS-top channel. Selection criteria are optimized separately for each channel, reflecting the different final-state configurations and background compositions. Incorporating realistic detector effects and the corresponding selection cuts, we carried out a detailed event-level analysis for collider energies of $\sqrt{s} = 13$, 13.6, and 14 TeV.

Our results show that at $\sqrt{s} = 13.6$ TeV, the SS-top channel exhibits a strong discovery potential, achieving observable significance for a large parameter space even with a luminosity of $L = 500$ fb^{-1}. For higher luminosity $L = 3000$ fb^{-1}, the signal remains detectable for $\tilde{\rho}_{tc} \gtrsim 0.15$ and $m_H \lesssim 350$ GeV, and for $\tilde{\rho}_{tc} \gtrsim 0.3$ at $m_H = 500$ GeV. In contrast, the all-top channel is more background-dominated, becoming observable only for $\tilde{\rho}_{tc} \gtrsim 0.39$ and

$m_H \lesssim 320$ GeV. However, in the mass-degenerate scenario ($m_H = m_A$), the sensitivity improves to $\tilde{\rho}_{tc} \gtrsim 0.27$ and $m_H \lesssim 400$ GeV. While the discovery potential of the all-top channel is less significant than that of the SS-top channel, it provides valuable complementary information through the kinematic reconstruction of the Higgs boson mass.

Overall, the results demonstrate that flavor-changing Higgs interactions in the G2HDM framework offer distinctive collider signatures that can be probed at current and future LHC luminosities. The combined exploration of charged and neutral Higgs channels provides complementary sensitivity to the Yukawa couplings and parameter space of G2HDM, thereby strengthening the case for precision searches in top-associated and multi-fermion final states.

These findings not only highlight the discovery potential of extended Higgs sectors but also motivate further studies at higher energies and luminosities at future colliders to conclusively test the presence of flavor-changing Higgs interactions and their connection to the origin of flavor and baryon asymmetry in the Universe.

References

[1] S. Navas et al. Review of particle physics. *Phys. Rev. D*, 110(3):030001, 2024.

[2] A. Pais and S. B. Treiman. How Many Charm Quantum Numbers Are There? *Phys. Rev. Lett.*, 35:1556, 1975.

[3] Paul A. M. Dirac. On the Theory of quantum mechanics. *Proc. Roy. Soc. Lond. A*, 112:661–677, 1926.

[4] J. J. Thomson. Cathode rays. *Phil. Mag. Ser. 5*, 44:293–316, 1897.

[5] Carl D. Anderson and Seth H. Neddermeyer. Cloud Chamber Observations of Cosmic Rays at 4300 Meters Elevation and Near Sea-Level. *Phys. Rev.*, 50:263–271, 1936.

[6] Yung-Su Tsai. Decay Correlations of Heavy Leptons in e+ e- —> Lepton+ Lepton-. *Phys. Rev. D*, 4:2821, 1971. [Erratum: Phys.Rev.D 13, 771 (1976)].

[7] Martin L. Perl et al. Evidence for Anomalous Lepton Production in e+ - e- Annihilation. *Phys. Rev. Lett.*, 35:1489–1492, 1975.

[8] J. Burmester et al. Anomalous Muon Production in e+ e- Annihilation as Evidence for Heavy Leptons. *Phys. Lett. B*, 68:297, 1977.

[9] Frederick Reines and Clyde L. Cowan. The neutrino. *Nature*, 178:446–449, 1956.

[10] C. L. Cowan, F. Reines, F. B. Harrison, H. W. Kruse, and A. D. McGuire. Detection of the free neutrino: A Confirmation. *Science*, 124:103–104, 1956.

[11] G. Danby, J. M. Gaillard, Konstantin A. Goulianos, L. M. Lederman, Nari B. Mistry, M. Schwartz, and J. Steinberger. Observation of High-Energy Neutrino Reactions and the Existence of Two Kinds of Neutrinos. *Phys. Rev. Lett.*, 9:36–44, 1962.

[12] Paul A. M. Dirac. The quantum theory of the electron. *Proc. Roy. Soc. Lond. A*, 117:610–624, 1928.

[13] C. D. Anderson. The Positive Electron. *Phys. Rev.*, 43:491–494, 1933.

[14] Murray Gell-Mann. A Schematic Model of Baryons and Mesons. *Phys. Lett.*, 8:214–215, 1964.

[15] G. Zweig. An SU(3) model for strong interaction symmetry and its breaking. Version 1. 1 1964.

[16] Elliott D. Bloom et al. High-Energy Inelastic e p Scattering at 6-Degrees and 10-Degrees. *Phys. Rev. Lett.*, 23:930–934, 1969.

[17] Martin Breidenbach, Jerome I. Friedman, Henry W. Kendall, Elliott D. Bloom, D. H. Coward, H. C. DeStaebler, J. Drees, Luke W. Mo, and Richard E. Taylor. Observed behavior of highly inelastic electron-proton scattering. *Phys. Rev. Lett.*, 23:935–939, 1969.

[18] J. J. Aubert et al. Experimental Observation of a Heavy Particle J. *Phys. Rev. Lett.*, 33:1404–1406, 1974.

[19] J. E. Augustin et al. Discovery of a Narrow Resonance in e^+e^- Annihilation. *Phys. Rev. Lett.*, 33:1406–1408, 1974.

[20] T. G. Trippe et al. New Particle Searches and Discoveries. A Supplement to the 1976 Edition Review of Particle Properties. *Phys. Lett. B*, 68:1–30, 1977.

[21] S. Abachi et al. Observation of the top quark. *Phys. Rev. Lett.*, 74:2632–2637, 1995.

[22] K. B. Davis, M. O. Mewes, M. R. Andrews, N. J. van Druten, D. S. Durfee, D. M. Kurn, and W. Ketterle. Bose-Einstein condensation in a gas of sodium atoms. *Phys. Rev. Lett.*, 75:3969–3973, 1995.

[23] Max Planck. Über das Gesetz der Energieverteilung im Normalspectrum. *Annalen Phys.*, 309(3):553–563, 1901.

[24] Albert Einstein. Concerning an heuristic point of view toward the emission and transformation of light. *Annalen Phys.*, 17:132–148, 1905.

[25] Vernon D. Barger and R. J. N. Phillips. *COLLIDER PHYSICS*. CRC Press, 1987.

[26] G. Arnison et al. Experimental Observation of Isolated Large Transverse Energy Electrons with Associated Missing Energy at $\sqrt{s} = 540$ GeV. *Phys. Lett. B*, 122:103–116, 1983.

[27] G. Arnison et al. Experimental Observation of Lepton Pairs of Invariant Mass Around 95-GeV/c**2 at the CERN SPS Collider. *Phys. Lett. B*, 126:398–410, 1983.

[28] Georges Aad et al. Observation of a new particle in the search for the Standard Model Higgs boson with the ATLAS detector at the LHC. *Phys. Lett. B*, 716:1–29, 2012.

[29] Serguei Chatrchyan et al. Observation of a New Boson at a Mass of 125 GeV with the CMS Experiment at the LHC. *Phys. Lett. B*, 716:30–61, 2012.

[30] S. L. Glashow. Partial Symmetries of Weak Interactions. *Nucl. Phys.*, 22:579–588, 1961.

[31] Steven Weinberg. A Model of Leptons. *Phys. Rev. Lett.*, 19:1264–1266, 1967.

[32] Abdus Salam. Weak and Electromagnetic Interactions. *Conf. Proc. C*, 680519:367–377, 1968.

[33] H. David Politzer. Reliable Perturbative Results for Strong Interactions? *Phys. Rev. Lett.*, 30:1346–1349, 1973.

[34] David J. Gross and Frank Wilczek. Ultraviolet Behavior of Nonabelian Gauge Theories. *Phys. Rev. Lett.*, 30:1343–1346, 1973.

[35] F. Halzen and Alan D. Martin. *QUARKS AND LEPTONS: AN INTRODUCTORY COURSE IN MODERN PARTICLE PHYSICS*. Wiley, 1984.

[36] S. L. Glashow. Partial Symmetries of Weak Interactions. *Nucl. Phys.*, 22:579–588, 1961.

[37] Abdus Salam. Weak and Electromagnetic Interactions. *Conf. Proc. C*, 680519:367–377, 1968.

[38] S. L. Glashow, J. Iliopoulos, and L. Maiani. Weak Interactions with Lepton-Hadron Symmetry. *Phys. Rev. D*, 2:1285–1292, 1970.

[39] M. Gell-Mann. The interpretation of the new particles as displaced charge multiplets. *Nuovo Cim.*, 4(S2):848–866, 1956.

[40] Kazuhiko Nishijima. Charge Independence Theory of V Particles. *Prog. Theor. Phys.*, 13(3):285–304, 1955.

[41] Peter W. Higgs. Broken symmetries, massless particles and gauge fields. *Phys. Lett.*, 12:132–133, 1964.

[42] Michael E. Peskin and Daniel V. Schroeder. *An Introduction to quantum field theory*. Addison-Wesley, Reading, USA, 1995.

[43] N. Aghanim et al. Planck 2018 results. VI. Cosmological parameters. *Astron. Astrophys.*, 641:A6, 2020. [Erratum: Astron.Astrophys. 652, C4 (2021)].

[44] A. D. Sakharov. Violation of CP Invariance, C asymmetry, and baryon asymmetry of the universe. *Pisma Zh. Eksp. Teor. Fiz.*, 5:32–35, 1967.

[45] M. B. Gavela, P. Hernandez, J. Orloff, and O. Pene. Standard model CP violation and baryon asymmetry. *Mod. Phys. Lett. A*, 9:795–810, 1994.

[46] R. Aaij et al. Test of lepton universality in $b \to s\ell^+\ell^-$ decays. *Phys. Rev. Lett.*, 131(5):051803, 2023.

[47] G. Caria et al. Measurement of $\mathcal{R}(D)$ and $\mathcal{R}(D^*)$ with a semileptonic tagging method. *Phys. Rev. Lett.*, 124(16):161803, 2020.

[48] Wolfgang Altmannshofer, Peter Stangl, and David M. Straub. Interpreting Hints for Lepton Flavor Universality Violation. *Phys. Rev. D*, 96(5):055008, 2017.

[49] John F. Gunion and Howard E. Haber. The CP conserving two Higgs doublet model: The Approach to the decoupling limit. *Phys. Rev. D*, 67:075019, 2003.

[50] Farvah Mahmoudi and Oscar Stal. Flavor constraints on the two-Higgs-doublet model with general Yukawa couplings. *Phys. Rev. D*, 81:035016, 2010.

[51] Vernon D. Barger, J. L. Hewett, and R. J. N. Phillips. New Constraints on the Charged Higgs Sector in Two Higgs Doublet Models. *Phys. Rev. D*, 41:3421–3441, 1990.

[52] David Eriksson, Johan Rathsman, and Oscar Stal. 2HDMC: Two-Higgs-Doublet Model Calculator Physics and Manual. *Comput. Phys. Commun.*, 181:189–205, 2010.

[53] Nathaniel Craig, Jamison Galloway, and Scott Thomas. Searching for Signs of the Second Higgs Doublet. 5 2013.

[54] Marcela Carena, Ian Low, Nausheen R. Shah, and Carlos E. M. Wagner. Impersonating the Standard Model Higgs Boson: Alignment without Decoupling. *JHEP*, 04:015, 2014.

[55] Wei-Shu Hou, Rishabh Jain, Chung Kao, Masaya Kohda, Brent McCoy, and Amarjit Soni. Flavor Changing Heavy Higgs Interactions with Leptons at Hadron Colliders. *Phys. Lett. B*, 795:371–378, 2019.

[56] Stefan Weinzierl. Introduction to Monte Carlo methods. 6 2000.

[57] G. Peter Lepage. A New Algorithm for Adaptive Multidimensional Integration. *J. Comput. Phys.*, 27:192, 1978.

[58] Johan Alwall, Michel Herquet, Fabio Maltoni, Olivier Mattelaer, and Tim Stelzer. MadGraph 5 : Going Beyond. *JHEP*, 06:128, 2011.

[59] Kaoru Hagiwara, Junichi Kanzaki, Qiang Li, and Kentarou Mawatari. HELAS and MadGraph/MadEvent with spin-2 particles. *Eur. Phys. J. C*, 56:435–447, 2008.

[60] Torbjorn Sjostrand, Stephen Mrenna, and Peter Z. Skands. A Brief Introduction to PYTHIA 8.1. *Comput. Phys. Commun.*, 178:852–867, 2008.

[61] Michelangelo L. Mangano, Mauro Moretti, Fulvio Piccinini, and Michele Treccani. Matching matrix elements and shower evolution for top-quark production in hadronic collisions. *JHEP*, 01:013, 2007.

[62] Leif Lonnblad. Correcting the color dipole cascade model with fixed order matrix elements. *JHEP*, 05:046, 2002.

[63] J. de Favereau, C. Delaere, P. Demin, A. Giammanco, V. Lemaître, A. Mertens, and M. Selvaggi. DELPHES 3, A modular framework for fast simulation of a generic collider experiment. *JHEP*, 02:057, 2014.

[64] Matteo Cacciari, Gavin P. Salam, and Gregory Soyez. FastJet User Manual. *Eur. Phys. J. C*, 72:1896, 2012.

[65] Matteo Cacciari, Gavin P. Salam, and Gregory Soyez. The anti-k_t jet clustering algorithm. *JHEP*, 04:063, 2008.

[66] W. Herr and B. Muratori. Concept of luminosity. In *CERN Accelerator School and DESY Zeuthen: Accelerator Physics*, pages 361–377, 9 2003.

[67] Glen Cowan, Kyle Cranmer, Eilam Gross, and Ofer Vitells. Asymptotic formulae for likelihood-based tests of new physics. *Eur. Phys. J. C*, 71:1554, 2011. [Erratum: Eur.Phys.J.C 73, 2501 (2013)].

[68] Byron P. Roe, Hai-Jun Yang, Ji Zhu, Yong Liu, Ion Stancu, and Gordon McGregor. Boosted decision trees, an alternative to artificial neural networks. *Nucl. Instrum. Meth. A*, 543(2-3):577–584, 2005.

[69] Tianqi Chen and Carlos Guestrin. XGBoost: A Scalable Tree Boosting System. 3 2016.

[70] F. Pedregosa, G. Varoquaux, A. Gramfort, V. Michel, B. Thirion, O. Grisel, M. Blondel, P. Prettenhofer, R. Weiss, V. Dubourg, J. Vanderplas, A. Passos, D. Cournapeau, M. Brucher, M. Perrot, and E. Duchesnay. Scikit-learn: Machine learning in Python. *Journal of Machine Learning Research*, 12:2825–2830, 2011.

[71] Georges Aad et al. Search for flavour-changing neutral-current couplings between the top quark and the Higgs boson in multi-lepton final states in 13 TeV pp collisions with the ATLAS detector. *Eur. Phys. J. C*, 84(7):757, 2024.

[72] Aram Hayrapetyan et al. Search for flavor-changing neutral current interactions of the top quark mediated by a Higgs boson in proton-proton collisions at 13 TeV. 7 2024.

[73] Georges Aad et al. Search for top quark decays $t \to qH$ with $H \to \gamma\gamma$ using the ATLAS detector. *JHEP*, 06:008, 2014.

[74] Masaya Kohda, Tanmoy Modak, and Wei-Shu Hou. Searching for new scalar bosons via triple-top signature in $cg \to tS^0 \to tt\bar{t}$. *Phys. Lett. B*, 776:379–384, 2018.

[75] Wei-Shu Hou and Tanmoy Modak. Probing Top Changing Neutral Higgs Couplings at Colliders. *Mod. Phys. Lett. A*, 36(07):2130006, 2021.

[76] Georges Aad et al. Search for heavy Higgs bosons with flavour-violating couplings in multi-lepton plus b-jets final states in pp collisions at 13 TeV with the ATLAS detector. *JHEP*, 12:081, 2023.

[77] Aram Hayrapetyan et al. Search for new Higgs bosons via same-sign top quark pair production in association with a jet in proton-proton collisions at $\sqrt{s} = 13$ TeV. *Phys. Lett. B*, 850:138478, 2024.

[78] Baris Altunkaynak, Wei-Shu Hou, Chung Kao, Masaya Kohda, and Brent McCoy. Flavor changing heavy higgs interactions at the lhc. *Physics Letters B*, 751:135–142, 2015.

[79] Andreas Crivellin, Ahmet Kokulu, and Christoph Greub. Flavor-phenomenology of two-Higgs-doublet models with generic Yukawa structure. *Phys. Rev. D*, 87(9):094031, 2013.

[80] Sayipjamal Dulat, Tie-Jiun Hou, Jun Gao, Marco Guzzi, Joey Huston, Pavel Nadolsky, Jon Pumplin, Carl Schmidt, Daniel Stump, and C. P. Yuan. New parton distribution functions from a global analysis of quantum chromodynamics. *Phys. Rev. D*, 93(3):033006, 2016.

[81] J. Alwall, R. Frederix, S. Frixione, V. Hirschi, F. Maltoni, O. Mattelaer, H. S. Shao, T. Stelzer, P. Torrielli, and M. Zaro. The automated computation of tree-level and next-to-leading order differential cross sections, and their matching to parton shower simulations. *JHEP*, 07:079, 2014.

[82] Armen Tumasyan et al. A new calibration method for charm jet identification validated with proton-proton collision events at $\sqrt{s}$ =13 TeV. *JINST*, 17(03):P03014, 2022.

[83] Georges Aad et al. Measurements of Higgs bosons decaying to bottom quarks from vector boson fusion production with the ATLAS experiment at $\sqrt{s} = 13\,\text{TeV}$. *Eur. Phys. J. C*, 81(6):537, 2021.

[84] Kaoru Hagiwara, Alan D. Martin, and D. Zeppenfeld. Tau Polarization Measurements at LEP and SLC. *Phys. Lett. B*, 235:198–202, 1990.

[85] Kaoru Hagiwara, Tong Li, Kentarou Mawatari, and Junya Nakamura. TauDecay: a library to simulate polarized tau decays via FeynRules and MadGraph5. *Eur. Phys. J. C*, 73:2489, 2013.

[86] Michal Czakon and Alexander Mitov. Top++: A Program for the Calculation of the Top-Pair Cross-Section at Hadron Colliders. *Comput. Phys. Commun.*, 185:2930, 2014.

[87] Celine Degrande. Automatic evaluation of UV and R2 terms for beyond the Standard Model Lagrangians: a proof-of-principle. *Comput. Phys. Commun.*, 197:239–262, 2015.

[88] Stanislaw Jadach, Johann H. Kuhn, and Zbigniew Was. TAUOLA: A Library of Monte Carlo programs to simulate decays of polarized tau leptons. *Comput. Phys. Commun.*, 64:275–299, 1990.

[89] S. Jadach, Z. Was, R. Decker, and Johann H. Kuhn. The tau decay library TAUOLA: Version 2.4. *Comput. Phys. Commun.*, 76:361–380, 1993.

[90] Georges Aad et al. ATLAS b-jet identification performance and efficiency measurement with $t\bar{t}$ events in pp collisions at $\sqrt{s} = 13$ TeV. *Eur. Phys. J. C*, 79(11):970, 2019.

[91] Identification of hadronic tau lepton decays using neural networks in the ATLAS experiment. 2019.

[92] Armen Tumasyan et al. Identification of hadronic tau lepton decays using a deep neural network. *JINST*, 17:P07023, 2022.

[93] Morad Aaboud et al. Cross-section measurements of the Higgs boson decaying into a pair of τ-leptons in proton-proton collisions at $\sqrt{s} = 13$ TeV with the ATLAS detector. *Phys. Rev. D*, 99:072001, 2019.

[94] Georges Aad et al. Measurement of the top-quark mass in $t\bar{t} + 1$-jet events collected with the ATLAS detector in pp collisions at $\sqrt{s} = 8$ TeV. *JHEP*, 11:150, 2019.

[95] Chung Kao, Hai-Yang Cheng, Wei-Shu Hou, and Joshua Sayre. Top Decays with Flavor Changing Neutral Higgs Interactions at the LHC. *Phys. Lett. B*, 716:225–230, 2012.

Appendix A

This appendix provides the detailed E_c^* selection ranges for the all-top (AT) channel and p_T^c distribution for same-sign top (SST) channel at different Higgs boson masses m_ϕ. By examining the E_c^* distributions for each m_ϕ hypothesis, the optimized cut intervals are determined and summarized in Table **1**.

m_ϕ **(GeV)**	**Optimized** E_c^* **Range (GeV)**
200	[0, 60]
250	[20, 90]
300	[60, 130]
350	[90, 150]
400	[110, 180]
450	[130, 450]
500	[150, 500]

Table 1: Optimized E_c^* selection ranges for the all-top channel corresponding to different Higgs boson masses m_ϕ.

Figure **1** presents the p_T^c distributions for dominant background ttW with signal for different m_H.

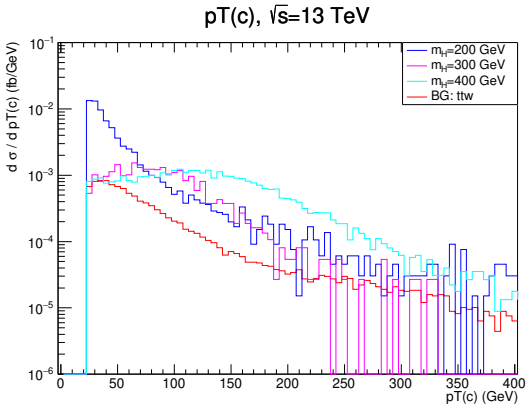


Figure 1: p_T^c distribution for $m_H = 200$ (blue), 300 (magenta) and 400 (cyan) with dominant background ttW (red) at $\sqrt{s} = 13$ TeV.